

© COPYRIGHTED BY

Saurabh Jain

August 2009

ISOTROPIC MULTIREOLUTION ANALYSIS
AND
ROTATIONAL INVARIANCE IN IMAGE ANALYSIS

A Dissertation

Presented to

the Faculty of the Department of Mathematics

University of Houston

In Partial Fulfillment

of the Requirements for the Degree

Doctor of Philosophy

By

Saurabh Jain

August 2009

ISOTROPIC MULTIREOLUTION ANALYSIS
AND
ROTATIONAL INVARIANCE IN IMAGE ANALYSIS

Saurabh Jain

APPROVED:

Dr. Emmanouil Papadakis,
Chairman

Dr. Robert Azencott

Dr. Donald Kouri

Dr. Bernhard Bodmann

Dean, College of Natural Sciences and Mathematics

Acknowledgements

Attaining this doctoral degree would not have been possible without the contribution of numerous people who instilled their faith in my abilities, and nurtured me over the period of last five years and the time before that. First and foremost, I would like to thank my adviser, Prof. Manos Papadakis, for his constant support and encouragement to help me pursue my research. His valuable insights and expertise in the area were indispensable tools for the completion of this project.

Next, I would like to thank Profs. Robert Azencott, Bernhard Bodmann, and Don Kouri for serving on my defense committee, and for their insightful contributions to various projects that I worked on during the period of the last five years at UH. Thanks to Juan, Simon, Shikha, and other members of the Papadakis group for many stimulating discussions about, and contributions to, this research. I would also like to thank all the members of Mathematical Sciences Foundation, especially Drs. Dinesh Singh, Sanjeev Agrawal, and Amber Habib, for motivating me and preparing me for a research career in mathematics. Thanks to Drs. Eric Dussaud, Paul Williamson, Henri Calandra, and other members of the HGRG at Total E&P for providing an excellent research environment for our joint work on the seismic imaging project. Thanks to Total E&P for their financial support on the said project.

Finally, I would like to thank all my friends and family, here in the United States and back home in India, for being my strength when research made me feel burnt out. A special thanks to my uncle, Mr. Vivek Jain, for motivating me to choose a research career. I dedicate this thesis to my parents and my brother, who have always supported me in my pursuits, even though most of the time they were quite clueless about my work.

ISOTROPIC MULTIREOLUTION ANALYSIS
AND
ROTATIONAL INVARIANCE IN IMAGE ANALYSIS

An Abstract of a Dissertation
Presented to
the Faculty of the Department of Mathematics
University of Houston

In Partial Fulfillment
of the Requirements for the Degree
Doctor of Philosophy

By
Saurabh Jain
August 2009

Abstract

In this thesis, we study the theory of Isotropic Multiresolution Analysis (IMRA) and its application to image analysis problems that require rotational invariance. Multiresolution Analysis (MRA) is a mathematical tool that gives us the ability to process a signal or an image at multiple levels of resolution and detail. IMRA is a new type of MRA for which the core resolution sub-space is invariant under all rotations. We give a characterization of IMRAs using the Lax-Wiener theorem, which shows that all the resolution and detail spaces of an IMRA are invariant under all rigid motions. We further develop examples of isotropic wavelet frames associated to IMRA via the Extension Principles. This facilitates the fast implementation of isotropic wavelet decomposition and reconstruction algorithms.

We derive an IMRA-based explicit scheme for the numerical solution of the acoustic wave equation in the context of seismic migration. The multiscale structure of the IMRA offers the possibility of improving the computational efficiency of the standard explicit schemes used in seismic imaging.

We develop a novel rotationally invariant three-dimensional texture classification scheme using Gaussian Markov Random Fields on \mathbb{Z}^3 to model textures sampled on a discrete lattice. These are considered to be sampled versions of continuous textures, which are viewed as realizations of stationary Gaussian random fields on \mathbb{R}^3 . IMRA is used to bridge the gap between the discrete and the continuous domains, where the rotation invariance of the resolution spaces plays a key role.

Contents

1	Introduction and Preliminaries	1
1.1	Background	1
1.2	Notation	8
1.3	Classical Fast Wavelet Algorithms	12
1.3.1	Definition of a Classical MRA	13
1.3.2	Construction of Wavelets from MRAs	13
1.3.3	The Fast Wavelet Algorithm	15
1.4	Frames	22
2	Isotropic Multi-Resolution Analysis	24
2.1	Isotropic Multiresolution Analysis of $L^2(\mathbb{R}^d)$	24
2.2	Characterization of IMRAs	25
2.3	Isotropic Refinable Functions and IMRAs	30
3	Isotropic Wavelets from Extension Principles	33
3.1	Extension Principles Revisited	35
3.2	Examples of Isotropic Wavelet Frames	58
3.3	Fast Isotropic Wavelet Transform	68

4	Explicit Schemes in Seismic Migration and Isotropic Multiscale Representations	74
4.1	Explicit Schemes for Wave Equation Migration	75
4.2	IMRA-based Solution of the One-way Acoustic Wave Equation	78
4.2.1	Discretization of the Propagator	80
4.2.2	Decomposing the Signal and the Propagator Matrix using the Fast Isotropic Wavelet Algorithm	83
4.2.3	Increasing the Sparsity of the Propagator Matrix	89
4.3	Filter Design and Implementation	91
4.3.1	McClellan Transform	93
4.3.2	Soubaras' Laplacian Synthesis	94
4.3.3	Computational Cost	98
5	Rotationally Invariant 3-D Texture Classification	111
5.1	Introduction	111
5.2	Description of the GMRF Model	115
5.2.1	Gibbs and Markov Random Fields	116
5.2.2	Gaussian Markov Random Field	118
5.2.3	Parameter Estimation	120
5.2.4	Synthesizing a GMRF	123
5.3	Rotationally Invariant Distance	123
5.3.1	KL-distance Between two Gaussian Markov Random Fields	125
5.3.2	Rotation of Textures	126
5.3.3	Practical Implementation of the Distance	128
5.4	Experimental Results	130
5.5	Conclusion and Future Work	137
	Bibliography	138
	Index	146

List of Figures

1.1	High pass band outputs of the ‘Barbara’ image; one scale decomposition only. Image (a) obtained with the Isotropic high pass filter associated to an IMRA. Image (b) was obtained with the tensor product one dimensional Daubechies-8 filters and is the mix (normalized sum) of all bands but the low-low. Notice in (b) the distortion in Barbara’s scarf texture due the directional filtering selectivity of the tensor product filters. This effect is almost absent in (a).	2
1.2	Schematic representation of the decomposition algorithm	17
1.3	Schematic representation of the reconstruction algorithm	18
1.4	Flow diagram for one level of decomposition	21
1.5	Flow diagram for one level of reconstruction	22
3.1	Fourier transforms of a typical isotropic refinable function (left) and wavelet (right).	60
3.2	Isotropic refinable function (left) and wavelet (right) in the space domain. .	61
3.3	Radial profiles of the transfer functions of various filters used in Example 3.2.2. Notice that all filters lie between 0 and 1. The actual high pass filters are a constant multiple of the filters shown here (see Equation (3.29)). Since the constant differs with the dimension of the space and the dilation factor, we have not shown it here. The dashed graphs represent the synthesis filters while the solid ones represent the analysis filters.	62
3.4	Flow diagram for one level of decomposition in FIWT	69
3.5	Flow diagram for one level of reconstruction in FIWT	69

4.1	Here we show the vertical cross sections of the images obtained for the SEG Salt model using IMRA. The left image on the top was obtained by discretizing the propagator at the zero resolution level. The right image on the top was obtained using one-level of decomposition with the Dyadic dilation matrix. The image on the bottom was obtained using one-level of decomposition using the Quincunx dilation matrix (4.16).	87
4.2	Horizontal cross-sections of the results obtained using the IMRA for the Impulse (left) and the Salt (right) models. Due to the radial nature of the filters the faults in all directions are imaged with the same accuracy and have no directional artifacts.	88
4.3	Trigonometric polynomial approximations of the propagator filter with a weighted least squares algorithm (top) and with a truncated Fourier series (bottom). Both have 25×25 coefficients.	92
4.4	The 1-D profiles of the filters, L (dashed) and L_0 (solid), along the k_x -axis. Here L is a trigonometric polynomial in Equation (4.17) with $N_x = N_y = 5$. The approximation is exact up to k_{exact}	95
4.5	The figure on the left has the contours of the ‘Improved McClellan filter’ plotted along with the exact function $\cos\left(\sqrt{k_x^2 + k_y^2}\right)$. The figure on the right is a contour plot of a synthesized Laplacian, L with $N_x = N_y = 5$ along with the contour plot of the exact function $k_x^2 + k_y^2$. Notice that although the McClellan filter gives a very good approximation of the exact function along the axes, it deviates significantly along the $k_x = k_y$ line. The Soubaras’ filter is a good approximation in all directions up to a radius k_{exact} (See Figure 4.4) which is larger than the radius up to which the McClellan filter gives a good approximation. Beyond k_{exact} , the Soubaras’ filter also deviates from the exact function $k_x^2 + k_y^2$ as the contours for the filter are not radial for radii bigger than k_{exact}	97
4.6	Slice $y = 76$ of the constant velocity impulse model using McClellan (top) and Soubaras (bottom).	99
4.7	Slice $x = y$ of the constant velocity impulse model using McClellan (top) and Soubaras (bottom). The result from McClellan shows a lot of dispersion in the higher angles while the Soubaras gives an accurate result.	100
4.8	Slice $y = 76$ (top) and $x = y$ (bottom) of the constant velocity impulse model using 2D IMRA filters. These results have less ringing than the ones obtained from Soubaras. (Figures 4.6,4.7)	101
4.9	Slice $z = 75$ using McClellan. Notice the dispersion in the 45° azimuth angle which is absent in the results obtained from Soubaras (Figure 4.10) and full 2-D IMRA implementation (Figure 4.11).	102

LIST OF FIGURES

4.10 Slice $z = 75$ of the constant velocity impulse model using Soubaras. The result is accurate in all directions but has more ringing than the result obtained from a full 2-D convolution (Figure 4.11) 103

4.11 Slice $z = 75$ of the constant velocity impulse model using 2D IMRA filters at the zero resolution level (without decomposing into low and high pass components). 104

4.12 Slice $y = 5$ of the steep model using McClellan. 105

4.13 Slice $y = 5$ of the steep model using Soubaras. 106

4.14 Slice $y = 5$ of the steep model using 2D IMRA filters at the zero resolution level (without decomposing into low and high pass components). 107

4.15 Slice $x = y$ of the steep model using McClellan. Notice the dispersion in the higher angles of propagation. The results obtained from Soubaras (Figure 4.16) and 2-D IMRA filters (Figure 4.17) do not have these artifacts. 108

4.16 Slice $x = y$ of the steep model using Soubaras. 109

4.17 Slice $x = y$ of the steep model using 2D IMRA filters at the zero resolution level (without decomposing into low and high pass components). 110

5.1 Examples of structural 2-D textures 112

5.2 Examples of stochastic 2-D textures 112

List of Tables

4.1	Percentage of points in the high pass component that must be propagated for various ranges of temporal frequencies, in the case of Dyadic and Quincunx dilations, for the SEG Salt model.	90
5.1	Parameters for synthetic textures used for experimental study.	131
5.2	Distances between two rotations of two distinct textures using the rotationally invariant distance defined in Equation (5.23) and autocovariance resampled on $\frac{\mathbb{Z}^3}{4}$. Below each distance we list the angles $(\alpha^*/\pi, \beta^*/\pi, \gamma^*/\pi)$, where $(\alpha^*, \beta^*, \gamma^*)$ is the minimizer.	133
5.3	Distances between two rotations of two distinct textures using the rotationally invariant distance defined in Equation (5.23) and autocovariance resampled on $\frac{\mathbb{Z}^3}{2}$. Below each distance we list the angles $(\alpha^*/\pi, \beta^*/\pi, \gamma^*/\pi)$, where $(\alpha^*, \beta^*, \gamma^*)$ is the minimizer.	134
5.4	Distances between two rotations of two distinct textures using the rotationally invariant distance defined in Equation (5.23) and autocovariance sampled on the original grid \mathbb{Z}^3 . Below each distance we list the angles $(\alpha^*/\pi, \beta^*/\pi, \gamma^*/\pi)$, where $(\alpha^*, \beta^*, \gamma^*)$ is the minimizer.	135
5.5	Distances between five distinct textures using the rotationally invariant distance defined in Equation (5.23) and autocovariance resampled on the grid $\frac{\mathbb{Z}^3}{2}$	136

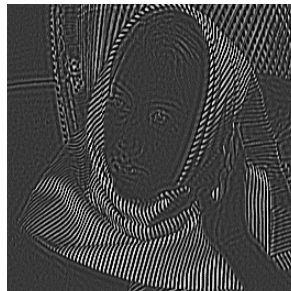
Chapter 1

Introduction and Preliminaries

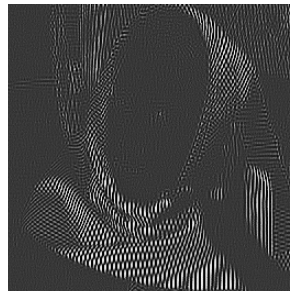
1.1 Background

The ability to process a signal at multiple levels of resolution is highly desirable in signal and image processing. Being able to switch between coarser and finer resolutions allows us to adaptively process only the relevant details for the problem at hand. A multiresolution analysis (abbreviated as MRA), provides a formal mathematical setting for a mechanism to switch between resolutions. The idea of a multiresolution pyramid, used by Burt and Adelson [18] in the context of computer vision, is a precursor to the formal definition of a Multiresolution Analysis (also called Multiresolution Approximation) of $L^2(\mathbb{R})$ given by Mallat [78] and Meyer [85] (see Definition 1.3.1 below). Around the same time a simple yet not accurately implementable idea was proposed, the continuous wavelet transform, based on the ideas from reflection seismology and coherent quantum states by Morlet and Grossman [53]. However, wavelets associated with a Multiresolution Analysis are particularly useful in practice because of the associated fast wavelet algorithms which provide

numerically stable and accurate decompositions and reconstructions (see Section 1.3.3). To date, the most popular examples of higher dimensional MRAs have been obtained from MRA of $L^2(\mathbb{R})$ via a tensor product construction. Their popularity stems from the relatively easy implementation of the resulting wavelet transforms which essentially involves the application of the 1- D transforms along the rows and columns of an image (see [79] p. 346). However, this image processing in a row and column fashion is also one of the major drawbacks of this approach since it gives rise to what is known as directional bias. The need to eliminate directional bias in digital filtering using scaling functions and wavelets with high degree of smoothness and symmetry motivated us to introduce Isotropic Multiresolution Analysis, abbreviated as IMRA. Figure 1.1(b) demonstrates the advantage of isotropic filters over tensor product constructions using a standard two dimensional image known as ‘Barbara’ in the image processing literature. We see that while the vertical and



(a) IMRA



(b) 2- D DWT (tensor product)

Figure 1.1: High pass band outputs of the ‘Barbara’ image; one scale decomposition only. Image (a) obtained with the Isotropic high pass filter associated to an IMRA. Image (b) was obtained with the tensor product one dimensional Daubechies-8 filters and is the mix (normalized sum) of all bands but the low-low. Notice in (b) the distortion in Barbara’s scarf texture due the directional filtering selectivity of the tensor product filters. This effect is almost absent in (a).

horizontal patterns are picked up by the 2- D DWT, the patterns at other orientations are distorted. The likely reason for this outcome is that tensor product MRAs give rise to

filters with higher sensitivity in horizontal and vertical orientations. This selectivity in filtering is what we refer to as directional bias. This motivates us to construct IMRA with radial filters, since such filters are not biased towards any preferred direction. Even though we are not the first to have realized the need to reduce this sort of filtering bias, there is no formal definition of the term directional bias in the literature. In fact, this need to eliminate the “preferred directions” effect [10] has motivated the constructions of filters and multiresolution analyses that are not tensor products of one-dimensional ones, the so-called non-separable MRAs e.g. [3–6, 10, 19, 33, 39, 52, 59, 68, 73]. One of the major design constraints in all these constructions is that the scaling function is required to form a basis. Consequently, the scaling functions of these non-separable MRA designs suffer from lack of either symmetry or smoothness or both. For instance, as pointed out in the introduction of [10], the scaling functions in [52], are indicator functions of (often fractal-like) compact sets while those in [68] have discontinuous first derivatives. In addition, most of these constructs are in two-dimensions. To remedy this situation we allow redundancy in our design which gives the flexibility of using highly symmetric and smooth scaling functions.

The need for filters with radial symmetry has been recognized in the past, not in an MRA-context but for multiscale transforms. The most well known and probably the oldest approach in this context is the Canny Edge Detector [23] motivated by the studies of Marr and Hildreth [82] on vision. The authors of [82] use the Laplacian of a radial Gaussian for edge detection to achieve an orientation-independent design; a goal similar to ours. For the same reason, radial Gaussian filters with various widths (corresponding to different scales) are used in [23]. More recently, the use of isotropic filters has been proposed by Fickus and co-workers who develop moment transforms covariant with respect to rigid motions in multidimensions [47, 48]. The need to derive MRA wavelet decompositions covariant with respect to rigid motions also motivated [36, 49]. These constructs are in $2-D$ and are not

generalizable to higher dimensions and the Fourier transforms of their radial Riesz scaling functions are discontinuous at the origin. Other notable constructions of multidimensional, isotropic or radial frame wavelets have been proposed in [2, 57, 86]. However, these have not been shown to arise from MRAs or yield decompositions implementable with MRA-type fast wavelet algorithms. In [42, 43], Epperson and Frazier construct radial wavelets suited for polar co-ordinates but these are not translation invariant and have limited practical utility.

An alternative method to reduce the effects of directional bias is to introduce *more* preferred directions to the filtering by augmenting one dimensional constructions with multiscale or monoscale angular decomposition. In other words one might spread the directional bias into more than the obvious directions. We refer to all of those as *directional representations*. There are two dominant schools in directional representations; one pioneered by Candes, Donoho, and collaborators who introduced ridgelets, wedgelets, beamlets, planelets, shearlets, curvelets, etc. (see e.g., [20–22, 40, 54, 71]) and the other pioneered by Kingsbury proposing monoscale angular resolution (see e.g., [67, 98, 99]). The latter approach aims at using oversampled filters, applied to rows and columns of an image, in order to mitigate the problem of directional bias. In [67] the phase information of a complex wavelet transform is used to encode the local orientation information while [98, 99] use tensor products of oversampled filter banks based on B-splines. The angle selectivity in either of these approaches is limited to a finite number of orientations. Among the directional representations of Candes and Donoho, curvelets have received the most attention as these are claimed to yield an optimally sparse representation for 2- D images that are smooth away from C^2 -edges [22]. The construction relies on a product of radial and angular windows that form a partition of the unity, and a parabolic dilation matrix. Unlike the construction of Kingsbury, for curvelets the angular resolution increases with

the scale. The discrete curvelet transform and its implementation is described in [109]. The transform has a redundancy factor of 5 which can pose problems for large data-sets used in modern signal processing applications such as seismic imaging and biomedical imaging. In contrast, the redundancy factor for the fast isotropic wavelet transform described in Section 3.3 is bounded above by 2 and is close to 1.5 for a finite number of levels of decomposition. The trade-off is the lack of directional information that may be obtained from the curvelet transform and other directional representations. But for applications such as seismic imaging (see Chapter 4) where low redundancy and isotropic filters are required, IMRA scores over directional transforms. It is also better suited for isotropic textures arising in medical imaging, a rigorous treatment of which can be found in [88]. Another notable construction, with frequency tiling similar to the discrete curvelet transform, called shearlets has been described in [71]. It is shown to arise from an MRA with the so-called composite dilations [54] which results in “a faithful transition from the continuous to the discrete representation” [41]; unlike curvelets, for which the discrete representation is only an approximation to the continuous transform. Other directional representations in the spirit of digital filter design, not directly related to multiresolution analyses nor to wavelets can be found in [1, 32, 50, 61, 63, 92, 100].

In this thesis, we study the approach to isotropic filters and IMRAs that originated in [89] and continued in [14, 88]. We formally define Isotropic Multiresolution Analysis of $L^2(\mathbb{R}^d)$ in Chapter 2. This is a new type of MRA for which the core subspace, V_0 , is invariant under all rotations, in addition to its usual invariance under integer translations. The rotational invariance of the resolution spaces addresses an important concern in sampling theory: Intuitively, the resolution of an image should not change as a result of a rigid motion applied to it. But that is not the case with the resolution spaces corresponding to the multiresolution constructions available in the literature. This situation is remedied

in the construction of IMRA, since the resolution spaces are, by definition, rotationally invariant. In fact, these spaces are shown to be invariant under all rigid motions in Section 2.2. In addition, the IMRA design addresses other concerns with the non-separable and isotropic constructions discussed above. Firstly, it is easily generalizable to any number of space dimensions. In fact, we describe all constructions for $L^2(\mathbb{R}^d)$ for a general d . Next, the examples of isotropic scaling functions produced in Section 3.2 exhibit high degree of smoothness in addition to their radial symmetry. In Chapter 3, we construct isotropic wavelets associated with IMRAs using the so-called Extension Principles [38, 97] which facilitates fast algorithmic implementation of the IMRA decomposition and reconstruction algorithms.

In Section 3.1, we revisit the Extension Principles which first appear in the celebrated paper of Ron and Shen [97], and are later studied in [38], where they are used to design Framelets. A Framelet is an affine family $\Psi := \left\{ D_A^j T_{\mathbf{k}} \psi_i : j \in \mathbb{Z}, \mathbf{k} \in \mathbb{Z}^d, i = 1, \dots, m \right\}$ such that each ψ_i belongs to the resolution space V_1 of a MRA. In their definition of MRA, the authors of [38] only require the translates of the scaling function, ϕ (the generator of V_0), to be a Bessel family. The Extension Principles characterize affine families that form tight frames or a pair of dual frames in terms of quadrature mirror type conditions on the associated low and high pass filters. In applications such as seismic imaging [62], we are interested in families of the form

$$X_{\phi\psi} := \left\{ D_A^j T_{\mathbf{k}} \psi_i : j \in \mathbb{N} \cup \{0\}, \mathbf{k} \in \mathbb{Z}^d, i = 1, \dots, m \right\} \cup \left\{ T_{\mathbf{k}} \phi : \mathbf{k} \in \mathbb{Z}^d \right\}.$$

We are interested in the question of whether $X_{\phi\psi}$ forms a Parseval frame of $L^2(\mathbb{R}^d)$. This question is not answered by the Extension Principles. We characterize the families of the form $X_{\phi\psi}$ that are Parseval frames or yield a pair of dual frames of $L^2(\mathbb{R}^d)$ in terms of conditions on the associated low and high pass filters that are the same as those that appear

in the Extension Principles but with the so-called fundamental function identically equal to one.

We discuss the application of IMRA to seismic imaging in Chapter 4. Migration is a seismic imaging technique used by the oil industry to image the sub-surface of the Earth for the purpose of oil prospecting. In Section 4.1, we give a very brief overview of what is called wave equation migration and we arrive at the so-called Phase-shift propagator operator which is used to obtain the image of the interior by downward propagating acoustic waves recorded on the surface. An efficient discretization of this operator using the isotropic frames arising from IMRA constitutes an explicit migration scheme which is described in Section 4.2. The importance of circularly symmetric propagator filters, required to design accurate explicit schemes for wave equation migration, has been discussed in [44, 56, 101, 104]. We show that on top of the circular symmetry, the multiscale structure of IMRA offers the possibility of reducing the computational cost. This can be compared to the work of Margrave and his collaborators [81], who describe a sub-sampling scheme based on the temporal frequency domain. However, the IMRA-based scheme is more general because we sub-sample not only for one fixed frequency, but also for various regions of the sub-surface image where the sound velocity is high. In addition, our treatment of the discretization of the propagator is formal as compared to the various ad-hoc discretization schemes available in the geophysical literature.

We continue the theme of rotation invariance in image analysis in Chapter 5 where we describe a rotationally invariant 3- D texture classification scheme. In Section 5.1, we discuss the literature on rotationally invariant texture classification. The models present in the literature are mostly for 2- D textures and impose an isotropic structure on possibly non-isotropic textures. We define a texture signature that is itself non-isotropic but the

rotational invariance is achieved via a rotationally invariant distance between these texture signatures that we define in Section 5.3. We describe a practical implementation of this distance that stays computationally efficient in 3- D (Section 5.3.3). Textures defined on a discrete lattice are modeled using Gaussian Markov Random Fields following the approach of Chellappa [25]. We consider the texture defined on a discrete lattice to be samples of a continuous texture which is viewed as a realization of a stationary Gaussian random field on \mathbb{R}^3 . The rotation of a texture then takes a natural form and is shown to be equivalent to the rotation of the corresponding autocovariance function (Section 5.3.2). IMRA is used to bridge the gap between the discrete and the continuous domains where the rotation invariance of the resolution spaces plays a key role.

In the remainder of this chapter, we set up the notation (Section 1.2), and discuss the preliminaries. We discuss the classical MRA of Mallat and Meyer, and the associated fast wavelet algorithms in Section 1.3. We give a quick overview of frames for separable Hilbert spaces, and their characterization in terms of the so called analysis and synthesis operators, in Section 1.4.

1.2 Notation

Before we give the formal definition of an MRA, we must set up some notation that is used here and in the subsequent chapters of this thesis.

We use \mathcal{F} to denote the Fourier Transform on $L^2(\mathbb{R}^d)$ defined via

$$\mathcal{F}f(\boldsymbol{\xi}) = \hat{f}(\boldsymbol{\xi}) = \int_{\mathbb{R}^n} f(\mathbf{x})e^{-2\pi i\langle \mathbf{x}, \boldsymbol{\xi} \rangle} d\mathbf{x} \quad \boldsymbol{\xi} \in \mathbb{R}^d,$$

for all $f \in (L^1 \cap L^2)(\mathbb{R}^d)$ and extended to an isometry on all of $L^2(\mathbb{R}^d)$.

1.2. NOTATION

For convenience we adopt the notation,

$$e_{\mathbf{k}}(\boldsymbol{\xi}) = e^{-2\pi i \langle \mathbf{k}, \boldsymbol{\xi} \rangle} \quad \boldsymbol{\xi} \in \mathbb{R}^d; \mathbf{k} \in \mathbb{Z}^d,$$

for the modulations and

$$\mathbb{T}^d = [-1/2, 1/2]^d,$$

for the fundamental domain.

For $\mathbf{y} \in \mathbb{R}^d$, the (unitary) shift operator $T_{\mathbf{y}}$ is defined as

$$T_{\mathbf{y}}f(\mathbf{x}) = f(\mathbf{x} - \mathbf{y}), f \in L^2(\mathbb{R}^d).$$

Given a lattice $\Gamma \subset \mathbb{R}^d$ which is similar to \mathbb{Z}^d , a linear closed subspace V of $L^2(\mathbb{R}^d)$ is said to be Γ -**shift-invariant** if for each $\boldsymbol{\gamma} \in \Gamma$, $T_{\boldsymbol{\gamma}}V = V$. When we use the term shift-invariant for a subspace we mean $\Gamma = \mathbb{Z}^d$.

Given S , a subset of a linear space V , the notation $\langle S \rangle$ will be used for the shift invariant subspace generated by S (i.e., the smallest shift invariant subspace of V containing S). If $S = \{\phi\}$, we will write $\langle \phi \rangle$ to denote $\langle \{\phi\} \rangle$.

Moreover, \mathbb{S}^{d-1} denotes the unit sphere in d dimensions, centered at the origin. For $\mathbf{x} \in \mathbb{R}^d$ and $\rho > 0$, $B(\mathbf{x}, \rho)$ will denote the ball centered at \mathbf{x} with radius ρ . We will not distinguish open from closed balls because the difference $\overline{B(\mathbf{x}, \rho)} \setminus B(\mathbf{x}, \rho)$ (a d sphere) has measure zero in \mathbb{R}^d . By $\text{supp} f$ we mean the closure of the set of points \mathbf{x} such that $f(\mathbf{x}) \neq 0$.

Given $\Omega \subset \mathbb{R}^d$ with positive measure, PW_{Ω} is the closed subspace of $L^2(\mathbb{R}^d)$ defined as

$$PW_{\Omega} = \{f \in L^2(\mathbb{R}^d) : \text{supp} \hat{f} \subseteq \Omega\}.$$

If r is a positive real number, PW_r will denote $PW_{B(0,r)}$. The subspace PW_{Ω} is called a *Paley-Wiener* subspace of $L^2(\mathbb{R}^d)$ associated to Ω , if Ω has compact closure, or simply

a *Wiener* subspace of $L^2(\mathbb{R}^d)$ associated to Ω if Ω is an arbitrary measurable subset of \mathbb{R}^d . The Lax-Wiener Theorem states that these are the only subspaces of \mathbb{R}^d that are invariant under the action the group of translations induced by \mathbb{R}^d [74]. This theorem plays a central role in the characterization of IMRAs (Section 2.2). Finally, we remark that all set equalities and inclusions are modulo null sets unless otherwise mentioned.

Definition 1.2.1 *Let Ω be a measurable subset of \mathbb{R}^d .*

1. *We say that $\Omega \subset \mathbb{R}^d$ is **radial** if for all $R \in SO(d)$, $R\Omega = \Omega$.*
2. *A $d \times d$ matrix is **expansive** if it has integer entries and if all of its eigenvalues have absolute value greater than 1.*
3. *An expansive matrix is **radially expansive** if $A = aR$, for some fixed $a > 0$ and a matrix $R \in SO(d)$.*

A radially expansive matrix A is a matrix with integer entries that leaves the lattice \mathbb{Z}^d invariant, and $|\det A|$ is a positive integer. The term *isotropic* is sometimes used to refer to matrices that are similar to a diagonal matrix and for which every eigenvalue has the same absolute value [75]. However, these ‘isotropic’ matrices are not suitable for our study because they do not necessarily map radial sets into radial sets. We also note that we use the term ‘*isotropic*’ in an entirely different context.

If A is an expansive (or radially expansive) matrix, we define its associated unitary dilation operator by

$$\forall f \in L^2(\mathbb{R}^d), D_A f(x) = |\det A|^{1/2} f(Ax).$$

A function g defined on \mathbb{R}^d is said to be **radial** if, $g(x_1) = g(x_2)$, whenever $\|x_1\| = \|x_2\|$. A subset \mathfrak{F} of \mathbb{R}^d is **radial** if its characteristic function $\chi_{\mathfrak{F}}$ is equal a.e. to a Lebesgue measurable radial function. Now, let \mathfrak{F} be a Lebesgue measurable subset of \mathbb{R}^d . Then, $\chi_{\mathfrak{F}}$ is measurable and now a change of coordinates from Cartesian to spherical together with Tonelli's theorem readily imply

$$\int_{\mathbb{R}^d} \chi_{\mathfrak{F}} = \int_0^\infty \int_{\mathbb{S}^{d-1}} \chi_{\mathfrak{F}}(r, \theta) r^{d-1} d\theta dr .$$

The change of variable preserves the measurability of $\chi_{\mathfrak{F}}$ because the transformation from Cartesian to spherical coordinates is continuous. For a.e. $r > 0$, the function $\chi_{\mathfrak{F}}(r, \cdot)$ is a.e. constant on the sphere $r\mathbb{S}^{d-1}$, so either it takes the value 1 or the value 0 on $r\mathbb{S}^{d-1}$. But, the result of the first of the two successive integrations is a measurable function with respect to r , and the value of this function is either $m(\mathbb{S}^{d-1})$ or 0, where $m(\mathbb{S}^{d-1})$ is the area of the sphere \mathbb{S}^{d-1} . So, there exists a measurable subset F of \mathbb{R}^+ such that

$$\int_{\mathbb{R}^d} \chi_{\mathfrak{F}} = m(\mathbb{S}^{d-1}) \int_0^\infty \chi_F(r) r^{d-1} dr .$$

We will call this set F a *radial profile* of \mathfrak{F} . This set is Lebesgue measurable but it is not uniquely defined for any given radial subset of \mathbb{R}^d . Nonetheless, all radial profiles are 'equal' in the sense of measure-theoretic set-equality. Generalizing this analysis we call a measurable function f defined on \mathbb{R}^d radial, if for almost every $r > 0$, the restriction of f on $r\mathbb{S}^{d-1}$ is a.e. equal to a constant function, with respect to the surface measure of \mathbb{S}^{d-1} . Thus, from now on, all these functions are considered constant on the spheres $r\mathbb{S}^{d-1}$, for a.e. $r > 0$. This also applies to characteristic functions of radial sets. Thus, if \mathfrak{F} is a radial set, then for a.e. r in its radial profile, the sphere $r\mathbb{S}^{d-1}$ is contained in \mathfrak{F} . This readily implies that radial sets remain invariant under all rotations and radially expansive matrices map radial sets onto radial sets.

To simplify the language we henceforth drop the term measurable when we refer to functions and sets, since we assume that all of them are measurable. We will often need to consider the restriction of a function on a radial set \mathfrak{F} . Doing so, we use the term ‘radial’ to refer to the property that the restrictions of the function to the spheres $r\mathbb{S}^{d-1}$ are constant for a.e. r in a radial profile of \mathfrak{F} .

If L is a measurable subset of \mathbb{R}^d , x_0 is a *point of density* of L if,

$$\lim_{\eta \rightarrow 0} \frac{|L \cap (B(x_0, \eta))|}{|B(0, \eta)|} = 1 .$$

A well-known theorem due to Lebesgue asserts that a.e. every point of L is a point of density of L , e.g. [107], and for a.e. x_0 in L^c

$$\lim_{\eta \rightarrow 0} \frac{|L \cap (B(x_0, \eta))|}{|B(0, \eta)|} = 0 .$$

Since radial sets remain invariant under rotations we readily assert that if x_0 is a point of density for some radial set, then all the points on the sphere $\|x_0\|\mathbb{S}^{d-1}$ share the same property. A function $f \in L^2(\mathbb{R}^d)$ is said to be *isotropic* if there exist $y \in \mathbb{R}^d$ and a radial function $g \in \mathbb{R}^d$ such that $f = T_y g$. A function $f \in L^2(\mathbb{R}^d)$ is said to be **isotropic** if there exists a $\mathbf{y} \in \mathbb{R}^d$ and a radial function $g \in \mathbb{R}^d$ such that $f = T_{\mathbf{y}} g$.

1.3 Classical Fast Wavelet Algorithms

We now present a brief overview of the Multiresolution Analysis (MRA) theory of $L^2(\mathbb{R})$ and the resulting fast wavelet algorithms. In the rest of this chapter, the dilation operator is assumed to be defined with respect the dyadic dilation matrix, and is denoted by D .

1.3.1 Definition of a Classical MRA

Definition 1.3.1 A sequence of closed subspaces $\{V_j\}_{j \in \mathbb{Z}}$ of $L^2(\mathbb{R})$ is called a **Multiresolution Analysis (MRA)** of $L^2(\mathbb{R})$ if and only if

- $V_j \subset V_{j+1} \quad \forall j \in \mathbb{Z}$,
- $f \in V_j \Leftrightarrow Df \in V_{j+1}$,
- $\bigcap_{j \in \mathbb{Z}} V_j = \{0\}$,
- $\overline{\bigcup_{j \in \mathbb{Z}} V_j} = L^2(\mathbb{R})$,
- There exists a function $\phi \in V_0$ such that $\{T_k \phi : k \in \mathbb{Z}\}$ is an orthonormal basis of V_0 .

The function ϕ is called the **scaling function** of the MRA. Here, the hypothesis that the translates of the scaling function form an orthonormal basis for V_0 , can be replaced by just requiring this set to be a Riesz basis.

1.3.2 Construction of Wavelets from MRAs

Let us now review the construction of orthonormal wavelets from MRA. We begin with the definition of an orthonormal wavelet of $L^2(\mathbb{R})$.

Definition 1.3.2 A function $\psi \in L^2(\mathbb{R})$ is called an **orthonormal wavelet** if and only if the set $\{D^j T_k \psi\}_{j,k \in \mathbb{Z}}$ is an orthonormal basis of $L^2(\mathbb{R})$.

Next, since $D^*\phi \in V_{-1}$, the inclusion $V_{-1} \subset V_0$ implies that $D^*\phi$ can be written in terms of the orthonormal basis of V_0

$$2^{-1/2}\phi(x/2) = \sum_{k \in \mathbb{Z}} \alpha_k T_{-k}\phi(x).$$

This equation is known as the **two-scale relation**. Taking the Fourier Transform of the above equation, we get

$$2^{1/2}\hat{\phi}(2\xi) = \hat{\phi}(\xi) \sum_{k \in \mathbb{Z}} \alpha_k e^{2\pi i k \xi}.$$

This gives us the following equation also called the two-scale relation (in the frequency domain)

$$2^{1/2}\hat{\phi}(2\xi) = \hat{\phi}(\xi)m_0(\xi),$$

where $m_0(\xi) = \sum_{k \in \mathbb{Z}} \alpha_k e^{2\pi i k \xi}$ is a 1-periodic function called the **low pass filter** corresponding to the scaling function ϕ .

Now, let W_0 be the orthogonal complement of V_0 in V_1 , that is $V_1 = V_0 \oplus W_0$. Then, $W_j = D^j(W_0)$ is a closed subspace of V_{j+1} such that for all $j \in \mathbb{Z}$

$$V_{j+1} = V_j \oplus W_j.$$

Now, the inclusion $V_j \subset V_{j+1}$ for all $j \in \mathbb{Z}$ and the above relation imply

$$L^2(\mathbb{R}) = \bigoplus_{j=-\infty}^{\infty} W_j.$$

Hence, if we have a function $\psi \in W_0$ such that $\{T_k\psi\}_{k \in \mathbb{Z}}$ is an orthonormal basis for W_0 then ψ is an orthonormal wavelet, i.e. $\{D^j T_k \psi\}_{j, k \in \mathbb{Z}}$ is an orthonormal basis of $L^2(\mathbb{R})$. Every function ψ such that $\{T_k\psi\}_{k \in \mathbb{Z}}$ is an orthonormal basis of W_0 is called an orthonormal wavelet associated with the MRA $\{V_j\}_{j \in \mathbb{Z}}$. If we define ψ by

$$2^{1/2}\hat{\psi}(2\xi) = e^{2\pi i \xi} \overline{m_0(\xi + 1/2)} \hat{\phi}(\xi), \quad \xi \in \mathbb{R},$$

then $\{T_k\psi\}_{k \in \mathbb{Z}}$ is an orthonormal basis for W_0 . For a proof of this result the reader is referred to [60]. The 1-periodic function m_1 , defined by

$$m_1(\xi) = e^{2\pi i \xi} \overline{m_0(\xi + 1/2)},$$

is referred to as the **high pass filter** corresponding to m_0 .

1.3.3 The Fast Wavelet Algorithm

In this section we present the theory of the Fast wavelet transforms associated with the classical MRAs of $L^2(\mathbb{R})$. MRAs provide the mathematical foundation of the transition between analog and digital domains. Fast wavelet algorithms facilitate the analysis of the discrete information representing an analog signal to various levels of lower resolution and detail.

Let P_j be the orthogonal projection operators onto V_j and Q_j the orthogonal projection operators onto W_j . This assumption implies that the original analog signal f has been approximated by $P_j f$, its projection at the resolution level j .

For a given $f \in L^2(\mathbb{R})$ let $c_{j,k}$ and $d_{j,k}$ be defined as follows:

$$c_{j,k} = \langle f, D^j T_k \phi \rangle,$$

$$d_{j,k} = \langle f, D^j T_k \psi \rangle.$$

The coefficients $\{c_{j,k}\}_{k \in \mathbb{Z}}$ essentially are the samples of $P_j f$ at resolution level j , corresponding to a sampling rate proportional to 2^{-j} .

Then P_j and Q_j are given by:

$$P_j(f) = \sum_{k \in \mathbb{Z}} c_{j,k} D^j T_k \phi,$$

$$Q_j(f) = \sum_{k \in \mathbb{Z}} d_{j,k} D^j T_k \psi.$$

For simplicity we assume that the signal lies in V_j for a certain $j \in \mathbb{Z}$. The samples of the signal can be interpreted as the coefficients $c_{j,k}$ of the projection onto V_j . The so called **pyramid algorithm** or **fast wavelet transform** is an iterative scheme that gives $c_{j-1,k}$ and $d_{j-1,k}$ from $c_{j,k}$. Thus, it takes the discrete information corresponding to the projection of f (or $P_j f$) to the next lower resolution level $P_{j-1} f$ and the detail level $Q_{j-1} f$.

Recall,

$$D^{-1} \phi(x) = \sum_{n \in \mathbb{Z}} \alpha_n T_{-n} \phi(x).$$

Now, by applying the unitary operator $D^j T_{2k}$ to this equation, we get,

$$D^{j-1} T_k \phi(x) = \sum_{n \in \mathbb{Z}} \alpha_n D^j T_{2k-n} \phi(x), \quad (1.1)$$

since $T_k D^j = D^j T_{2^j k}$. Hence,

$$\begin{aligned} c_{j-1,k} &= \langle f, D^{j-1} T_k \phi \rangle = \left\langle f, \sum_{n \in \mathbb{Z}} \alpha_n D^j T_{2k-n} \phi \right\rangle \\ &= \sum_{n \in \mathbb{Z}} \overline{\alpha_n} \langle f, D^j T_{2k-n} \phi \rangle = \sum_{n \in \mathbb{Z}} \overline{\alpha_n} c_{j,2k-n}. \end{aligned}$$

Therefore, the coefficients $c_{j-1,k}$ are obtained by convolving $\{\overline{\alpha_n}\}_{n \in \mathbb{Z}}$ with $\{c_{j,k}\}_{k \in \mathbb{Z}}$ followed by downsampling by 2, i.e. keeping only the even entries from the result of the convolution.

Similarly, if

$$D^{-1} \psi(x) = \sum_{n \in \mathbb{Z}} \beta_n T_{-n} \phi(x),$$

applying the unitary operator $D^j T_{2k}$ as above, we obtain

$$D^{j-1} T_k \psi(x) = \sum_{n \in \mathbb{Z}} \beta_n D^j T_{2k-n} \phi(x), \quad (1.2)$$

then similar calculations as above yield

$$d_{j-1,k} = \sum_{n \in \mathbb{Z}} \overline{\beta_n} c_{j,2k-n}.$$

The sequences $\{\overline{\alpha_n}\}_{n \in \mathbb{Z}}$, $\{\overline{\beta_n}\}_{n \in \mathbb{Z}}$ are the impulse responses of the low and high pass filters m_0 and m_1 respectively. These sequences are also referred to as the analysis low and high pass components respectively.

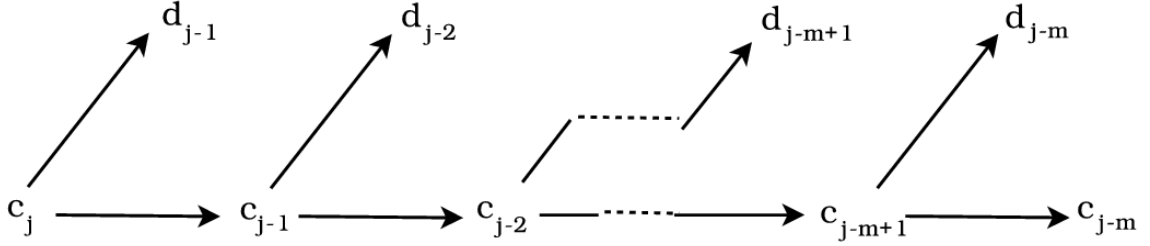


Figure 1.2: Schematic representation of the decomposition algorithm

Now observing that $P_j f = P_{j-1} f + Q_{j-1} f$, and using (1.1) and (1.2) we deduce the reconstruction algorithm as follows,

$$\begin{aligned} \sum_{l \in \mathbb{Z}} c_{j,l} D^j T_l \phi &= \sum_{k \in \mathbb{Z}} c_{j-1,k} D^{j-1} T_k \phi + \sum_{l \in \mathbb{Z}} d_{j-1,k} D^{j-1} T_k \psi \\ &= \sum_{k \in \mathbb{Z}} c_{j-1,k} \left(\sum_{n \in \mathbb{Z}} \alpha_n D^j T_{2k-n} \phi \right) + \sum_{l \in \mathbb{Z}} d_{j-1,k} \left(\sum_{n \in \mathbb{Z}} \beta_n D^j T_{2k-n} \phi \right) \\ &= \sum_{l \in \mathbb{Z}} \left\{ \sum_{k \in \mathbb{Z}} [c_{j-1,k} \alpha_{2k-l} + d_{j-1,k} \beta_{2k-l}] \right\} D^j T_l \phi. \end{aligned}$$

Thus,

$$c_{j,l} = \sum_{k \in \mathbb{Z}} [c_{j-1,k} \alpha_{2k-l} + d_{j-1,k} \beta_{2k-l}]. \quad (1.3)$$

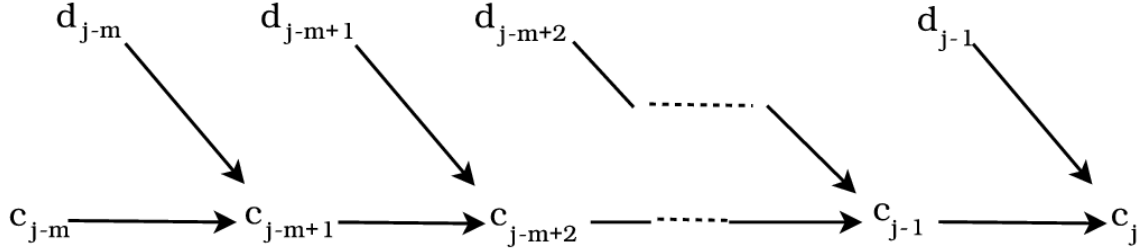


Figure 1.3: Schematic representation of the reconstruction algorithm

Each of the summands in (1.3), represented by an arrow in Figure 1.3, is a convolution.

To see this consider, for j fixed,

$$\tilde{c}_n = \begin{cases} c_{j-1, \frac{n}{2}} & \text{if } n \text{ is even,} \\ 0 & \text{otherwise;} \end{cases}$$

and $\tilde{\alpha}_n = \alpha_{-n}$. Then

$$(\tilde{c} * \tilde{\alpha})_l = \sum_{n \in \mathbb{Z}} \tilde{c}_n \tilde{\alpha}_{l-n} = \sum_{k \in \mathbb{Z}} \tilde{c}_{2k} \tilde{\alpha}_{l-2k} = \sum_{k \in \mathbb{Z}} c_{j-1, k} \alpha_{2k-l}.$$

Thus, each arrow in the figure requires an upsampling by 2 followed by a convolution.

The sequences $\{\alpha_{-n}\}_{n \in \mathbb{Z}}$, $\{\beta_{-n}\}_{n \in \mathbb{Z}}$ are referred to as the synthesis low and high pass respectively.

This decomposition and reconstruction can be presented in a more elegant operator theoretic setting. This will facilitate the understanding of fast algorithms for the more intricate IMRA discussed later. To this end we define $Y : V_0 \rightarrow L^2(\mathbb{T})$ by

$$Y(f) = \sum_{k \in \mathbb{Z}} \langle f, T_k \phi \rangle e_k. \tag{1.4}$$

Since $\{T_k \phi\}_{k \in \mathbb{Z}}$ is an orthonormal basis for V_0 , we get

$$Y(T_k \phi) = e_k.$$

Thus, Y is a surjective isometry and is our sampling operator, or the converter between the analog and the digital domains. Note that when ϕ is a Parseval frame scaling function i.e. when $\{T_k\phi\}_{k \in \mathbb{Z}}$ is a Parseval frame and not an orthonormal basis of V_0 , Y is not surjective. If $a_k = \langle f, T_k\phi \rangle$, then

$$Y\left(\sum_{k \in \mathbb{Z}} a_k T_k\phi\right) = \sum_{k \in \mathbb{Z}} a_k e_k = w,$$

equivalently, for every $g \in V_0$, $Y(g) = w$ if and only if $\hat{g} = w\hat{\phi}$. In particular, we have $Y(D^*\phi) = m_0$. Now,

$$P_{-1}f = \sum_{k \in \mathbb{Z}} \tilde{a}_k D^* T_k\phi = \sum_{k \in \mathbb{Z}} \tilde{a}_k T_{2k} D^* \phi.$$

Denoting the Fourier Transform by \wedge , we obtain

$$(P_{-1}f)^\wedge = \sum_{k \in \mathbb{Z}} \tilde{a}_k e_{2k} (D^*\phi)^\wedge = \sum_{k \in \mathbb{Z}} \tilde{a}_k e_{2k} D\hat{\phi} = w_1(2.)m_0\hat{\phi}, \quad (1.5)$$

where $w_1 = \sum_{k \in \mathbb{Z}} \tilde{a}_k e_k$. $YP_{-1}Y^*$ is the orthogonal projection, onto $Y(V_{-1})$ and using (1.5) we infer

$$YP_{-1}f = w_1(2.)m_0. \quad (1.6)$$

Note that in Equation (1.5) we don't have f in the RHS. Obviously, we must find out how to obtain w_1 from f . Next we discuss this problem.

Let us analyze Equation (1.5). The function $w_1(2.)$ can be expanded in terms of the even modulations only. Notice that $w_1(2.)$ is already upsampled. Its Fourier coefficients are the terms of $\{\tilde{a}_k\}_{k \in \mathbb{Z}}$. This formula is implemented by the low pass branch of the reconstruction algorithm, because we multiply $w_1(2.)$ with the low pass filter m_0 , usually referred to as the reconstruction (synthesis) low pass filter.

The problem we now have to address is how to compute \tilde{a}_k from the Fourier coefficients a_k of the expansion of f with respect to $\{T_k\phi\}_{k \in \mathbb{Z}}$. First, we introduce the operator

$\mathcal{U} : l^2(\mathbb{Z}) \rightarrow l^2(\mathbb{Z})$ defined by

$$\mathcal{U}a(k) = \begin{cases} a(k/2) & k \text{ even,} \\ 0 & \text{otherwise.} \end{cases}$$

If \mathcal{F} is the Fourier Transform on $l^2(\mathbb{Z})$, then $\widehat{\mathcal{U}}w(\xi) = w(2\xi)$, $\xi \in \mathbb{T}$ where $\widehat{\mathcal{U}} = \mathcal{F}\mathcal{U}\mathcal{F}^*$. We also define $\mathcal{D} : l^2(\mathbb{Z}) \rightarrow l^2(\mathbb{Z})$ by

$$\begin{aligned} \mathcal{D}a(k) &= a(2k), \quad \text{or equivalently,} \\ \widehat{\mathcal{D}}w(\xi) &= \frac{1}{2} \left(w\left(\frac{\xi}{2}\right) + w\left(\frac{\xi}{2} + \frac{1}{2}\right) \right). \end{aligned}$$

\mathcal{D} is called the downsampling operator and \mathcal{U} is called the upsampling operator. Note that $\mathcal{U}^* = \mathcal{D}$ and \mathcal{U} is an isometry, while \mathcal{D} is only a partial isometry. Using the definition of Y we obtain

$$a_k = \langle f, T_k\phi \rangle = \langle Yf, Y(T_k\phi) \rangle = \langle Yf, e_k \rangle.$$

Observe that $\{e_{2l}m_0\}_{l \in \mathbb{Z}}$ is an orthonormal basis for $Y(V_{-1})$ because

$$Y(D^*T_l\phi) = Y(T_{2l}D^*\phi) = YT_{2l}Y^*(YD^*\phi) = M_{2l}m_0 = e_{2l}m_0,$$

and $\{D^*T_l\phi\}_{l \in \mathbb{Z}}$ is an orthonormal basis of V_{-1} . Since $YP_{-1}Y^*$ is an orthogonal projection and $Yf = w$, we obtain

$$\begin{aligned} \tilde{a}_k &= \langle P_{-1}f, D^*T_k\phi \rangle = \langle YP_{-1}f, YD^*T_k\phi \rangle \\ &= \langle (YP_{-1}Y^*)(Yf), e_{2k}m_0 \rangle = \langle w, e_{2k}m_0 \rangle = \langle w\overline{m_0}, e_{2k} \rangle. \end{aligned}$$

Therefore, \tilde{a}_k is the $2k$ -th Fourier coefficient of $w\overline{m_0}$ and

$$w_1 = \widehat{\mathcal{D}}(\overline{m_0}w). \tag{1.7}$$

Thus, the decomposition algorithm gives the coefficients of the expansion of $P_{-1}f$ with respect to the basis $\{D^*T_k\phi\}_{k \in \mathbb{Z}}$. The reconstruction algorithm forms $P_{-1}f$, which is the

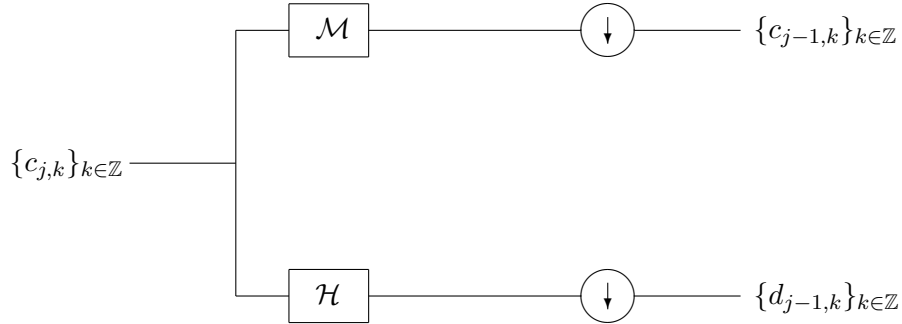


Figure 1.4: Flow diagram for one level of decomposition

actual image captured at the resolution level -1 , i.e. the projection one level below the input analog image. Now, using (1.6) and (1.7) we obtain

$$\begin{aligned} YP_{-1}Y^*w &= YP_{-1}f = m_0(\widehat{U}w_1) \\ &= m_0\widehat{U}\widehat{D}(\overline{m_0}w) = \widehat{M}^*\widehat{M}w, \end{aligned}$$

where $\widehat{M}w = \widehat{D}(\overline{m_0}w)$ for all $w \in L^2(\mathbb{T})$. Similar arguments are true for the high pass filter m_1 and the associated filtering operators $\mathcal{H}, \mathcal{H}^*$. The flow diagrams for decomposition and reconstruction are shown in Figures 1.4 and 1.5.

Finally, since $P_{-1} + Q_{-1} = I|_{V_0}$, we obtain,

$$I = \mathcal{M}^*\mathcal{M} + \mathcal{H}^*\mathcal{H}.$$

This is known as the exact reconstruction formula. We close this section by remarking that in most applications we don't know a_k . So we use the samples of the function $f \in V_0$ instead of the coefficients a_k .

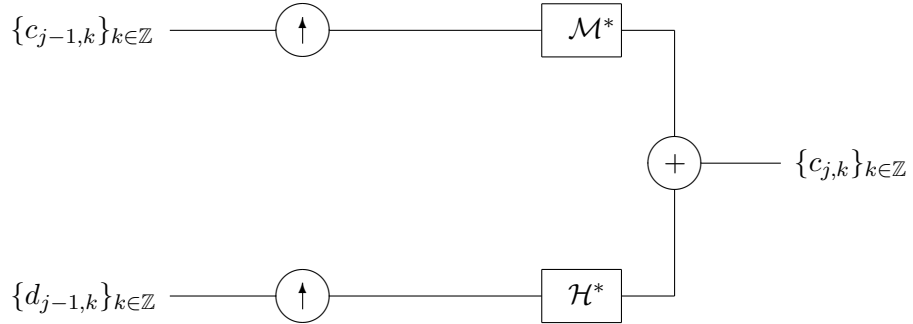


Figure 1.5: Flow diagram for one level of reconstruction

1.4 Frames

Next we define the concepts of frames and Bessel families on a separable Hilbert space H .

Definition 1.4.1 Let $(H, \langle \cdot, \cdot \rangle_H)$ be a separable Hilbert space. A subset $\{f_n\}_{n \in \Lambda}$ of H , where Λ is a countable indexing set, is called a **frame** if and only if there exist two constants $0 < A, B < +\infty$, such that

$$A\|g\|_H^2 \leq \sum_{n \in \Lambda} |\langle g, f_n \rangle_H|^2 \leq B\|g\|_H^2, \quad \text{for all } g \in H. \quad (1.8)$$

The set, $\{f_n\}_{n \in \Lambda}$, is called a **Bessel family** if only the upper bound, B , in (1.8) exists and $A = 0$. The minimum constant B for which (1.8) holds is called the **upper Bessel bound** or the **upper frame bound**. The optimal constant A for which (1.8) holds is called the **lower frame bound**.

If $A = B = 1$ then we refer to the frame as **Parseval**. In this case we have the following reconstruction formula:

$$g = \sum_{n \in \Lambda} \langle g, f_n \rangle_H f_n \quad \text{for all } g \in H.$$

Let K be a separable Hilbert space with an orthonormal basis $\{e_n\}_{n \in \Lambda}$. The operator, $S : K \rightarrow H$, defined via $S(e_n) = f_n$, is called the **synthesis operator** for the family $\{f_n\}_{n \in \Lambda}$. If $\{f_n\}_{n \in \Lambda}$ is Bessel then S can be extended to a bounded linear operator. The adjoint of this operator is given by, $S^*(f) = \sum_{n \in \Lambda} \langle f, f_n \rangle e_n$ for all $f \in H$. We refer to S^* as the **analysis operator** for $\{f_n\}_{n \in \Lambda}$. The operator SS^* is referred to as the **frame operator**. A restatement of the above reconstruction formula is: $SS^* = I_H$ if and only if $\{f_n\}_{n \in \Lambda}$ is a Parseval frame.

Let $\{f_n\}_{n \in \Lambda}$ and $\{\tilde{f}_n\}_{n \in \Lambda}$ be frames of H . If

$$g = \sum_{n \in \Lambda} \langle g, \tilde{f}_n \rangle_H f_n$$

holds for all $g \in H$, then $\{f_n\}_{n \in \Lambda}$ and $\{\tilde{f}_n\}_{n \in \Lambda}$ are a pair of **dual frames**. In operator theoretic language, if S and \tilde{S} are the synthesis operators for $\{f_n\}_{n \in \Lambda}$ and $\{\tilde{f}_n\}_{n \in \Lambda}$ respectively, then $\{f_n\}_{n \in \Lambda}$ and $\{\tilde{f}_n\}_{n \in \Lambda}$ are dual to each other if and only if $S(\tilde{S})^* = I_H$. For more details on frames, the reader is referred to [28].

Chapter 2

Isotropic Multi-Resolution Analysis

2.1 Isotropic Multiresolution Analysis of $L^2(\mathbb{R}^d)$

We begin this chapter by defining an Isotropic Multiresolution Analysis (IMRA) of $L^2(\mathbb{R}^d)$ (see [96]). We drop the assumption of the existence of a scaling function, translates of which form a Riesz basis or a frame for the core subspace V_0 . Instead, we assume that the core subspace is invariant under all rotations, and under translations by integers. As we shall see in subsequent chapters, this definition gives us a lot of flexibility in designing wavelet transforms for applications.

Definition 2.1.1 *An Isotropic Multiresolution Analysis (IMRA) of $L^2(\mathbb{R}^d)$ with respect to a radially expansive matrix A (see Definition 1.2.1 and the subsequent discussion), is a sequence $\{V_j\}_{j \in \mathbb{Z}}$ of closed subspaces of $L^2(\mathbb{R}^d)$ satisfying the following conditions:*

- $\forall j \in \mathbb{Z}, V_j \subset V_{j+1},$
- $(D_A)^j V_0 = V_j,$

- $\cup_{j \in \mathbb{Z}} V_j$ is dense in $L^2(\mathbb{R}^d)$,
- $\cap_{j \in \mathbb{Z}} V_j = \{0\}$,
- V_0 is invariant under all translations $T_{\mathbf{k}}$ such that $\mathbf{k} \in \mathbb{Z}^d$,
- V_0 is invariant under all rotations, i.e.,

$$\mathcal{O}(R)V_0 = V_0 \quad \text{for all } R \in SO(d), \quad (2.1)$$

where $\mathcal{O}(R)$ is the unitary operator given by $\mathcal{O}(R)f(x) := f(R^T x)$ a.e. with $f \in L^2(\mathbb{R}^d)$ and $R \in SO(d)$ and R^T is the transpose of the matrix R .

Although the last two properties of Definition 2.1.1 appear not to be sufficiently strong to yield rigid motion covariant wavelet decompositions, they force all the resolution subspaces V_j of an IMRA to be invariant under all rigid motions in any number of dimensions (Theorem 2.2.1). This strong result follows from the characterization of all IMRAs by means of the Lax-Wiener Theorem [74] which is the topic of the next section.

2.2 Characterization of IMRAs

As we will see, Equation (2.1) imposes an algebraic-geometric constraint on the space V_0 : Assume V is a shift-invariant subspace of $L^2(\mathbb{R}^d)$ also satisfying (2.1). Then, for every $R \in SO(d)$ and $\mathbf{k} \in \mathbb{Z}^d$, we have

$$T_{\mathbf{k}}\mathcal{O}(R) = \mathcal{O}(R)T_{R^T\mathbf{k}}.$$

Thus, we obtain $\mathcal{O}(R)T_{R^T\mathbf{k}}V = T_{\mathbf{k}}\mathcal{O}(R)V = V$ yielding

$$T_{R^T\mathbf{k}}V = V, \quad \text{for every } R \in SO(d) \text{ and } \mathbf{k} \in \mathbb{Z}^d. \quad (2.2)$$

Since $SO(d)$ acts transitively on spheres centered at the origin, the orbit $\{R\mathbf{x} : R \in SO(d)\}$ of any \mathbf{x} in \mathbb{R}^d is the entire sphere of radius $\|\mathbf{x}\|$. In particular, if $\mathbf{x} = (1, 1, \dots, 1)$, then, Equation (2.2) implies that V remains invariant under all translations by $T_{\mathbf{y}}$ with $\mathbf{y} \in \sqrt{d} \cdot \mathbb{S}^{d-1}$ and thus also by translations $T_{\mathbf{y}}$ with $\mathbf{y} \in \sqrt{d} \mathbb{S}^{d-1} - \sqrt{d} \mathbb{S}^{d-1}$, which contains the fundamental domain $\mathbb{T}^d := [-\frac{1}{2}, \frac{1}{2}]^d$. Hence, we conclude that $T_{\mathbf{y}}(V) = V$ for all $\mathbf{y} \in \mathbb{T}^d$. Since the same identity is true for all $\mathbf{y} \in \mathbb{Z}^d$ we assert that V remains invariant under all translations induced by \mathbb{R}^d . This implies that V is a Wiener subspace of $L^2(\mathbb{R}^d)$, so there exists a measurable subset Ω of \mathbb{R}^d such that $V = PW_{\Omega}$. The fact that V remains invariant by all rotations now implies that Ω is radial. On the other hand, if Ω is radial we obviously have that $V = PW_{\Omega}$ remains invariant under all rotations and translations induced by \mathbb{Z}^d . Therefore, we have proved the following characterization of shift-invariant and rotation invariant subspaces of $L^2(\mathbb{R}^d)$.

Theorem 2.2.1 *Let V be an invariant subspace of $L^2(\mathbb{R}^d)$ under the action of the translation group induced by \mathbb{Z}^d . Then V remains invariant under all rotations if and only if $V = PW_{\Omega}$ for some radial measurable subset Ω of \mathbb{R}^d .*

As an immediate consequence we obtain a characterization of IMRAs generated by a single function, in the sense that there exists function φ such that $V_0 = \langle \varphi \rangle$.

Proposition 2.2.2 *Let A be a radially expansive matrix and $C := A^*$. A sequence $\{V_j\}_{j \in \mathbb{Z}}$ is an IMRA with respect to A if and only if $V_j = PW_{C^j \Omega}$, where Ω is radial and satisfies*

(i) $\Omega \subset C\Omega$.

(ii) The set-theoretic complement of $\cup_{j=1}^{\infty} C^j \Omega$ is null.

(iii) $\lim_{j \rightarrow \infty} |C^{-j} \Omega| = 0$.

2.2. CHARACTERIZATION OF IMRAS

Moreover the only singly generated IMRAs are precisely $V_j = PW_{C^j\Omega}$, where Ω is a radial subset of \mathbb{T}^d satisfying (i), (ii) and (iii).

Proof: If $\{V_j\}$ is an IMRA, then V_0 satisfies Equation (2.1). By the previous theorem, $V_0 = PW_\Omega$ for some set $\Omega \subset \mathbb{R}^d$. Thus, $V_j = PW_{C^j\Omega}$. Properties (i), (ii), and (iii) are now obvious.

On the other hand if $V_j = PW_{C^j\Omega}$, for some radial subset Ω , and conditions (i), (ii) and (iii) are satisfied, then clearly $\{V_j\}$ is an Isotropic Multiresolution Analysis.

Now, suppose that $V_0 = \langle \phi \rangle$. Then $\text{supp}\phi = \Omega$ where the equality must be perceived in the measure-theoretic sense. We will prove $\Omega \subseteq \mathbb{T}^d$. Since, $\Phi_\phi(\boldsymbol{\xi}) := \sum_{\mathbf{k} \in \mathbb{Z}^d} |\widehat{\phi}(\boldsymbol{\xi} + \mathbf{k})|^2$ is a.e. finite the function ω given by $\widehat{\omega} := \widehat{\phi}\Phi^{-1/2}$ is a Parseval frame generator of V_0 , i.e. $\{T_n\omega : n \in \mathbb{Z}^d\}$ is a Parseval frame of V_0 , because $\Phi_\omega(\boldsymbol{\xi}) := \sum_{\mathbf{k} \in \mathbb{Z}^d} |\widehat{\omega}(\boldsymbol{\xi} + \mathbf{k})|^2 = \chi_{\mathcal{E}}$, where \mathcal{E} is a subset of \mathbb{T}^d e.g. [12, 16, 87]. Consequently, there exists a family $\{\mathcal{L}_{\mathbf{k}}\}_{\mathbf{k} \in \mathbb{Z}^d}$ of mutually disjoint measurable subsets of \mathbb{T}^d such that $\cup_{\mathbf{k} \in \mathbb{Z}^d} (\mathbf{k} + \mathcal{L}_{\mathbf{k}}) = \Omega$, where this equality is again meaningful only in a measure-theoretic sense, for if it is not true there exists a subset \mathcal{U} of \mathbb{T}^d with positive measure and $\mathbf{l}_1, \mathbf{l}_2$ in \mathbb{Z}^d , $\mathbf{l}_1 \neq \mathbf{l}_2$, such that $\mathcal{U} + \mathbf{l}_1$ and $\mathcal{U} + \mathbf{l}_2$ are contained in Ω . Then, the inverse Fourier transform $(\chi_{\mathcal{U} + \mathbf{l}_1})^\vee$ belongs to V_0 , so

$$\chi_{\mathcal{U} + \mathbf{l}_1} = m\widehat{\omega}, \quad (2.3)$$

with $m \in L^2(\mathbb{T}^d)$. Since $\text{supp}\widehat{\omega} = \Omega$ and m is \mathbb{Z}^d -periodic, we conclude $m(\boldsymbol{\xi})\widehat{\omega}(\boldsymbol{\xi}) \neq 0$ a.e. on $\mathcal{U} + \mathbf{l}_2$ which is disjoint from $\mathcal{U} + \mathbf{l}_1$. This conclusion directly contradicts (2.3), so our claim is proved.

Next, we claim that the previously established property of Ω combined with its radially imply $\Omega \subseteq \mathbb{T}^d$. To prove this claim, assume that the contrary is true. Then, there exists a point of density $\boldsymbol{\xi}_0$ of Ω and $p \in \mathbb{Z}^+$ such that $\boldsymbol{\xi}_0 \in (p\mathbf{i} + \mathbb{T}^d)$, where $\mathbf{i} = (1, 0, \dots, 0)$.

2.2. CHARACTERIZATION OF IMRAS

Consequently, every point on $\|\xi_0\|\mathbb{S}^{d-1}$ is a density point of Ω . Let, $C_1 := \|\xi_0\|\mathbb{S}^{d-1} \cap (p\mathbf{i} + \mathbb{T}^d) \neq \emptyset$ and $C_2 := \|\xi_0\|\mathbb{S}^{d-1} \cap (p\mathbf{j} + \mathbb{T}^d) \neq \emptyset$, where $\mathbf{j} = (0, 1, \dots, 0)$. Since every point in both C_1 and C_2 is a density point of Ω , these two sets must be contained in $p\mathbf{i} + \mathcal{L}_{p\mathbf{i}}$ and $p\mathbf{j} + \mathcal{L}_{p\mathbf{j}}$ respectively, where $\mathcal{L}_{p\mathbf{i}}$ and $\mathcal{L}_{p\mathbf{j}}$ are disjoint. But, $-p\mathbf{i} + C_1$ and $-p\mathbf{j} + C_2$ intersect at a density point of both $\mathcal{L}_{p\mathbf{i}}$ and $\mathcal{L}_{p\mathbf{j}}$ contradicting the fact that these two sets are disjoint. Thus, $\Omega \subseteq \mathbb{T}^d$. The converse implication is obvious. \square

Remark 2.2.3 If $V = PW_\Omega$, for some radial subset Ω we can find a subset $F \subset L^2(\mathbb{R}^d)$ with $V = \overline{\text{span}\{T_{\mathbf{k}}f : f \in F, \mathbf{k} \in \mathbb{Z}^d\}}$ and this set is at most countably infinite. To show the existence of such a set it suffices to apply Zorn's lemma. The construction of the set of generator F is non-trivial but it does not interest us here. If Ω is essentially bounded, then every f in F can be chosen to satisfy $\{\xi \in \mathbb{R}^d : \widehat{f}(\xi) \neq 0\} = \Omega$ with F finite.

Example 2.2.4 The sequence of closed subspaces $V_j = PW_{2^j B(0, \rho)}$, for any $\rho > 0$ and $j \in \mathbb{Z}$ is an IMRA.

The purpose of the next two examples is to show that: First, Ω can be unbounded, and second, Ω may not contain a neighborhood of the origin. Notice that such a neighborhood is sufficient for Condition (ii). In both examples we use dyadic dilations.

Example 2.2.5 Denote by $B(0, r, s)$ the (d -dimensional) spherical shell centered at the origin having inner radius r and outer radius s . Now for simplicity set $d = 2$ although this example can be generalized for every $d > 2$. Let $\mathbf{A} = \bigcup_{n=1}^{\infty} B(0, r_n, 2^{n-1})$, with $r_n = 2^{n-1} - (1/16)^n$, and let $\mathbf{B} = B(0, 1/2)$. Set $\Omega := \mathbf{A} \cup \mathbf{B}$. Since \mathbf{A} and \mathbf{B} are disjoint, $|\mathbf{A} \cup \mathbf{B}| = |\mathbf{A}| + |\mathbf{B}|$. Moreover, both \mathbf{A} and \mathbf{B} have finite measure. Since $|B(0, r_n, 2^{n-1})| = \pi[(1/8)^n - (1/16)^{2n}]$ which implies $|\mathbf{A}| < \infty$. Thus, Ω is radial and satisfies all the conditions

(i)-(iii) of Proposition 2.2.2: (i) is satisfied because $B(0, r_{n+1}, 2^n) \subset 2B(0, r_n, 2^{n-1})$ for all $n \geq 1$ and $B(0, r_1, 1) \subset 2\mathbf{B}$; (ii) is trivially satisfied since \mathbf{B} is contained in Ω . The fact that Ω has finite measure implies (iii). Thus, Ω gives rise to an Isotropic Multiresolution Analysis, but Ω is not bounded.

Example 2.2.6 This example is valid for every $d \geq 2$. Let $\Omega = \bigcup_{n=1}^{\infty} B(0, (1/2)^{n+1}, r_n)$, with $r_n = (1/2)^n - (1/100)^n$. Obviously, Ω contains no neighborhood of the origin. According to Proposition 2.2.2, and since $\Omega \subseteq B(0, 1/2)$, it is enough to prove that the complement of $\bigcup_{n=1}^{\infty} 2^j \Omega$ is null and $\Omega \subset 2\Omega$ in order to establish that Ω defines an IMRA. Let us first show that (i) of Proposition 2.2.2 is satisfied. This property holds because $2B(0, (1/2)^{n+1}, r_n) = B(0, (1/2)^n, 2r_n)$ and $r_{n-1} < 2r_n$ for all $n \geq 2$.

We now prove that (ii) is satisfied.

Let $\mathbf{x} \in \mathbb{R}^d$ and $j_{\mathbf{x}} \in \mathbb{Z}$ such that $2^{j_{\mathbf{x}}-1} < \|\mathbf{x}\| < 2^{j_{\mathbf{x}}}$. Then,

$$\frac{1}{4} < \left\| \frac{\mathbf{x}}{2^{j_{\mathbf{x}}+1}} \right\| < \frac{1}{2}.$$

However,

$$\lim_{n \rightarrow \infty} \frac{r_n - 2^{-(n+1)}}{2^{-(n+1)}} = 1,$$

so there exists positive integer $n_{\mathbf{x}}$ satisfying

$$\frac{\left\| \frac{\mathbf{x}}{2^{j_{\mathbf{x}}+1}} \right\| - \frac{1}{4}}{1/4} < \frac{r_{n_{\mathbf{x}}} - 2^{-(n_{\mathbf{x}}+1)}}{2^{-(n_{\mathbf{x}}+1)}}.$$

This implies that $2^{-(j_{\mathbf{x}}+1)}\mathbf{x}$ belongs to the spherical shell $2^{n_{\mathbf{x}}-1}B(0, 2^{-(n_{\mathbf{x}}+1)}, r_{n_{\mathbf{x}}})$, which is equal to $B(0, \frac{1}{4}, 2^{n_{\mathbf{x}}-1}r_{n_{\mathbf{x}}})$. Thus, \mathbf{x} belongs to $2^{n_{\mathbf{x}}+j_{\mathbf{x}}}\Omega$. Our claim now follows from the fact that $\bigcup_{j \in \mathbb{Z}} 2^j \mathbb{S}^{d-1}$ is null.

Remark 2.2.7 Theorem 2.2.1 can be restated in terms of the theory of Von Neumann Algebras: The joint commutant of $\{\mathcal{O}(R) : R \in SO(d)\}$ and $\mathfrak{T}_{\mathbb{Z}^d}$, on one hand, and the

joint commutant of $\{\mathcal{O}(R) : R \in SO(d)\}$ and $\mathfrak{T}_{\mathbb{R}^d}$ on the other hand coincide. This follows from the fact that the orthogonal projections in these two joint commutants are exactly the same, as Theorem 2.2.1 suggests. Here, \mathfrak{T}_G denotes the group of translations induced by a subgroup G of \mathbb{R}^d .

So far, we have characterized the ‘core’ or zero-resolution subspaces V_0 of IMRAs. We also note that if these are singly generated then the choices for ‘core’ IMRA-subspaces are all of one kind: PW_Ω with Ω radial and inside the fundamental domain \mathbb{T}^d . In the light of this discussion an interesting open problem is to characterize all sets Ω for which $V_0 = PW_\Omega$ is generated by a fixed number, N , of functions. However, none of these generators can be compactly supported in the spatial domain: If one of them, say ϕ_1 , is compactly supported then $\widehat{\phi}_1$ has analytic extension on the complex domain \mathbb{C}^d . Then $\widehat{\phi}_1$ can vanish only on a set of points with no accumulation point, forcing $\Omega = \mathbb{R}^d$ which, in turn, implies $V_0 = L^2(\mathbb{R}^d)$ which contradicts the IMRA-definition.

2.3 Isotropic Refinable Functions and IMRAs

According to Proposition 2.2.2 a single refinable function ϕ defines an IMRA by letting $V_0 = \overline{\text{span}}\{T_{\mathbf{k}}\phi : \mathbf{k} \in \mathbb{Z}^d\}$, if ϕ is radial and the support of $\widehat{\phi}$ is contained in the fundamental domain \mathbb{T}^d . This observation motivates us to characterize radial and, more generally, isotropic refinable functions (Theorem 2.3.1) with respect to dilations defined by radially expansive matrices. The purpose of this section is to characterize these functions. As we will see not all of these functions generate ‘core’ IMRA-subspaces, because their support in the frequency domain does not have to be contained in the fundamental domain.

Let A be a radially expansive matrix. With respect to dilations induced by A , a

function ϕ in $L^2(\mathbb{R}^d)$ is called **refinable** if there exists a measurable, essentially bounded, \mathbb{Z}^d -periodic function H such that $\widehat{\phi}(A^*\xi) = H(\xi)\widehat{\phi}(\xi)$, a.e. $\xi \in \mathbb{R}^d$. The function H is called the **low-pass filter** or **mask** corresponding to ϕ .

Theorem 2.3.1 *Let A be a radially expansive matrix and $\phi \in L^2(\mathbb{R}^d)$ be a refinable function and $H \in L^\infty(\mathbb{T}^d)$ be its mask. We also assume that*

1. ϕ is isotropic, and
2. $\lim_{\xi \rightarrow 0} \widehat{\phi}(\xi) = L \neq 0$.

Then $\phi \in PW_{\rho/(\rho+1)}$, where $\rho = |\det A|^{1/d}$ is the dilation factor of A .

The proof of this theorem is presented in [96]. Here we shall consider the following two important ramifications of Theorem 2.3.1. The first corollary follows from the fact that $\widehat{\phi}$ is compactly supported.

Corollary 2.3.2 *There is no isotropic, refinable function that is compactly supported in the spatial domain.*

Next, recall that according to Proposition 2.2.2 the refinable functions generating an integer shift and rotation-invariant subspace of $L^2(\mathbb{R}^d)$ belong to the Paley-Wiener space $PW_{\mathbb{T}^d}$. So if a refinable function ϕ is isotropic and *does not* belong to $PW_{\mathbb{T}^d}$, does it define an IMRA? The answer is provided by the next corollary.

Corollary 2.3.3 *If an MRA is defined by a single isotropic refinable function ϕ whose Fourier transform is supported outside the ball of radius $1/2$ centered at the origin is not an IMRA; equivalently, the orthogonal projection onto V_0 does not commute with all rotations.*

We remark that Theorem 2.3.1 is not true for a non-singleton refinable set $\{\phi_l : l \in \mathbb{N}\}$, a set for which there exists an essentially bounded $\infty \times \infty$ -matrix valued \mathbb{Z}^d -periodic function H satisfying

$$(\widehat{\phi}_1(A^*\cdot), \widehat{\phi}_2(A^*\cdot), \dots)^T = H(\widehat{\phi}_1, \widehat{\phi}_2, \dots)^T \quad \text{a.e. on } \mathbb{R}^d,$$

where even at least one ϕ_l satisfies the hypotheses of the theorem. As an example, consider the set $\{\phi_1, \phi_2\}$, where $\widehat{\phi}_1 = \chi_{B(0,1/2)}$, the characteristic function of the ball centered at the origin and radius $1/2$, and $\widehat{\phi}_2 = \chi_{B(0,1/2,1)}$, the characteristic function of the annulus with inner radius $1/2$ and outer radius 1 . Let $A = 2I_{L^2(\mathbb{R}^d)}$, the dyadic dilation matrix. Then the set $\{\phi_1, \phi_2\}$ satisfies the following refinement equation:

$$\begin{bmatrix} \widehat{\phi}_1(2\cdot) \\ \widehat{\phi}_2(2\cdot) \end{bmatrix} = \begin{bmatrix} H_1 & 0 \\ H_2 & 0 \end{bmatrix} \begin{bmatrix} \widehat{\phi}_1 \\ \widehat{\phi}_2 \end{bmatrix} \quad \text{on } \mathbb{R}^d,$$

where H_1 is a \mathbb{Z}^d -periodic function whose restriction to \mathbb{T}^d is $\chi_{B(0,1/4)}$, and H_2 is a \mathbb{Z}^d -periodic function whose restriction to \mathbb{T}^d is $\chi_{B(0,1/4,1/2)}$. Since $\rho = 2$ for dyadic dilation, according to the theorem the scaling function should belong to $PW_{2/3}$. But, as is evident, ϕ_2 does not belong to $PW_{2/3}$.

Chapter 3

Isotropic Wavelets from Extension Principles

In Section 2.3, we prove that the singly generated IMRAs are the ones for which the scaling function is supported inside the ball of radius $1/2$. Now, if we want the integer translates of such a scaling function to form a frame, then its Fourier transform must necessarily be discontinuous (see Theorem 7.2.3 in [28]). Such a frame is useless in applications because it lacks good spatial localization. To secure the latter property, we use generators for V_0 whose Fourier transforms are C^∞ . Then the classical methods for the construction of wavelets (See Section 1.3.2 for orthonormal wavelets and [11, 12] for frame wavelets) do not work anymore. On the other hand, if the stability of the generator is the issue, i.e. if we want its integer translates to form a frame, then the solution is easy; take the generator to be $\mathcal{F}^{-1}(\chi_{\text{supp}(\widehat{\phi})})$, where ϕ is the well-localized generator of an IMRA and as mentioned, $\text{supp}(\phi) \subseteq \mathbb{T}^d$. But the construction of wavelets associated with this IMRA will require the use of a high-pass filter whose transfer function is of the form $\chi_{\text{supp}(\widehat{\phi})} - \chi_{\text{supp}(\widehat{\phi}(A^*\cdot))}$.

So the lack of smoothness of the generator for V_0 results in the lack of smoothness of the high pass filter. But what is the underlying property that seems to leave us out of choices when we try to follow the classical paths of wavelet construction? The answer is the enhanced symmetry of ϕ that we want to impose. Apparently, symmetry imposes limits to stability; we can not turn two knobs to the maximum at the same time! This is true for 1- D wavelet constructions as well. Daubechies, Cohen and Feauveau dropped the orthonormality and instead imposed that $\{T_{\mathbf{k}}\phi\}_{\mathbf{k}\in\mathbb{Z}^d}$ is a Riesz basis for its closed linear span to be able to achieve some symmetry [34]. However, the complete departure from any stability properties for ϕ , gives a lot more freedom in the design. Extension Principles address that fundamental problem in wavelet construction and in digital data processing. When the integer translates of a refinable function do not form a frame for their closed linear span but form only a Bessel family the construction of affine wavelet frames with desirable spatial localization cannot be carried out as in the classical multiresolution theory of Mallat and Meyer. In this case Extension Principles provide the complete answer to this problem, i.e., they characterize the affine families, associated with an MRA, that are frames or yield a pair of dual frames, when the translates of the refinable function only form a Bessel family. In addition they show that if we use the refinable function and the resulting wavelets for multiscale signal decompositions these decompositions are implementable with fast algorithms just as in the classical MRA theory. We don't want to further discuss the significance of the Extension Principles in wavelets and multiscale transforms in general. The interested reader may refer to the celebrated first paper on the topic due to Ron and Shen [97] and for nice overviews on the topic to the relevant chapter of [29] and to [38].

3.1 Extension Principles Revisited

For a given refinable function ϕ , we denote by V_0 the closed subspace $\overline{\text{span}} \{T_{\mathbf{k}}\phi\}_{\mathbf{k} \in \mathbb{Z}^d}$. We do not necessarily require that $\{T_{\mathbf{k}}\phi\}_{\mathbf{k} \in \mathbb{Z}^d}$ is a frame. In other words, we completely drop the stability requirements for ϕ . The spectrum of ϕ , denoted by $\sigma(V_0)$, is defined by (see, e.g., [15])

$$\sigma(V_0) := \left\{ \boldsymbol{\xi} \in \mathbb{T}^d : \sum_{\mathbf{k}} |\hat{\phi}(\boldsymbol{\xi} + \mathbf{k})|^2 > 0 \right\}.$$

The next theorem is one of the main results in [97] and is the cornerstone of the Unitary Extension Principle [97], but it also appears in [38] with different assumptions on ϕ where it is used to formulate the so-called Oblique Extension Principle. The notation and assumptions used here are those from [38].

Theorem 3.1.1 [38] *Let ϕ be a refinable function in $L^2(\mathbb{R}^d)$ such that $\hat{\phi}$ is continuous at the origin,*

$$\lim_{|\boldsymbol{\xi}| \rightarrow 0} \hat{\phi}(\boldsymbol{\xi}) = 1. \quad (3.1)$$

Assume that there exists a constant $B > 0$ such that $\sum_{\mathbf{l} \in \mathbb{Z}^d} |\hat{\phi}(\boldsymbol{\xi} + \mathbf{l})|^2 \leq B$ a.e. on \mathbb{R}^d and that ϕ is refinable with respect to the expansive matrix A , i.e. there exists a \mathbb{Z}^d -periodic measurable function H_0 , such that

$$\hat{\phi}(A^* \cdot) = H_0 \hat{\phi}. \quad (3.2)$$

Furthermore, let H_i , $i = 1, \dots, m$, be \mathbb{Z}^d -periodic measurable functions and define m wavelets ψ_i , $i = 1, \dots, m$, by

$$\hat{\psi}_i(A^* \cdot) = H_i \hat{\phi}. \quad (3.3)$$

Assume $H_i \in L^\infty(\mathbb{T}^d)$ for all $i = 0, \dots, m$, then the following two conditions are equivalent:

1. *The set $\left\{ D_A^j T_{\mathbf{k}} \psi_i : j \in \mathbb{Z}, \mathbf{k} \in \mathbb{Z}^d, i = 1, \dots, m \right\}$ is a Parseval frame for $L^2(\mathbb{R}^d)$.*

2. For all $\boldsymbol{\xi} \in \sigma(V_0)$,

(a) $\lim_{j \rightarrow -\infty} \Theta(A^{*j}\boldsymbol{\xi}) = 1.$

(b) If $\mathbf{q} \in (A^{*-1}\mathbb{Z}^d)/\mathbb{Z}^d \setminus \{0\}$ and $\boldsymbol{\xi} + \mathbf{q} \in \sigma(V_0)$, then

$$\Theta(A^*\boldsymbol{\xi})H_0(\boldsymbol{\xi})\overline{H_0(\boldsymbol{\xi} + \mathbf{q})} + \sum_{i=1}^m H_i(\boldsymbol{\xi})\overline{H_i(\boldsymbol{\xi} + \mathbf{q})} = 0,$$

where Θ is the so-called fundamental function, defined by

$$\Theta(\boldsymbol{\xi}) = \sum_{j=0}^{\infty} \sum_{i=1}^m |H_i(A^{*j}\boldsymbol{\xi})|^2 \prod_{l=0}^{j-1} |H_0(A^{*l}\boldsymbol{\xi})|^2.$$

The previous theorem characterizes all Parseval wavelet frames of $L^2(\mathbb{R}^d)$ defined by means of (3.3) from a refinable function satisfying (3.1) and (3.2). If we use several consecutive levels of the multiscale decomposition given by the Parseval frame

$$\left\{ D_A^j T_{\mathbf{k}} \psi_i : j \in \mathbb{Z}, \mathbf{k} \in \mathbb{Z}^d, i = 1, \dots, m \right\},$$

of a signal, say f , then it is like using a partial sum of the series

$$\sum_j \sum_{\mathbf{k}} \langle f, D_A^j T_{\mathbf{k}} \psi_i \rangle D_A^j T_{\mathbf{k}} \psi_i = f,$$

to approximate f . If we are forced to take only a few levels of decomposition, then we wish to use a family augmenting the refinable function and the wavelets such as

$$X_{\phi\psi} := \left\{ D_A^j T_{\mathbf{k}} \psi_i : j \in \mathbb{N} \cup \{0\}, \mathbf{k} \in \mathbb{Z}^d, i = 1, \dots, m \right\} \cup \left\{ T_{\mathbf{k}} \phi : \mathbf{k} \in \mathbb{Z}^d \right\}.$$

If this is the case, e.g. in seismic imaging [62], then it is legitimate to question whether $X_{\phi\psi}$ forms a Parseval frame of $L^2(\mathbb{R}^d)$. This problem is the focus of the present section. The answer to this problem does not follow from Theorem 3.1.1. However, if $X_{\phi\psi}$ is a Parseval frame of $L^2(\mathbb{R}^d)$, then it is also true that $\left\{ D_A^j T_{\mathbf{k}} \psi_i : j \in \mathbb{Z}, \mathbf{k} \in \mathbb{Z}^d, i = 1, \dots, m \right\}$ shares the same property (see Remark 3.1.3 and Corollary 3.1.9). One of the merits of Theorem 3.1.7

is that it imposes minimal conditions on the filters and the refinable function ϕ . In the spirit of Theorem 3.1.7, we have Theorem 3.1.10 which characterizes the Bessel sequence pairs $X_{\phi\psi}^a := X_{\phi^a\psi^a}$ and $X_{\phi\psi}^s := X_{\phi^s\psi^s}$ that are dual frames of $L^2(\mathbb{R}^d)$.

To facilitate the implementation of the decomposition of a multidimensional data set by means of a Parseval frame resulting from Theorems 3.1.1, 3.1.7, 3.1.4, and 3.1.10 we employ the modulation matrix, a concept introduced for filter design in engineering.

Definition 3.1.2 *The modulation matrix \mathbf{H} is defined by*

$$\mathbf{H} = \begin{pmatrix} H_0 & H_1 & \dots & H_m \\ T_{\mathbf{q}_1}H_0 & T_{\mathbf{q}_1}H_1 & \dots & T_{\mathbf{q}_1}H_m \\ \vdots & \vdots & \ddots & \vdots \\ T_{\mathbf{q}_{n-1}}H_0 & T_{\mathbf{q}_{n-1}}H_1 & \dots & T_{\mathbf{q}_{n-1}}H_m \end{pmatrix}, \quad (3.4)$$

where $n = |\det(A^*)|$ and $\mathbf{q}_l : l = 0, 1, 2, \dots, n-1$ are the representatives of the quotient group $(A^{*-1}\mathbb{Z}^d)/\mathbb{Z}^d$.

Remark 3.1.3 (1) A special case of Theorem 3.1.1 occurs when

$$\mathbf{H}\mathbf{H}^* = \begin{pmatrix} \chi_{\sigma(V_0)} & 0 & \dots & 0 \\ 0 & T_{\mathbf{q}_1}\chi_{\sigma(V_0)} & \dots & 0 \\ \vdots & \vdots & \ddots & \vdots \\ 0 & 0 & \dots & T_{\mathbf{q}_{n-1}}\chi_{\sigma(V_0)} \end{pmatrix} \quad (3.5)$$

almost everywhere on \mathbb{T}^d , then the set $\{D_A^j T_{\mathbf{k}}\psi_i : j \in \mathbb{Z}, \mathbf{k} \in \mathbb{Z}^d, i = 1, \dots, m\}$ is a Parseval frame for $L^2(\mathbb{R}^d)$. In this case the fundamental function $\Theta = 1$ a.e. on $\sigma(V_0)$. This special case is referred to as the *Unitary Extension Principle* in [38]. In Theorem 3.1.7 we show that

this condition is equivalent to the set $X_{\phi\psi}$ being a Parseval frame of $L^2(\mathbb{R}^d)$. Corollary 3.1.9 gives that the latter property implies the conclusion of the UEP. However, our assumptions for the refinable function ϕ in Theorem 3.1.7 are more general; we neither impose a decay condition for $\hat{\phi}$ at infinity as [97] does, nor we require that the integral translates of ϕ form a Bessel sequence, as [38] does.

(2) If the spectrum, $\sigma(V_0) = \mathbb{T}^d$ then the condition in (3.5) reduces to $\mathbf{HH}^* = \mathbf{I}$.

(3) For a very interesting direct proof of UEP under the same more general hypotheses we use in Theorem 3.1.7 see [13]; see also [9, 11]. The more general case where the fundamental function is not necessarily equal to one is referred to in [38] as the *Oblique Extension Principle*.

The next theorem characterizes pairs of affine families that form dual frames of $L^2(\mathbb{R}^d)$ in terms of conditions on their filters, similar to those in Theorem 3.1.1. The so-called Mixed Extension Principles follow directly from this theorem [38].

Theorem 3.1.4 [38] *Let ϕ^a and ϕ^s be refinable functions in $L^2(\mathbb{R}^d)$ such that $\widehat{\phi}^a$ and $\widehat{\phi}^s$ are continuous at the origin and*

$$\lim_{|\boldsymbol{\xi}| \rightarrow 0} \widehat{\phi}^a(\boldsymbol{\xi}) = \widehat{\phi}^s(\boldsymbol{\xi}) = 1. \quad (3.6)$$

Let H_0^a and $H_0^s \in L^\infty(\mathbb{T}^d)$, be the associated low pass filters. Furthermore, let H_i^a, H_i^s for $i = 1, \dots, m$, be \mathbb{Z}^d -periodic measurable functions and define m pairs of wavelets ψ_i^a, ψ_i^s $i = 1, \dots, m$, by

$$\widehat{\psi}_i^a(A^* \cdot) = H_i^a \widehat{\phi}, \quad (3.7)$$

$$\widehat{\psi}_i^s(A^* \cdot) = H_i^s \widehat{\phi}. \quad (3.8)$$

3.1. EXTENSION PRINCIPLES REVISITED

Assume $H_i^a, H_i^s \in L^\infty(\mathbb{T}^d)$ for all $i = 0, \dots, m$. Then the following two conditions are equivalent,

1. The sets $\Psi^a := \left\{ D_A^j T_{\mathbf{k}} \psi_i^a : j \in \mathbb{Z}, \mathbf{k} \in \mathbb{Z}^d, i = 1, \dots, m \right\}$ and $\Psi^s := \left\{ D_A^j T_{\mathbf{k}} \psi_i^s : j \in \mathbb{Z}, \mathbf{k} \in \mathbb{Z}^d, i = 1, \dots, m \right\}$ is a pair of dual frames for $L^2(\mathbb{R}^d)$.
2. Ψ^a and Ψ^s are Bessel families and for all $\boldsymbol{\xi} \in \sigma(V_0^a) \cap \sigma(V_0^s)$,

(a) $\lim_{j \rightarrow -\infty} \Theta_M(A^{*j} \boldsymbol{\xi}) = 1$,

(b) If $\mathbf{q} \in (A^{*-1}\mathbb{Z}^d)/\mathbb{Z}^d \setminus \{0\}$ and $\boldsymbol{\xi} + \mathbf{q} \in \sigma(V_0^a) \cap \sigma(V_0^s)$, then

$$\Theta_M(A^* \boldsymbol{\xi}) H_0^s(\boldsymbol{\xi}) \overline{H_0^a(\boldsymbol{\xi} + \mathbf{q})} + \sum_{i=1}^m H_i^s(\boldsymbol{\xi}) \overline{H_i^a(\boldsymbol{\xi} + \mathbf{q})} = 0,$$

where Θ_M is the so-called Mixed Fundamental function, defined by

$$\Theta_M(\boldsymbol{\xi}) = \sum_{j=0}^{\infty} \sum_{i=1}^m H_i^s(A^{*j} \boldsymbol{\xi}) \overline{H_i^a(A^{*j} \boldsymbol{\xi})} \prod_{l=0}^{j-1} H_0^s(A^{*l} \boldsymbol{\xi}) \overline{H_0^a(A^{*l} \boldsymbol{\xi})}.$$

Remark 3.1.5 Let \mathbf{H}_a and \mathbf{H}_s denote the modulation matrices corresponding to the filters H_i^a and H_i^s respectively. By Theorem 3.1.4 we conclude that if

$$\mathbf{H}_s \mathbf{H}_a^* = \begin{pmatrix} \chi_{\sigma(V_0^a) \cap \sigma(V_0^s)} & 0 & \dots & 0 \\ 0 & T_{\mathbf{q}_1} \chi_{\sigma(V_0^a) \cap \sigma(V_0^s)} & \dots & 0 \\ \vdots & \vdots & \ddots & \vdots \\ 0 & 0 & \dots & T_{\mathbf{q}_{n-1}} \chi_{\sigma(V_0^a) \cap \sigma(V_0^s)} \end{pmatrix} \quad (3.9)$$

holds almost everywhere on \mathbb{T}^d then Ψ^a and Ψ^s is a pair of dual frames for $L^2(\mathbb{R}^d)$. This special case of Theorem 3.1.4 is referred to as the *Mixed Extension Principle* in [38]. Notice that in this case, the Mixed Fundamental function $\Theta_M = 1$ a.e. on $\sigma(V_0^a) \cap \sigma(V_0^s)$. The more general case where Θ_M may take values other than one is referred to as the *Mixed Oblique Extension Principle* in [38].

The purpose of the next theorem is to characterize when the set $X_{\phi\psi}$ is a Parseval frame for $L^2(\mathbb{R}^d)$ under the most general hypotheses on the refinable function ϕ and on the filters H_i . Before we state and prove the theorem, let us prove the following lemma required in the proof of the theorem and also for the examples described in Section 3.2.

Lemma 3.1.6 *Let G be a finite group with the group operation denoted by \circ and let χ be a character on G . If χ is not the identity character on G , i.e. there exists an h in G such that $\chi(h) \neq 1$, then $\sum_{g \in G} \chi(g) = 0$.*

Proof: Let h in G satisfying $\chi(h) \neq 1$. Set $Y := \sum_{g \in G} \chi(g)$ and observe

$$\chi(h) \sum_{g \in G} \chi(g) = \sum_{g \in G} \chi(h \circ g) = Y.$$

Hence, we have $Y(\chi(h) - 1) = 0$, which gives us the required result since $\chi(h) \neq 1$. \square

Theorem 3.1.7 *Let $\phi \in L^2(\mathbb{R}^d)$ be a refinable function such that $\hat{\phi}$ is continuous at the origin satisfying Equations (3.1) and (3.2). Moreover assume $H_i \in L^\infty(\mathbb{T}^d)$ for all $i = 1, \dots, m$ are \mathbb{Z}^d -periodic functions and $\psi_i \in L^2(\mathbb{R}^d)$ are given by Equation (3.3).*

Then $X_{\phi\psi}$ is a Parseval frame for $L^2(\mathbb{R}^d)$ if and only if for all $\mathbf{q} \in (A^{-1}\mathbb{Z}^d)/\mathbb{Z}^d$ and for a.e. $\boldsymbol{\xi}, \boldsymbol{\xi} + \mathbf{q} \in \sigma(V_0)$,*

$$\sum_{i=0}^m H_i(\boldsymbol{\xi}) \overline{H_i(\boldsymbol{\xi} + \mathbf{q})} = \delta_{\mathbf{q},0}. \quad (3.10)$$

Proof: The proof splits in two parts. In the first part, we establish that $X_{\phi\psi}$ is a Parseval frame if and only if the following condition holds,

$$\sum_{j=0}^{j_0(\mathbf{l})} \sum_{i=1}^m \widehat{\psi}_i(A^{*-j}\boldsymbol{\xi}) \overline{\widehat{\psi}_i(A^{*-j}(\boldsymbol{\xi} + \mathbf{l}))} + \widehat{\phi}(\boldsymbol{\xi}) \overline{\widehat{\phi}(\boldsymbol{\xi} + \mathbf{l})} = \delta_{\mathbf{l},0},$$

for a.e. $\boldsymbol{\xi} \in \mathbb{R}^d$ and $\mathbf{l} \in \mathbb{Z}^d$ (The function j_0 is defined in (3.12) below). In the second part, we show that this condition is equivalent to (3.10). First, assume that $X_{\phi\psi}$ is a Parseval frame for $L^2(\mathbb{R}^d)$ and obtain the above condition.

We begin by defining a unitary operator $U : L^2(\mathbb{R}^d) \rightarrow L^2(\mathbb{T}^d, l^2(\mathbb{Z}^d))$ via

$$U(f) = \left\{ \widehat{f}(\cdot + \mathbf{k}) : \mathbf{k} \in \mathbb{Z}^d \right\}.$$

Next we define the set J by

$$J := \left\{ (j, r, i) : j \in \mathbb{N} \cup \{0\}, r \in \mathbb{Z}^d / (A^{*j}\mathbb{Z}^d), i = 1, \dots, m \right\} \cup \{(0, 0, 0)\},$$

and a map $S : L^2(\mathbb{T}^d, l^2(J)) \rightarrow L^2(\mathbb{T}^d, l^2(\mathbb{Z}^d))$, via

$$S(e_{\mathbf{l}}, \delta_{(j,r,i)}) = U(T_{\mathbf{l}} D_A^j T_r \psi_i) \quad \text{for all } \mathbf{l} \in \mathbb{Z}^d, (j, r, i) \in J,$$

where we adopt the convention $\psi_0 = \phi$. Note that,

$$(S e_{\mathbf{l}} \delta_{(j,r,i)})(\boldsymbol{\xi}) = \left\{ e_{\mathbf{l}}(\boldsymbol{\xi}) |\det(A)|^{-j/2} e^{-2\pi i \langle r, A^{*-j}(\boldsymbol{\xi} + \mathbf{k}) \rangle} \widehat{\psi}_i(A^{*-j}(\boldsymbol{\xi} + \mathbf{k})) \right\}_{\mathbf{k} \in \mathbb{Z}^d} \text{ for a.e. } \boldsymbol{\xi} \in \mathbb{T}^d.$$

Since $X_{\phi\psi}$ is a Parseval frame, S can be extended to a bounded linear transformation on $L^2(\mathbb{T}^d, l^2(J))$. Now S can be represented by a $\mathbb{Z}^d \times J$ matrix so that the $(\mathbf{k}, (j, r, i))$ -th entry of the matrix is an operator on $L^2(\mathbb{T}^d)$, denoted by $S_{\mathbf{k},(j,r,i)}$. This operator acts on the modulations as follows:

$$(S_{\mathbf{k},(j,r,i)} e_{\mathbf{l}})(\boldsymbol{\xi}) = e_{\mathbf{l}}(\boldsymbol{\xi}) |\det(A)|^{-j/2} e^{-2\pi i \langle r, (A^{*-j}(\boldsymbol{\xi} + \mathbf{k})) \rangle} \widehat{\psi}_i(A^{*-j}(\boldsymbol{\xi} + \mathbf{k})).$$

Thus we see that each $S_{\mathbf{k},(j,r,i)}$ commutes with all the modulation operators $M_{\mathbf{l}}$ defined on $L^2(\mathbb{T}^d)$ by $M_{\mathbf{l}}\omega(\boldsymbol{\xi}) := e_{\mathbf{l}}(\boldsymbol{\xi})\omega(\boldsymbol{\xi})$. Hence, each $S_{\mathbf{k},(j,r,i)}$ is a multiplicative operator (e.g. [37, Corollary 2.12.7]) in the following sense:

$$(S_{\mathbf{k},(j,r,i)}\omega)(\boldsymbol{\xi}) = \omega(\boldsymbol{\xi}) |\det(A)|^{-j/2} e^{-2\pi i \langle r, (A^{*-j}(\boldsymbol{\xi} + \mathbf{k})) \rangle} \widehat{\psi}_i(A^{*-j}(\boldsymbol{\xi} + \mathbf{k})),$$

for all $\omega \in L^2(\mathbb{T}^d)$. We denote the symbol for this operator again by $S_{\mathbf{k},(j,r,i)}(\cdot)$, so that

$$S_{\mathbf{k},(j,r,i)}(\boldsymbol{\xi}) = |\det(A)|^{-j/2} e^{-2\pi i \langle r, (A^{*-j}(\boldsymbol{\xi} + \mathbf{k})) \rangle} \widehat{\psi}_i(A^{*-j}(\boldsymbol{\xi} + \mathbf{k})).$$

Note that $S_{\mathbf{k},(j,r,i)}(\cdot)$ is an essentially bounded \mathbb{Z}^d -periodic function. Let $S(\cdot)$ denote the $\mathbb{Z}^d \times J$ matrix of the symbols $S_{\mathbf{k},(j,r,i)}(\cdot)$, then

$$(S\omega)(\boldsymbol{\xi}) = S(\boldsymbol{\xi})\omega(\boldsymbol{\xi}) \quad \text{for all } \omega \in L^2(\mathbb{T}^d, l^2(J)).$$

Also $\|S(\cdot)\|$ is essentially bounded [37, Theorem 7.52.8] Now, the adjoint of S can be represented by the $J \times \mathbb{Z}^d$ matrix of operators on $L^2(\mathbb{T}^d)$ such that the $((j, r, i), \mathbf{k})$ -th entry is $S_{\mathbf{k},(j,r,i)}^*$. Since $S_{\mathbf{k},(j,r,i)}^*$ is the adjoint of a multiplicative operator, it is itself a multiplicative operator with symbol $\overline{S_{\mathbf{k},(j,r,i)}(\cdot)}$. Therefore,

$$(S^*\omega)(\boldsymbol{\xi}) = S(\boldsymbol{\xi})^*\omega(\boldsymbol{\xi}) \quad \text{for all } \omega \in L^2(\mathbb{T}^d, l^2(\mathbb{Z}^d)).$$

Since $X_{\phi\psi}$ is a Parseval frame, we have, $SS^* = I_{L^2(\mathbb{T}^d, l^2(\mathbb{Z}^d))}$, i.e.

$$S(\boldsymbol{\xi})S(\boldsymbol{\xi})^* = I_{l^2(\mathbb{Z}^d)} \quad \text{for a.e. } \boldsymbol{\xi} \in \mathbb{T}^d. \quad (3.11)$$

The (\mathbf{k}, \mathbf{l}) -th entry of $S(\boldsymbol{\xi})S(\boldsymbol{\xi})^*$ is given by

$$\begin{aligned} & (S(\boldsymbol{\xi})S(\boldsymbol{\xi})^*)_{(\mathbf{k}, \mathbf{l})} \\ &= \sum_{j=0}^{\infty} \sum_{i=1}^m |\det(A)|^{-j} \sum_{r \in \mathbb{Z}^d / (A^{*j}\mathbb{Z}^d)} e^{2\pi i \langle r, A^{*-j}(\mathbf{k} - \mathbf{l}) \rangle} \widehat{\psi}_i(A^{*-j}(\boldsymbol{\xi} + \mathbf{k})) \overline{\widehat{\psi}_i(A^{*-j}(\boldsymbol{\xi} + \mathbf{l}))} \\ &+ \widehat{\phi}(\boldsymbol{\xi} + \mathbf{k}) \overline{\widehat{\phi}(\boldsymbol{\xi} + \mathbf{l})}. \end{aligned}$$

Now, define $j_0 : \mathbb{Z}^d \setminus \{0\} \rightarrow \mathbb{Z}$ via

$$j_0(\mathbf{l}) = \sup\{j : A^{*-j}(\mathbf{l}) \in \mathbb{Z}^d\}. \quad (3.12)$$

Obviously, if $\mathbf{l} \neq 0$, then $j_0(\mathbf{l})$ is finite while $j_0(0)$ can be set equal to $+\infty$. If $j > j_0(\mathbf{k} - \mathbf{l})$ then $A^{*-j}(\mathbf{k} - \mathbf{l}) \notin \mathbb{Z}^d$ and therefore $e_{A^{*-j}(\mathbf{k} - \mathbf{l})}$ is not the identity character on $\mathbb{Z}^d / (A^{*j}\mathbb{Z}^d)$.

On the other hand, if $j \leq j_0(\mathbf{k} - \mathbf{l})$ then $A^{*-j}(\mathbf{k} - \mathbf{l}) \in \mathbb{Z}^d$ and $e_{A^{*-j}(\mathbf{k}-\mathbf{l})}$ is the identity character on $\mathbb{Z}^d/(A^{*j}\mathbb{Z}^d)$. Thus using Lemma 3.1.6, we conclude

$$|\det(A)|^{-j} \sum_{r \in \mathbb{Z}^d/(A^{*j}\mathbb{Z}^d)} e^{2\pi i \langle r, A^{*-j}(\mathbf{k}-\mathbf{l}) \rangle} = \begin{cases} 0 & \text{for } j > j_0(\mathbf{k} - \mathbf{l}) \\ 1 & \text{for } j \leq j_0(\mathbf{k} - \mathbf{l}) \end{cases}.$$

Hence, for $\mathbf{k} \neq \mathbf{l}$, (3.12) reduces to,

$$(S(\boldsymbol{\xi})S(\boldsymbol{\xi})^*)_{(\mathbf{k}, \mathbf{l})} = \sum_{j=0}^{j_0(\mathbf{k}-\mathbf{l})} \sum_{i=1}^m \widehat{\psi}_i(A^{*-j}(\boldsymbol{\xi} + \mathbf{k})) \overline{\widehat{\psi}_i(A^{*-j}(\boldsymbol{\xi} + \mathbf{l}))} + \widehat{\phi}(\boldsymbol{\xi} + \mathbf{k}) \overline{\widehat{\phi}(\boldsymbol{\xi} + \mathbf{l})}.$$

Thus using (3.11), we conclude that the following condition holds for a.e. $\boldsymbol{\xi} \in \mathbb{T}^d$ and $\mathbf{k}, \mathbf{l} \in \mathbb{Z}^d$:

$$\sum_{j=0}^{j_0(\mathbf{k}-\mathbf{l})} \sum_{i=1}^m \widehat{\psi}_i(A^{*-j}(\boldsymbol{\xi} + \mathbf{k})) \overline{\widehat{\psi}_i(A^{*-j}(\boldsymbol{\xi} + \mathbf{l}))} + \widehat{\phi}(\boldsymbol{\xi} + \mathbf{k}) \overline{\widehat{\phi}(\boldsymbol{\xi} + \mathbf{l})} = \delta_{\mathbf{k}, \mathbf{l}}. \quad (3.13)$$

By changing variables the previous equation becomes equivalent to:

$$\sum_{j=0}^{j_0(\mathbf{l})} \sum_{i=1}^m \widehat{\psi}_i(A^{*-j}\boldsymbol{\xi}) \overline{\widehat{\psi}_i(A^{*-j}(\boldsymbol{\xi} + \mathbf{l}))} + \widehat{\phi}(\boldsymbol{\xi}) \overline{\widehat{\phi}(\boldsymbol{\xi} + \mathbf{l})} = \delta_{0, \mathbf{l}}. \quad (3.14)$$

for a.e. $\boldsymbol{\xi} \in \mathbb{R}^d$ and $\mathbf{l} \in \mathbb{Z}^d$.

Conversely, we must show that if (3.14) holds for a.e. $\boldsymbol{\xi} \in \mathbb{R}^d$ and $\mathbf{l} \in \mathbb{Z}^d$, then $X_{\phi\psi}$ is a Parseval frame. To this end, we densely define the operators $\mathcal{A}(\boldsymbol{\xi}) : l^2(\mathbb{Z}^d) \rightarrow l^2(J)$ via

$$\mathcal{A}(\boldsymbol{\xi})\delta_{\mathbf{k}} = \left\{ |\det(A)|^{-j/2} e^{2\pi i \langle r, A^{*-j}(\boldsymbol{\xi} + \mathbf{k}) \rangle} \overline{\widehat{\psi}_i(A^{*-j}(\boldsymbol{\xi} + \mathbf{k}))} \right\}_{(j, r, i) \in J}.$$

Using (3.13) which is equivalent to (3.14), we conclude that $\mathcal{A}(\boldsymbol{\xi})$ extends to an isometry on $l^2(\mathbb{Z}^d)$, for a.e. $\boldsymbol{\xi} \in \mathbb{T}^d$. We now define the operator $\mathcal{A} : L^2(\mathbb{T}^d, l^2(\mathbb{Z}^d)) \rightarrow L^2(\mathbb{T}^d, l^2(J))$, via

$$(\mathcal{A}\omega)(\boldsymbol{\xi}) = \mathcal{A}(\boldsymbol{\xi})\omega(\boldsymbol{\xi}).$$

Since $\mathcal{A}(\boldsymbol{\xi})$ is an isometry for a.e. $\boldsymbol{\xi} \in \mathbb{T}^d$, it is easy to verify that \mathcal{A} is an isometry. But \mathcal{A} coincides with S^* , which is the analysis operator for the family $X_{\phi\psi}$. Therefore $X_{\phi\psi}$ is a Parseval frame, finishing the first part of the proof.

Now, we proceed to the second part of the proof. In this part we show that (3.14) holds if and only if (3.10) holds. We will first assume (3.10) holds and prove that (3.14) holds for all $\mathbf{l} \neq 0$. Note, that $A^{*-j}\mathbf{l} \in \mathbb{Z}^d$ for all $j = 0, 1, \dots, j_0(\mathbf{l})$. Thus, for all these j we have $\sum_{i=0}^m H_i(A^{*-(j_0(\mathbf{l})+1)}\boldsymbol{\xi}) \overline{H_i(A^{*-(j_0(\mathbf{l})+1)}(\boldsymbol{\xi} + \mathbf{l}))} = 1$ due to (3.10). Using the last equation and the two-scale relations ((3.2) and (3.3)) we obtain,

$$\begin{aligned}
 & \sum_{j=0}^{j_0(\mathbf{l})} \sum_{i=1}^m \widehat{\psi}_i(A^{*-j}\boldsymbol{\xi}) \overline{\widehat{\psi}_i(A^{*-j}(\boldsymbol{\xi} + \mathbf{l}))} + \widehat{\phi}(\boldsymbol{\xi}) \overline{\widehat{\phi}(\boldsymbol{\xi} + \mathbf{l})} \\
 = & \sum_{j=1}^{j_0(\mathbf{l})} \sum_{i=1}^m \widehat{\psi}_i(A^{*-j}\boldsymbol{\xi}) \overline{\widehat{\psi}_i(A^{*-j}(\boldsymbol{\xi} + \mathbf{l}))} + \\
 & + \widehat{\phi}(A^{*-1}\boldsymbol{\xi}) \overline{\widehat{\phi}(A^{*-1}(\boldsymbol{\xi} + \mathbf{l}))} \left(\sum_{i=0}^m H_i(A^{*-1}\boldsymbol{\xi}) \overline{H_i(A^{*-1}(\boldsymbol{\xi} + \mathbf{l}))} \right) \\
 = & \sum_{j=1}^{j_0(\mathbf{l})} \sum_{i=1}^m \widehat{\psi}_i(A^{*-j}\boldsymbol{\xi}) \overline{\widehat{\psi}_i(A^{*-j}(\boldsymbol{\xi} + \mathbf{l}))} + \widehat{\phi}(A^{*-1}\boldsymbol{\xi}) \overline{\widehat{\phi}(A^{*-1}(\boldsymbol{\xi} + \mathbf{l}))} \\
 & \vdots \\
 = & \sum_{i=1}^m \widehat{\psi}_i(A^{*-j_0(\mathbf{l})}\boldsymbol{\xi}) \overline{\widehat{\psi}_i(A^{*-j_0(\mathbf{l})}(\boldsymbol{\xi} + \mathbf{l}))} \\
 & + \widehat{\phi}(A^{*-j_0(\mathbf{l})}\boldsymbol{\xi}) \overline{\widehat{\phi}(A^{*-j_0(\mathbf{l})}(\boldsymbol{\xi} + \mathbf{l}))} \left(\sum_{i=0}^m H_i(A^{*-j_0(\mathbf{l})}\boldsymbol{\xi}) \overline{H_i(A^{*-j_0(\mathbf{l})}(\boldsymbol{\xi} + \mathbf{l}))} \right) \\
 = & \sum_{i=1}^m \widehat{\psi}_i(A^{*-j_0(\mathbf{l})}\boldsymbol{\xi}) \overline{\widehat{\psi}_i(A^{*-j_0(\mathbf{l})}(\boldsymbol{\xi} + \mathbf{l}))} + \widehat{\phi}(A^{*-j_0(\mathbf{l})}\boldsymbol{\xi}) \overline{\widehat{\phi}(A^{*-j_0(\mathbf{l})}(\boldsymbol{\xi} + \mathbf{l}))} \\
 = & \widehat{\phi}(A^{*-(j_0(\mathbf{l})+1)}\boldsymbol{\xi}) \overline{\widehat{\phi}(A^{*-(j_0(\mathbf{l})+1)}(\boldsymbol{\xi} + \mathbf{l}))}. \\
 & \left(\sum_{i=0}^m H_i(A^{*-(j_0(\mathbf{l})+1)}\boldsymbol{\xi}) \overline{H_i(A^{*-(j_0(\mathbf{l})+1)}(\boldsymbol{\xi} + \mathbf{l}))} \right) \\
 = & 0.
 \end{aligned}$$

Next we show that (3.14) holds for $\mathbf{l} = 0$, using the hypothesis (3.10). For a fixed N we have

$$\begin{aligned}
 & \sum_{j=0}^N \sum_{i=1}^m \left| \widehat{\psi}_i(A^{*-j}\boldsymbol{\xi}) \right|^2 + \left| \widehat{\phi}(\boldsymbol{\xi}) \right|^2 \\
 = & \sum_{j=1}^N \sum_{i=1}^m \left| \widehat{\psi}_i(A^{*-j}\boldsymbol{\xi}) \right|^2 + \left| \widehat{\phi}(A^{*-1}\boldsymbol{\xi}) \right|^2 \left(\sum_{i=0}^m |H_i(A^{*-1}\boldsymbol{\xi})|^2 \right) \\
 = & \sum_{j=1}^N \sum_{i=1}^m \left| \widehat{\psi}_i(A^{*-j}\boldsymbol{\xi}) \right|^2 + \left| \widehat{\phi}(A^{*-1}\boldsymbol{\xi}) \right|^2 \\
 = & \sum_{j=2}^N \sum_{i=1}^m \left| \widehat{\psi}_i(A^{*-j}\boldsymbol{\xi}) \right|^2 + \left| \widehat{\phi}(A^{*-2}\boldsymbol{\xi}) \right|^2 \left(\sum_{i=0}^m |H_i(A^{*-2}\boldsymbol{\xi})|^2 \right) \\
 = & \sum_{j=2}^N \sum_{i=1}^m \left| \widehat{\psi}_i(A^{*-j}\boldsymbol{\xi}) \right|^2 + \left| \widehat{\phi}(A^{*-2}\boldsymbol{\xi}) \right|^2 \\
 & \vdots \\
 = & \sum_{i=1}^m \left| \widehat{\psi}_i(A^{*-N}\boldsymbol{\xi}) \right|^2 + \left| \widehat{\phi}(A^{*-N}\boldsymbol{\xi}) \right|^2 \left(\sum_{i=0}^m |H_i(A^{*-N}\boldsymbol{\xi})|^2 \right) \\
 = & \sum_{i=1}^m \left| \widehat{\psi}_i(A^{*-N}\boldsymbol{\xi}) \right|^2 + \left| \widehat{\phi}(A^{*-N}\boldsymbol{\xi}) \right|^2 \\
 = & \left| \widehat{\phi}(A^{*-N-1}\boldsymbol{\xi}) \right|^2 \left(\sum_{i=0}^m |H_i(A^{*-N-1}\boldsymbol{\xi})|^2 \right) = \left| \widehat{\phi}(A^{*-N-1}\boldsymbol{\xi}) \right|^2.
 \end{aligned}$$

Now the assumption (3.1), together with the continuity of $\widehat{\phi}$ at 0 imply that for every $\epsilon > 0$, there exists a N_0 such that $\left| \left| \widehat{\phi}(A^{*-N}\boldsymbol{\xi}) \right|^2 - 1 \right| < \epsilon$ for all $N > N_0$. This in turn implies that

$$\left| \sum_{j=0}^N \sum_{i=1}^m \left| \widehat{\psi}_i(A^{*-j}\boldsymbol{\xi}) \right|^2 + \left| \widehat{\phi}(\boldsymbol{\xi}) \right|^2 - 1 \right| < \epsilon,$$

for all $N > N_0 + 1$. This proves that (3.14) holds for $\mathbf{l} = 0$. Thus, we have shown that (3.10) implies (3.14).

To establish the converse implication, first notice that the calculations we carried out to prove that (3.10) implies (3.14) for $\mathbf{l} \neq 0$ are still valid for almost every $\boldsymbol{\xi}$ and all $\mathbf{l} \in \mathbb{Z}^d$.

Now pick $\mathbf{q} \in (A^{*-1})\mathbb{Z}^d/\mathbb{Z}^d$. We have $A^*\mathbf{q} \in \mathbb{Z}^d$. If \mathbf{p} is an arbitrary integer grid point, i.e. $\mathbf{p} \in \mathbb{Z}^d$ set $\mathbf{l} := A^*(\mathbf{q} + \mathbf{p})$. Obviously $\mathbf{l} \in \mathbb{Z}^d$, since A is expansive and thus A^* leaves the lattice \mathbb{Z}^d invariant. Observe $j_0(\mathbf{l}) = 0$, because $\mathbf{p} + \mathbf{q}$ does not belong to the integer grid. Next, assume that (3.10) holds for $\mathbf{q} = 0$. Since, (3.14) is valid for all $\mathbf{l} \neq 0$ we deduce

$$\begin{aligned} 0 &= \sum_{i=1}^m \widehat{\psi}_i(\boldsymbol{\xi}) \overline{\widehat{\psi}_i(\boldsymbol{\xi} + \mathbf{l})} + \widehat{\phi}(\boldsymbol{\xi}) \overline{\widehat{\phi}(\boldsymbol{\xi} + \mathbf{l})} \\ &= \widehat{\phi}(A^{*-1}\boldsymbol{\xi}) \overline{\widehat{\phi}(A^{*-1}(\boldsymbol{\xi} + \mathbf{l}))} \left(\sum_{i=0}^m H_i(A^{*-1}\boldsymbol{\xi}) \overline{H_i(A^{*-1}(\boldsymbol{\xi} + \mathbf{l}))} \right) \\ &= \widehat{\phi}(A^{*-1}\boldsymbol{\xi}) \overline{\widehat{\phi}(A^{*-1}\boldsymbol{\xi} + \mathbf{q} + \mathbf{p})} \left(\sum_{i=0}^m H_i(A^{*-1}\boldsymbol{\xi}) \overline{H_i(A^{*-1}\boldsymbol{\xi} + \mathbf{q} + \mathbf{p})} \right) \quad \text{a.e. in } \mathbb{R}^d. \end{aligned}$$

Take $\boldsymbol{\xi}$ and $\boldsymbol{\xi} + \mathbf{q}$ in $\sigma(V_0)$ such that $A^*\boldsymbol{\xi}$ belongs to the set of points in \mathbb{R}^d for which (3.14) holds. The fact that (3.14) is equivalent to (3.13) implies that, if (3.14) holds for a $\boldsymbol{\xi} \in \mathbb{R}^d$ then, (3.14) holds for all integer translates of this point. Apply the previous equations for $A^*(\boldsymbol{\xi} + \mathbf{s})$ instead of $\boldsymbol{\xi}$, where $\mathbf{s} \in \mathbb{Z}^d$. Then

$$0 = \widehat{\phi}(\boldsymbol{\xi} + \mathbf{s}) \overline{\widehat{\phi}(\boldsymbol{\xi} + \mathbf{q} + \mathbf{p})} \left(\sum_{i=0}^m H_i(\boldsymbol{\xi}) \overline{H_i(\boldsymbol{\xi} + \mathbf{q})} \right),$$

due to the \mathbb{Z}^d -periodicity of H_i . Since \mathbf{p}, \mathbf{s} are arbitrary integers and $\boldsymbol{\xi}, \boldsymbol{\xi} + \mathbf{q} \in \sigma(V_0)$ there exist some \mathbf{s}_0 and \mathbf{p}_0 for which

$$\widehat{\phi}(\boldsymbol{\xi} + \mathbf{s}_0) \overline{\widehat{\phi}(\boldsymbol{\xi} + \mathbf{q} + \mathbf{p}_0)} \neq 0.$$

Thus,

$$\sum_{i=0}^m H_i(\boldsymbol{\xi}) \overline{H_i(\boldsymbol{\xi} + \mathbf{q})} = 0.$$

In order to complete the proof of the theorem we need to establish that (3.10) holds for $\mathbf{q} = 0$. To verify this, set $\mathbf{l} = 0$ in (3.14):

$$\sum_{j=0}^{\infty} \sum_{i=1}^m \left| \widehat{\psi}_i(A^{*-j}\boldsymbol{\xi}) \right|^2 + \left| \widehat{\phi}(\boldsymbol{\xi}) \right|^2 = 1, \quad \boldsymbol{\xi} \in \mathbb{R}^d \text{ a.e. .}$$

Observe that this implies

$$\sum_{j=0}^{\infty} \sum_{i=1}^m \left| \widehat{\psi}_i(A^{*-j+1}\boldsymbol{\xi}) \right|^2 + \left| \widehat{\phi}(A^*\boldsymbol{\xi}) \right|^2 = 1, \quad \boldsymbol{\xi} \in \mathbb{R}^d \text{ a.e. .}$$

Using the two scale relations, (3.2) and (3.3), we infer

$$\sum_{j=0}^{\infty} \sum_{i=1}^m \left| \widehat{\psi}_i(A^{*-j+1}\boldsymbol{\xi}) \right|^2 + \left| \widehat{\phi}(A^*\boldsymbol{\xi}) \right|^2 = \sum_{j=0}^{\infty} \sum_{i=1}^m \left| \widehat{\psi}_i(A^{*-j}\boldsymbol{\xi}) \right|^2 + \left| \widehat{\phi}(\boldsymbol{\xi}) \right|^2 \left(\sum_{i=0}^m |H_i(\boldsymbol{\xi})|^2 \right).$$

Hence,

$$\sum_{j=0}^{\infty} \sum_{i=1}^m \left| \widehat{\psi}_i(A^{*-j}\boldsymbol{\xi}) \right|^2 + \left| \widehat{\phi}(\boldsymbol{\xi}) \right|^2 = \sum_{j=0}^{\infty} \sum_{i=1}^m \left| \widehat{\psi}_i(A^{*-j}\boldsymbol{\xi}) \right|^2 + \left| \widehat{\phi}(\boldsymbol{\xi}) \right|^2 \left(\sum_{i=0}^m |H_i(\boldsymbol{\xi})|^2 \right).$$

Therefore, $\sum_{i=0}^m |H_i(\boldsymbol{\xi})|^2 = 1$ for a.e. $\boldsymbol{\xi} \in \sigma(V_0)$. \square

Remark 3.1.8 The characterization of affine frames in [97] utilizes

$$\Psi[\omega, \omega'] := \sum_{\psi \in \Psi} \sum_{j=\kappa(\omega-\omega')}^{\infty} \widehat{\psi}(2^j\omega) \overline{\widehat{\psi}(2^j\omega')}, \quad \omega, \omega' \in \mathbb{R}$$

where κ is defined by $\kappa(\omega) = \inf\{j \in \mathbb{Z} : 2^j\omega \in 2\pi\mathbb{Z}\}$. A similar convention is used by Bownik [17]. This is reminiscent of the term of the sum in the left-hand side of (3.14) involving the wavelets ψ_i . However, since we use positive powers of D_A in the definition of $X_{\phi\psi}$, we arrive at negative powers of A^* .

An immediate consequence of the previous theorem is a generalization of the UEP.

Corollary 3.1.9 [13] *Under the hypotheses of Theorem 3.1.7 the following is true: If Condition 3.10 holds for all $\mathbf{q} \in (A^{*-1}\mathbb{Z}^d)/\mathbb{Z}^d$ and for a.e. $\boldsymbol{\xi}, \boldsymbol{\xi} + \mathbf{q} \in \sigma(V_0)$, then the set $\left\{ D_A^j T_{\mathbf{k}} \psi_i : j \in \mathbb{Z}, \mathbf{k} \in \mathbb{Z}^d, i = 1, \dots, m \right\}$ is a Parseval frame for $L^2(\mathbb{R}^d)$.*

Proof: Obviously we have that $X_{\phi\psi}$ is a Parseval frame of $L^2(\mathbb{R}^d)$, thus for every $j_0 \in \mathbb{Z}$, the set

$$\left\{ D_A^j T_{\mathbf{k}} \psi_i : j \geq j_0, \mathbf{k} \in \mathbb{Z}^d, i = 1, \dots, m \right\} \cup \left\{ D_A^{j_0} T_{\mathbf{k}} \phi : \mathbf{k} \in \mathbb{Z}^d \right\},$$

is a Parseval frame of $L^2(\mathbb{R}^d)$ as well. Now, take $f \in L^2(\mathbb{R}^d)$. Then as $j_0 \rightarrow -\infty$ observe that

$$\lim_{j_0 \rightarrow -\infty} \sum_{\mathbf{k} \in \mathbb{Z}^d} \left| \langle f, D_A^{j_0} T_{\mathbf{k}} \phi \rangle \right|^2 = 0.$$

The proof of this fact is not hard (see [13, Lemma 7.7]), so we omit it. \square

Theorem 3.1.7 shows that $X_{\phi\psi}$ is a Parseval frame if and only if the conditions in Theorem 3.1.1 hold with the fundamental function equal to 1 a.e. on $\sigma(V_0)$. In the same spirit, the next theorem characterizes the Bessel families, $X_{\phi\psi}^a$ and $X_{\phi\psi}^s$, that form a pair of dual frames based on conditions on the corresponding filters. We infer that $X_{\phi\psi}^a$ and $X_{\phi\psi}^s$ are a pair of dual frames for $L^2(\mathbb{R}^d)$ if and only if the conditions in Theorem 3.1.4 hold with the mixed fundamental function equal to 1 a.e. on $\sigma(V_0^a) \cap \sigma(V_0^s)$ (see Remark 3.1.11 below). The proof of Theorem 3.1.10 uses arguments similar to those in the proof of Theorem 3.1.7.

Theorem 3.1.10 *Let ϕ^a and ϕ^s be refinable functions in $L^2(\mathbb{R}^d)$ such that $\widehat{\phi}^a$ and $\widehat{\phi}^s$ are continuous at the origin and*

$$\lim_{|\boldsymbol{\xi}| \rightarrow 0} \widehat{\phi}^a(\boldsymbol{\xi}) = \widehat{\phi}^s(\boldsymbol{\xi}) = 1. \quad (3.15)$$

Let H_0^a and $H_0^s \in L^\infty(\mathbb{T}^d)$, be the associated low pass filters. Furthermore, let $H_i^a, H_i^s \in L^\infty(\mathbb{T}^d)$ for $i = 1, \dots, m$, be \mathbb{Z}^d -periodic functions and define m pairs of wavelets ψ_i^a, ψ_i^s $i = 1, \dots, m$, by

$$\widehat{\psi}_i^a(A^* \cdot) = H_i^a \widehat{\phi}^a. \quad (3.16)$$

$$\widehat{\psi}_i^s(A^* \cdot) = H_i^s \widehat{\phi}^s. \quad (3.17)$$

3.1. EXTENSION PRINCIPLES REVISITED

Then $X_{\phi\psi}^a$ and $X_{\phi\psi}^s$ form a pair of dual frames for $L^2(\mathbb{R}^d)$ if and only if

1. $X_{\phi\psi}^a$ and $X_{\phi\psi}^s$ are Bessel families,
2. For all $\mathbf{q} \in (A^{*-1}\mathbb{Z}^d)/\mathbb{Z}^d$ and for a.e. $\boldsymbol{\xi}, \boldsymbol{\xi} + \mathbf{q} \in \sigma(V_0^a) \cap \sigma(V_0^s)$,

$$\sum_{i=0}^m H_i^s(\boldsymbol{\xi}) \overline{H_i^a(\boldsymbol{\xi} + \mathbf{q})} = \delta_{\mathbf{q},0}. \quad (3.18)$$

Proof: Analogous to the proof of Theorem 3.1.7, the proof for this theorem is divided into two parts. First, we establish that $X_{\phi\psi}^a$ and $X_{\phi\psi}^s$ is a pair of dual frames for $L^2(\mathbb{R}^d)$, if and only if the following condition holds,

$$\sum_{j=0}^{j_0(\mathbf{l})} \sum_{i=1}^n \widehat{\psi}_i^s(A^{*-j}\boldsymbol{\xi}) \overline{\widehat{\psi}_i^a(A^{*-j}(\boldsymbol{\xi} + \mathbf{l}))} + \widehat{\phi}^s(\boldsymbol{\xi}) \overline{\widehat{\phi}^a(\boldsymbol{\xi} + \mathbf{l})} = \delta_{\mathbf{l},0}.$$

for a.e. $\boldsymbol{\xi} \in \mathbb{R}^d$ and $\mathbf{l} \in \mathbb{Z}^d$ (The function j_0 is defined in (3.21) below). In the second part we show that this condition is equivalent to (3.18).

We begin by defining a unitary operator $U : L^2(\mathbb{R}^d) \rightarrow L^2(\mathbb{T}^d, l^2(\mathbb{Z}^d))$ via

$$U(f) = \left\{ \widehat{f}(\cdot + \mathbf{k}) : \mathbf{k} \in \mathbb{Z}^d \right\}.$$

Next we define the set J by

$$J := \left\{ (j, \mathbf{r}, i) : j \in \mathbb{N} \cup \{0\}, \mathbf{r} \in \mathbb{Z}^d / (A^{*j}\mathbb{Z}^d), i = 1, \dots, n \right\} \cup \{(0, 0, 0)\},$$

and a map $S^a : L^2(\mathbb{T}^d, l^2(J)) \rightarrow L^2(\mathbb{T}^d, l^2(\mathbb{Z}^d))$, via

$$S^a(e_{\mathbf{l}}, \delta_{(j,\mathbf{r},i)}) = U(T_{\mathbf{l}} D_A^j T_{\mathbf{r}} \psi_i^a) \quad \text{for all } \mathbf{l} \in \mathbb{Z}^d, (j, \mathbf{r}, i) \in J,$$

where we adopt the convention $\psi_0^a = \phi^a$.

Note that,

$$(S^a e_{\mathbf{l}} \delta_{(j,\mathbf{r},i)})(\boldsymbol{\xi}) = \left\{ e_{\mathbf{l}}(\boldsymbol{\xi}) |\det(A)|^{-j/2} e^{-2\pi i \langle \mathbf{r}, A^{*-j}(\boldsymbol{\xi} + \mathbf{k}) \rangle} \widehat{\psi}_i^a(A^{*-j}(\boldsymbol{\xi} + \mathbf{k})) \right\}_{\mathbf{k} \in \mathbb{Z}^d},$$

3.1. EXTENSION PRINCIPLES REVISITED

for a.e. $\boldsymbol{\xi} \in \mathbb{T}^d$. Since $X_{\phi\psi}^a$ is a Bessel family, S^a can be extended to a bounded linear transformation on $L^2(\mathbb{T}^d, l^2(J))$. Now S^a can be represented by a $\mathbb{Z}^d \times J$ matrix so that the $(\mathbf{k}, (j, \mathbf{r}, i))$ -th entry of the matrix is an operator on $L^2(\mathbb{T}^d)$, denoted by $S_{\mathbf{k},(j,\mathbf{r},i)}^a$. This operator acts on the modulations as follows,

$$(S_{\mathbf{k},(j,\mathbf{r},i)}^a e_{\mathbf{l}})(\boldsymbol{\xi}) = e_{\mathbf{l}}(\boldsymbol{\xi}) |\det(A)|^{-j/2} e^{-2\pi i \langle \mathbf{r}, (A^{*-j}(\boldsymbol{\xi} + \mathbf{k})) \rangle} \widehat{\psi}_i^a(A^{*-j}(\boldsymbol{\xi} + \mathbf{k})).$$

Thus, we see that each $S_{\mathbf{k},(j,\mathbf{r},i)}^a$ commutes with all the modulation operators $M_{\mathbf{l}}$. These modulation operators are defined on $L^2(\mathbb{T}^d)$ by $M_{\mathbf{l}}\omega(\boldsymbol{\xi}) := e_{\mathbf{l}}(\boldsymbol{\xi})\omega(\boldsymbol{\xi})$. Hence, each $S_{\mathbf{k},(j,\mathbf{r},i)}^a$ is a multiplicative operator (e.g. [37, Corollary 2.12.7]) in the following sense:

$$(S_{\mathbf{k},(j,\mathbf{r},i)}^a \omega)(\boldsymbol{\xi}) = \omega(\boldsymbol{\xi}) |\det(A)|^{-j/2} e^{-2\pi i \langle \mathbf{r}, (A^{*-j}(\boldsymbol{\xi} + \mathbf{k})) \rangle} \widehat{\psi}_i^a(A^{*-j}(\boldsymbol{\xi} + \mathbf{k})),$$

for all $\omega \in L^2(\mathbb{T}^d)$. We denote the symbol for this operator again by $S_{\mathbf{k},(j,\mathbf{r},i)}^a(\cdot)$, so that,

$$S_{\mathbf{k},(j,\mathbf{r},i)}^a(\boldsymbol{\xi}) = |\det(A)|^{-j/2} e^{-2\pi i \langle \mathbf{r}, (A^{*-j}(\boldsymbol{\xi} + \mathbf{k})) \rangle} \widehat{\psi}_i^a(A^{*-j}(\boldsymbol{\xi} + \mathbf{k})).$$

Note that $S_{\mathbf{k},(j,\mathbf{r},i)}^a(\cdot)$ is an essentially bounded \mathbb{Z}^d -periodic function.

Let $S^a(\cdot)$ denote the $\mathbb{Z}^d \times J$ matrix of the symbols $S_{\mathbf{k},(j,\mathbf{r},i)}^a(\cdot)$, then

$$(S^a \omega)(\boldsymbol{\xi}) = S^a(\boldsymbol{\xi}) \omega(\boldsymbol{\xi}) \quad \text{for all } \omega \in L^2(\mathbb{T}^d, l^2(J)).$$

Now, the adjoint of S^a can be represented by the $J \times \mathbb{Z}^d$ matrix of operators on $L^2(\mathbb{T}^d)$ such that the $((j, \mathbf{r}, i), \mathbf{k})$ -th entry is $S_{\mathbf{k},(j,\mathbf{r},i)}^{a*}$. Since $S_{\mathbf{k},(j,\mathbf{r},i)}^{a*}$ is the adjoint of a multiplicative operator, it itself, is a multiplicative operator with symbol $\overline{S_{\mathbf{k},(j,\mathbf{r},i)}^a(\cdot)}$. Therefore,

$$(S^{a*} \omega)(\boldsymbol{\xi}) = S^a(\boldsymbol{\xi})^* \omega(\boldsymbol{\xi}) \quad \text{for all } \omega \in L^2(\mathbb{T}^d, l^2(\mathbb{Z}^d)).$$

Similarly, we define $S^s : L^2(\mathbb{T}^d, l^2(J)) \rightarrow L^2(\mathbb{T}^d, l^2(\mathbb{Z}^d))$, via

$$S^s(e_{\mathbf{l}}, \delta_{(j,\mathbf{r},i)}) = U(T_{\mathbf{l}} D^j T_{\mathbf{r}} \psi_i^s) \quad \text{for all } \mathbf{l} \in \mathbb{Z}^d, \quad (j, \mathbf{r}, i) \in J,$$

where we adopt the convention $\psi_0^s = \phi^s$. Arguing as before for S^a , we obtain the following expression for S^s :

$$(S^s \omega)(\boldsymbol{\xi}) = S^s(\boldsymbol{\xi}) \omega(\boldsymbol{\xi}) \quad \text{for all } \omega \in L^2(\mathbb{T}^d, l^2(J)),$$

where $S^s(\cdot)$ denotes the $\mathbb{Z}^d \times J$ matrix of the symbols,

$$S_{\mathbf{k},(j,\mathbf{r},i)}^s(\boldsymbol{\xi}) = |\det(A)|^{-j/2} e^{-2\pi i \langle \mathbf{r}, (A^{*-j}(\boldsymbol{\xi} + \mathbf{k})) \rangle} \widehat{\psi}_i^s(A^{*-j}(\boldsymbol{\xi} + \mathbf{k})).$$

The families, $X_{\phi\psi}^a$ and $X_{\phi\psi}^s$, is a pair of dual frames, if and only if, $S^s S^{a*} = I_{L^2(\mathbb{T}^d, l^2(\mathbb{Z}^d))}$, i.e.

$$S^s(\boldsymbol{\xi}) S^a(\boldsymbol{\xi})^* = I_{l^2(\mathbb{Z}^d)} \quad \text{for a.e. } \boldsymbol{\xi} \in \mathbb{T}^d. \quad (3.19)$$

The (\mathbf{k}, \mathbf{l}) -th entry of $S^s(\boldsymbol{\xi}) S^a(\boldsymbol{\xi})^*$ is given by

$$\begin{aligned} & (S^s(\boldsymbol{\xi}) S^a(\boldsymbol{\xi})^*)_{(\mathbf{k}, \mathbf{l})} \\ &= \sum_{j=0}^{\infty} \sum_{i=1}^n |\det(A)|^{-j} \sum_{\mathbf{r} \in \mathbb{Z}^d / (A^{*j} \mathbb{Z}^d)} e^{2\pi i \langle \mathbf{r}, A^{*-j}(\mathbf{k} - \mathbf{l}) \rangle} \widehat{\psi}_i^s(A^{*-j}(\boldsymbol{\xi} + \mathbf{k})) \overline{\widehat{\psi}_i^a(A^{*-j}(\boldsymbol{\xi} + \mathbf{l}))} \\ &+ \widehat{\phi}^s(\boldsymbol{\xi} + \mathbf{k}) \overline{\widehat{\phi}^a(\boldsymbol{\xi} + \mathbf{l})}. \end{aligned} \quad (3.20)$$

Define $j_0 : \mathbb{Z}^d \rightarrow \mathbb{Z}$ via

$$j_0(\mathbf{l}) = \sup\{j : A^{*-j}(\mathbf{l}) \in \mathbb{Z}^d\} \text{ for all } \mathbf{l} \in \mathbb{Z}^d, \quad (3.21)$$

with the convention that $j_0(0) = +\infty$.

Now, if $j > j_0(\mathbf{k} - \mathbf{l})$, then $A^{*-j}(\mathbf{k} - \mathbf{l}) \notin \mathbb{Z}^d$ and therefore $e_{A^{*-j}(\mathbf{k} - \mathbf{l})}$ is not the identity character on $\mathbb{Z}^d / (A^{*j} \mathbb{Z}^d)$. On the other hand, if $j \leq j_0(\mathbf{k} - \mathbf{l})$ then $A^{*-j}(\mathbf{k} - \mathbf{l}) \in \mathbb{Z}^d$ and $e_{A^{*-j}(\mathbf{k} - \mathbf{l})}$ is the identity character on $\mathbb{Z}^d / (A^{*j} \mathbb{Z}^d)$. Thus, using Lemma 3.1.6, we conclude

$$|\det(A)|^{-j} \sum_{\mathbf{r} \in \mathbb{Z}^d / (A^{*j} \mathbb{Z}^d)} e^{2\pi i \langle \mathbf{r}, A^{*-j}(\mathbf{k} - \mathbf{l}) \rangle} = \begin{cases} 0 & \text{for } j > j_0(\mathbf{k} - \mathbf{l}) \\ 1 & \text{for } j \leq j_0(\mathbf{k} - \mathbf{l}) \end{cases}.$$

Hence, for $\mathbf{k} \neq \mathbf{l}$, (3.20) reduces to,

$$(S^s(\boldsymbol{\xi})S^a(\boldsymbol{\xi}^*))_{(\mathbf{k},\mathbf{l})} = \sum_{j=0}^{j_0(\mathbf{k}-\mathbf{l})} \sum_{i=1}^n \widehat{\psi}_i^s(A^{*-j}(\boldsymbol{\xi} + \mathbf{k})) \overline{\widehat{\psi}_i^a(A^{*-j}(\boldsymbol{\xi} + \mathbf{l}))} \\ + \widehat{\phi}^s(\boldsymbol{\xi} + \mathbf{k}) \overline{\widehat{\phi}^a(\boldsymbol{\xi} + \mathbf{l})}.$$

Thus using (3.19), $X_{\phi\psi}^a$ and $X_{\phi\psi}^a$ is a pair of dual frames if and only if the following condition holds for a.e. $\boldsymbol{\xi} \in \mathbb{T}^d$ and $\mathbf{k}, \mathbf{l} \in \mathbb{Z}^d$:

$$\sum_{j=0}^{j_0(\mathbf{k}-\mathbf{l})} \sum_{i=1}^n \widehat{\psi}_i^s(A^{*-j}(\boldsymbol{\xi} + \mathbf{k})) \overline{\widehat{\psi}_i^a(A^{*-j}(\boldsymbol{\xi} + \mathbf{l}))} + \widehat{\phi}^s(\boldsymbol{\xi} + \mathbf{k}) \overline{\widehat{\phi}^a(\boldsymbol{\xi} + \mathbf{l})} = \delta_{\mathbf{k},\mathbf{l}}. \quad (3.22)$$

Changing variables, in the previous equation gives that it is equivalent to:

$$\sum_{j=0}^{j_0(\mathbf{l})} \sum_{i=1}^n \widehat{\psi}_i^s(A^{*-j}\boldsymbol{\xi}) \overline{\widehat{\psi}_i^a(A^{*-j}(\boldsymbol{\xi} + \mathbf{l}))} + \widehat{\phi}^s(\boldsymbol{\xi}) \overline{\widehat{\phi}^a(\boldsymbol{\xi} + \mathbf{l})} = \delta_{\mathbf{l},0}, \quad (3.23)$$

for a.e. $\boldsymbol{\xi} \in \mathbb{R}^d$ and $\mathbf{l} \in \mathbb{Z}^d$. This finishes the first part of the proof.

Now, we proceed to the second part of the proof. In this part we show that (3.23) holds if and only if (3.18) holds. We will first assume (3.18) holds and prove that (3.23) holds

for all $\mathbf{l} \neq 0$. Using the two-scale relations ((3.16) and (3.17)) and (3.18) we obtain,

$$\begin{aligned}
 & \sum_{j=0}^{j_0(\mathbf{l})} \sum_{i=1}^n \widehat{\psi}_i^s(A^{*-j}\boldsymbol{\xi}) \overline{\widehat{\psi}_i^a(A^{*-j}(\boldsymbol{\xi} + \mathbf{l}))} + \widehat{\phi}^s(\boldsymbol{\xi}) \overline{\widehat{\phi}^a(\boldsymbol{\xi} + \mathbf{l})} = \\
 = & \sum_{j=1}^{j_0(\mathbf{l})} \sum_{i=1}^n \widehat{\psi}_i^s(A^{*-j}\boldsymbol{\xi}) \overline{\widehat{\psi}_i^a(A^{*-j}(\boldsymbol{\xi} + \mathbf{l}))} \\
 & + \widehat{\phi}^s(A^{*-1}\boldsymbol{\xi}) \overline{\widehat{\phi}^a(A^{*-1}(\boldsymbol{\xi} + \mathbf{l}))} \left(\sum_{i=0}^n H_i^s(A^{*-1}\boldsymbol{\xi}) \overline{H_i^a(A^{*-1}(\boldsymbol{\xi} + \mathbf{l}))} \right) \\
 = & \sum_{j=1}^{j_0(\mathbf{l})} \sum_{i=1}^n \widehat{\psi}_i^s(A^{*-j}\boldsymbol{\xi}) \overline{\widehat{\psi}_i^a(A^{*-j}(\boldsymbol{\xi} + \mathbf{l}))} + \widehat{\phi}^s(A^{*-1}\boldsymbol{\xi}) \overline{\widehat{\phi}^a(A^{*-1}(\boldsymbol{\xi} + \mathbf{l}))} \\
 & \vdots \\
 = & \sum_{i=1}^n \widehat{\psi}_i^s(A^{*-j_0(\mathbf{l})}\boldsymbol{\xi}) \overline{\widehat{\psi}_i^a(A^{*-j_0(\mathbf{l})}(\boldsymbol{\xi} + \mathbf{l}))} + \\
 & \widehat{\phi}^s(A^{*-j_0(\mathbf{l})}\boldsymbol{\xi}) \overline{\widehat{\phi}^a(A^{*-j_0(\mathbf{l})}(\boldsymbol{\xi} + \mathbf{l}))} \left(\sum_{i=0}^n H_i^s(A^{*-j_0(\mathbf{l})}\boldsymbol{\xi}) \overline{H_i^a(A^{*-j_0(\mathbf{l})}(\boldsymbol{\xi} + \mathbf{l}))} \right) \\
 = & \sum_{i=1}^n \widehat{\psi}_i^s(A^{*-j_0(\mathbf{l})}\boldsymbol{\xi}) \overline{\widehat{\psi}_i^a(A^{*-j_0(\mathbf{l})}(\boldsymbol{\xi} + \mathbf{l}))} + \widehat{\phi}^s(A^{*-j_0(\mathbf{l})}\boldsymbol{\xi}) \overline{\widehat{\phi}^a(A^{*-j_0(\mathbf{l})}(\boldsymbol{\xi} + \mathbf{l}))} \\
 = & \widehat{\phi}^s(A^{*-(j_0(\mathbf{l})+1)}\boldsymbol{\xi}) \overline{\widehat{\phi}^a(A^{*-(j_0(\mathbf{l})+1)}(\boldsymbol{\xi} + \mathbf{l}))}. \\
 & \left(\sum_{i=0}^n H_i^s(A^{*-(j_0(\mathbf{l})+1)}\boldsymbol{\xi}) \overline{H_i^a(A^{*-(j_0(\mathbf{l})+1)}(\boldsymbol{\xi} + \mathbf{l}))} \right) \\
 = & 0.
 \end{aligned}$$

Next, using the hypothesis (3.18), we show that (3.23) holds for $\mathbf{l} = 0$,

$$\begin{aligned}
 & \sum_{j=0}^{\infty} \sum_{i=1}^n \widehat{\psi}_i^s(A^{*-j}\boldsymbol{\xi}) \overline{\widehat{\psi}_i^a(A^{*-j}\boldsymbol{\xi})} + \widehat{\phi}^s(\boldsymbol{\xi}) \overline{\widehat{\phi}^a(\boldsymbol{\xi})} = \\
 = & \sum_{j=1}^{\infty} \sum_{i=1}^n \widehat{\psi}_i^s(A^{*-j}\boldsymbol{\xi}) \overline{\widehat{\psi}_i^a(A^{*-j}\boldsymbol{\xi})} \\
 & + \widehat{\phi}^s(A^{*-1}\boldsymbol{\xi}) \overline{\widehat{\phi}^a(A^{*-1}\boldsymbol{\xi})} \left(\sum_{i=0}^n H_i^s(A^{*-1}\boldsymbol{\xi}) \overline{H_i^a(A^{*-1}\boldsymbol{\xi})} \right) \\
 = & \sum_{j=1}^{\infty} \sum_{i=1}^n \widehat{\psi}_i^s(A^{*-j}\boldsymbol{\xi}) \overline{\widehat{\psi}_i^a(A^{*-j}\boldsymbol{\xi})} + \widehat{\phi}^s(A^{*-1}\boldsymbol{\xi}) \overline{\widehat{\phi}^a(A^{*-1}\boldsymbol{\xi})} \\
 & \vdots \\
 = & \sum_{j=N}^{\infty} \sum_{i=1}^n \widehat{\psi}_i^s(A^{*-j}\boldsymbol{\xi}) \overline{\widehat{\psi}_i^a(A^{*-j}\boldsymbol{\xi})} \\
 & + \widehat{\phi}^s(A^{*-N}\boldsymbol{\xi}) \overline{\widehat{\phi}^a(A^{*-N}\boldsymbol{\xi})} \left(\sum_{i=0}^n H_i^s(A^{*-N}\boldsymbol{\xi}) \overline{H_i^a(A^{*-N}\boldsymbol{\xi})} \right) \\
 = & \underbrace{\sum_{j=N}^{\infty} \sum_{i=1}^n \widehat{\psi}_i^s(A^{*-j}\boldsymbol{\xi}) \overline{\widehat{\psi}_i^a(A^{*-j}\boldsymbol{\xi})}}_{\rightarrow 0 \text{ as } N \rightarrow \infty \text{ because the series converges for a.e. } \boldsymbol{\xi} \in \mathbb{R}^d} \\
 & + \underbrace{\widehat{\phi}^s(A^{*-N}\boldsymbol{\xi}) \overline{\widehat{\phi}^a(A^{*-N}\boldsymbol{\xi})}}_{\rightarrow 1 \text{ as } N \rightarrow \infty \text{ by (3.15) and continuity of } \widehat{\phi}^s, \widehat{\phi}^a \text{ at the origin.}} \\
 \rightarrow & 1 \text{ as } N \rightarrow \infty \quad \text{for almost every } \boldsymbol{\xi} \in L^2(\mathbb{R}^d).
 \end{aligned}$$

Thus, we have shown that (3.18) implies (3.23).

Next we establish that the converse implication is valid. Assume first, that (3.18) holds for $\mathbf{q} = 0$. Under the assumption, the calculations we carried out to prove that (3.18) implies (3.23) for $\mathbf{l} \neq 0$ are still valid for almost every $\boldsymbol{\xi}$ and all $\mathbf{l} \in \mathbb{Z}^d$. Now, pick $\mathbf{q} \in (A^{*-1})\mathbb{Z}^d/\mathbb{Z}^d$. We have $A^*\mathbf{q} \in \mathbb{Z}^d$. If \mathbf{p} is an arbitrary integer grid point, i.e. $\mathbf{p} \in \mathbb{Z}^d$ set $\mathbf{l} := A^*(\mathbf{q} + \mathbf{p})$. Obviously $\mathbf{l} \in \mathbb{Z}^d$, since A is expansive and, thus, A^* leaves the lattice \mathbb{Z}^d invariant. Observe $j_0(\mathbf{l}) = 0$, because $\mathbf{q} + \mathbf{p}$ does not belong to the integer grid. Since

(3.23) is valid for all $\mathbf{l} \neq 0$, we deduce

$$\begin{aligned}
 0 &= \sum_{i=1}^n \widehat{\psi}_i^s(\boldsymbol{\xi}) \overline{\widehat{\psi}_i^a(\boldsymbol{\xi} + \mathbf{l})} + \widehat{\phi}^s(\boldsymbol{\xi}) \overline{\widehat{\phi}^a(\boldsymbol{\xi} + \mathbf{l})} \\
 &= \widehat{\phi}^s(A^{*-1}\boldsymbol{\xi}) \overline{\widehat{\phi}^a(A^{*-1}(\boldsymbol{\xi} + \mathbf{l}))} \left(\sum_{i=0}^n H_i^s(A^{*-1}\boldsymbol{\xi}) \overline{H_i^a(A^{*-1}(\boldsymbol{\xi} + \mathbf{l}))} \right) \\
 &= \widehat{\phi}^s(A^{*-1}\boldsymbol{\xi}) \overline{\widehat{\phi}^a(A^{*-1}\boldsymbol{\xi} + \mathbf{q} + \mathbf{p})} \left(\sum_{i=0}^n H_i^s(A^{*-1}\boldsymbol{\xi}) \overline{H_i^a(A^{*-1}\boldsymbol{\xi} + \mathbf{q} + \mathbf{p})} \right),
 \end{aligned}$$

for a.e. $\boldsymbol{\xi}$ in \mathbb{R}^d . Now, take $\boldsymbol{\xi}$ and $\boldsymbol{\xi} + \mathbf{q}$ in $\sigma(V_0^a) \cap \sigma(V_0^s)$ such that $A^*\boldsymbol{\xi}$ belongs to the set of points in \mathbb{R}^d for which (3.23) holds. The fact that (3.23) is equivalent to (3.22) implies that, if (3.23) holds for a $\boldsymbol{\xi} \in \mathbb{R}^d$ then, (3.23) holds for all integer translates of this point. Next, apply the previous equations for $A^*(\boldsymbol{\xi} + \boldsymbol{\lambda})$ instead of $\boldsymbol{\xi}$, where $\boldsymbol{\lambda} \in \mathbb{Z}^d$. Then,

$$0 = \widehat{\phi}^s(\boldsymbol{\xi} + \boldsymbol{\lambda}) \overline{\widehat{\phi}^a(\boldsymbol{\xi} + \mathbf{q} + \mathbf{p})} \left(\sum_{i=0}^n H_i^s(\boldsymbol{\xi}) \overline{H_i^a(\boldsymbol{\xi} + \mathbf{q})} \right),$$

due to the \mathbb{Z}^d -periodicity of H_i^a and H_i^s . Since $\mathbf{p}, \boldsymbol{\lambda}$ are arbitrary integers and $\boldsymbol{\xi}, \boldsymbol{\xi} + \mathbf{q} \in \sigma(V_0^a) \cap \sigma(V_0^s)$ there exist some $\boldsymbol{\lambda}_0$ and \mathbf{p}_0 for which

$$\widehat{\phi}^s(\boldsymbol{\xi} + \boldsymbol{\lambda}_0) \overline{\widehat{\phi}^a(\boldsymbol{\xi} + \mathbf{q} + \mathbf{p}_0)} \neq 0.$$

Thus,

$$\sum_{i=0}^n H_i^s(\boldsymbol{\xi}) \overline{H_i^a(\boldsymbol{\xi} + \mathbf{q})} = 0.$$

In order to complete the proof of the theorem we need to establish that (3.18) holds for $\mathbf{q} = 0$. To verify this set $\mathbf{l} = 0$ in (3.23):

$$\sum_{j=0}^{\infty} \sum_{i=1}^n \widehat{\psi}_i^s(A^{*-j}\boldsymbol{\xi}) \overline{\widehat{\psi}_i^a(A^{*-j}(\boldsymbol{\xi}))} + \widehat{\phi}^s(\boldsymbol{\xi}) \overline{\widehat{\phi}^a(\boldsymbol{\xi})} = 1.$$

Observe that this implies,

$$\sum_{j=0}^{\infty} \sum_{i=1}^n \widehat{\psi}_i^s(A^{*-j+1}\boldsymbol{\xi}) \overline{\widehat{\psi}_i^a(A^{*-j+1}(\boldsymbol{\xi}))} + \widehat{\phi}^s(A^*\boldsymbol{\xi}) \overline{\widehat{\phi}^a(A^*\boldsymbol{\xi})} = 1.$$

Using the two scale relations, (3.16) and (3.17), we infer,

$$\begin{aligned} & \sum_{j=0}^{\infty} \sum_{i=1}^n \widehat{\psi}_i^s(A^{*-j+1}\boldsymbol{\xi}) \overline{\widehat{\psi}_i^a(A^{*-j+1}\boldsymbol{\xi})} + \widehat{\phi}^s(A^*\boldsymbol{\xi}) \overline{\widehat{\phi}^a(A^*\boldsymbol{\xi})} = \\ & = \sum_{j=0}^{\infty} \sum_{i=1}^n \widehat{\psi}_i^s(A^{*-j}\boldsymbol{\xi}) \overline{\widehat{\psi}_i^a(A^{*-j}\boldsymbol{\xi})} + \widehat{\phi}^s(\boldsymbol{\xi}) \overline{\widehat{\phi}^a(\boldsymbol{\xi})} \left(\sum_{i=0}^n H_i^s(\boldsymbol{\xi}) \overline{H_i^a(\boldsymbol{\xi})} \right), \end{aligned}$$

hence,

$$\begin{aligned} & \sum_{j=0}^{\infty} \sum_{i=1}^n \widehat{\psi}_i^s(A^{*-j}\boldsymbol{\xi}) \overline{\widehat{\psi}_i^a(A^{*-j}\boldsymbol{\xi})} + \widehat{\phi}^s(\boldsymbol{\xi}) \overline{\widehat{\phi}^a(\boldsymbol{\xi})} = \\ & = \sum_{j=0}^{\infty} \sum_{i=1}^n \widehat{\psi}_i^s(A^{*-j}\boldsymbol{\xi}) \overline{\widehat{\psi}_i^a(A^{*-j}\boldsymbol{\xi})} + \widehat{\phi}^s(\boldsymbol{\xi}) \overline{\widehat{\phi}^a(\boldsymbol{\xi})} \left(\sum_{i=0}^n H_i^s(\boldsymbol{\xi}) \overline{H_i^a(\boldsymbol{\xi})} \right). \end{aligned}$$

Therefore, $\sum_{i=0}^n H_i^s(\boldsymbol{\xi}) \overline{H_i^a(\boldsymbol{\xi})} = 1$ for a.e. $\boldsymbol{\xi} \in \sigma(V_0^a) \cap \sigma(V_0^s)$. \square

Remark 3.1.11 The conditions on the filters in (3.18) are similar to those required for Proposition 5.2 in [38] (also [30]), from which the so-called Mixed Extension Principle follows. The statement of the previous theorem does not require the so-called Mixed Fundamental Function that is present in the said result in [38]. At first glance, this fact seems contradictory but it is not. Under the assumptions of Theorem 3.1.10, the Mixed Fundamental Function is equal to one almost everywhere on $\sigma(V_0^a) \cap \sigma(V_0^s)$. This follows from the proof of the so-called Mixed Oblique Extension Principle (Corollary 5.3 in [38]). Let us recall the statement of this result:

Theorem 3.1.12 [38] [Mixed Oblique Extension Principle]: *Let ϕ^a and ϕ^s be refinable functions in $L^2(\mathbb{R}^d)$ such that $\widehat{\phi}^a$ and $\widehat{\phi}^s$ are continuous at the origin and*

$$\lim_{|\boldsymbol{\xi}| \rightarrow 0} \widehat{\phi}^a(\boldsymbol{\xi}) = \widehat{\phi}^s(\boldsymbol{\xi}) = 1. \quad (3.24)$$

3.1. EXTENSION PRINCIPLES REVISITED

Let H_0^a and $H_0^s \in L^\infty(\mathbb{T}^d)$, be the associated low pass filters. Furthermore, let H_i^a, H_i^s for $i = 1, \dots, m$, be \mathbb{Z}^d -periodic measurable functions and define m pairs of wavelets ψ_i^a, ψ_i^s $i = 1, \dots, m$, by

$$\widehat{\psi}_i^a(A^* \cdot) = H_i^a \widehat{\phi}, \quad (3.25)$$

$$\widehat{\psi}_i^s(A^* \cdot) = H_i^s \widehat{\phi}. \quad (3.26)$$

Assume $H_i^a, H_i^s \in L^\infty(\mathbb{T}^d)$ for all $i = 0, \dots, m$, and the affine families Ψ^a and Ψ^s are Bessel. Suppose we can find a \mathbb{Z}^d -periodic function Θ that satisfies the following:

1. Θ is essentially bounded, continuous at the origin, and $\Theta(0) = 1$.
2. If $\mathbf{q} \in (A^{*-1}\mathbb{Z}^d)/\mathbb{Z}^d \setminus \{0\}$ and $\boldsymbol{\xi}, \boldsymbol{\xi} + \mathbf{q} \in \sigma(V_0^a) \cap \sigma(V_0^s)$, then

$$\Theta(A^* \boldsymbol{\xi}) H_0^s(\boldsymbol{\xi}) \overline{H_0^a(\boldsymbol{\xi} + \mathbf{q})} + \sum_{i=1}^m H_i^s(\boldsymbol{\xi}) \overline{H_i^a(\boldsymbol{\xi} + \mathbf{q})} = 0.$$

and

$$\Theta(A^* \boldsymbol{\xi}) H_0^s(\boldsymbol{\xi}) \overline{H_0^a(\boldsymbol{\xi})} + \sum_{i=1}^m H_i^s(\boldsymbol{\xi}) \overline{H_i^a(\boldsymbol{\xi})} = \Theta(\boldsymbol{\xi}).$$

Then Ψ^a and Ψ^s form a pair of dual frames.

The proof of this result establishes that Θ is equal to the mixed fundamental function Θ_M a.e. on $\sigma(V_0^a) \cap \sigma(V_0^s)$. The condition that the sets $X_{\phi\psi}^a$ and $X_{\phi\psi}^s$ are Bessel implies that the affine families Ψ^a and Ψ^s are Bessel (see Corollary 3.1.9). Condition 3.18 is the same as the conditions on the filters in this result with Θ equal to 1 a.e. on $\sigma(V_0^a) \cap \sigma(V_0^s)$. Therefore, in our setting Θ_M is equal to one almost everywhere on $\sigma(V_0^a) \cap \sigma(V_0^s)$.

3.2 Examples of Isotropic Wavelet Frames

In this section we describe two examples of Isotropic wavelet frames. With the help of Theorems 3.1.1, 3.1.7, 3.1.4, and 3.1.10, the problem of designing wavelet frames is transformed into a problem of designing the corresponding filters. We illustrate this in Examples 3.2.1 and 3.2.2. In Example 3.2.1 we construct a Parseval frame while in Example 3.2.2 we construct a pair of dual frames. Recall that we define the dilation operator with respect to a radially expansive matrix $A = aR$, where R is a rotation. The constant $a > 0$ will be used in the examples below.

Example 3.2.1 As pointed out at the beginning of this section, we obtain the wavelet frame, by designing the corresponding filters and then invoking the appropriate extension principle. We begin with the low pass filter H_0 , a smooth \mathbb{Z}^d -periodic function such that

- $H_0 = 1$ inside the ball of radius b_1 ,
- $H_0 = 0$ on $\mathbb{T}^d \setminus B(0, b_0)$,
- $H_0|_{B(0, b_0)}$ is radial,

where $\frac{1}{2a^2} < b_1 < b_0 < \frac{1}{2a}$.

If ϕ by $\hat{\phi} = H_0(A^{*-1} \cdot)\chi_{\mathbb{T}^d}$, then ϕ satisfies conditions (3.1) and (3.2) of Theorem 3.1.1.

Now, let h be a \mathbb{Z}^d -periodic function defined by,

$$h(\boldsymbol{\xi}) = \sqrt{\frac{1 - H_0^2(\boldsymbol{\xi})}{|\det(A)|}}. \quad (3.27)$$

Using h we define the high pass filters as follows,

$$H_i(\boldsymbol{\xi}) = e_{\mathbf{q}_{i-1}}(\boldsymbol{\xi})h(\boldsymbol{\xi}), \quad i = 1, \dots, |\det(A)|, \quad (3.28)$$

where $\{\mathbf{q}_l : l = 0, 1, 2, \dots, |\det(A)| - 1\}$ are the representatives of the quotient group $\mathbb{Z}^d / (A^* \mathbb{Z}^d)$.

We claim $\mathbf{H}\mathbf{H}^* = \mathbf{I}$, where \mathbf{H} is defined by (3.1.2). Hence, by Theorem 3.1.1, the set

$$\left\{ D_A^j T_k \psi_i : j \in \mathbb{Z}, k \in \mathbb{Z}^d, i = 1, \dots, |\det(A)| \right\},$$

forms a Parseval Frame for $L^2(\mathbb{R}^d)$. Also, by Theorem 3.1.7, the set $X_{\phi\psi}$ is a Parseval frame for $L^2(\mathbb{R}^d)$.

To prove our claim, we use (3.27) and (3.28) to obtain

$$(\mathbf{H}\mathbf{H}^*)_{1,1}(\boldsymbol{\xi}) = \sum_{i=0}^{|\det(A)|} |H_i(\boldsymbol{\xi})|^2 = H_0^2(\boldsymbol{\xi}) + |\det(A)| \frac{1 - H_0^2(\boldsymbol{\xi})}{|\det(A)|} = 1 \text{ for all } \boldsymbol{\xi} \in \mathbb{T}^d,$$

and

$$(\mathbf{H}\mathbf{H}^*)_{i+1,i+1}(\boldsymbol{\xi}) = (\mathbf{H}\mathbf{H}^*)_{1,1}(\boldsymbol{\xi} + A^{*-1} \mathbf{q}_{i-1}) = 1 \text{ for all } \boldsymbol{\xi} \in \mathbb{T}^d, i = 1, \dots, |\det(A)|.$$

Next we want to show that the off-diagonal entries of $\mathbf{H}\mathbf{H}^*$ are zero. To do this we observe that the supports of $H_0(\cdot + A^{*-1} \mathbf{q}_{i-1})$ and $\overline{H_0(\cdot + A^{*-1} \mathbf{q}_{j-1})}$ are disjoint by definition of H_0 . Thus,

$$H_0(\boldsymbol{\xi} + A^{*-1} \mathbf{q}_{i-1}) \overline{H_0(\boldsymbol{\xi} + A^{*-1} \mathbf{q}_{j-1})} = 0 \quad \text{for all } \boldsymbol{\xi} \in \mathbb{T}^d, i \neq j.$$

Hence,

$$\begin{aligned} & (\mathbf{H}\mathbf{H}^*)_{j,k}(\boldsymbol{\xi}) \\ &= \sum_{i=0}^{|\det(A)|} H_i(\boldsymbol{\xi} + A^{*-1} \mathbf{q}_{j-1}) \overline{H_i(\boldsymbol{\xi} + A^{*-1} \mathbf{q}_{k-1})} \\ &= \sum_{i=1}^{|\det(A)|} H_i(\boldsymbol{\xi} + A^{*-1} \mathbf{q}_{j-1}) \overline{H_i(\boldsymbol{\xi} + A^{*-1} \mathbf{q}_{k-1})} \\ &= \underbrace{h(\boldsymbol{\xi} + A^{*-1} \mathbf{q}_{j-1}) \overline{h(\boldsymbol{\xi} + A^{*-1} \mathbf{q}_{k-1})}}_{=: s_{j-1,k-1}} \left(\sum_{i=1}^{|\det(A)|} e_{\mathbf{q}_{i-1}}(\boldsymbol{\xi} + A^{*-1} \mathbf{q}_{j-1}) \overline{e_{\mathbf{q}_{i-1}}(\boldsymbol{\xi} + A^{*-1} \mathbf{q}_{k-1})} \right). \end{aligned}$$

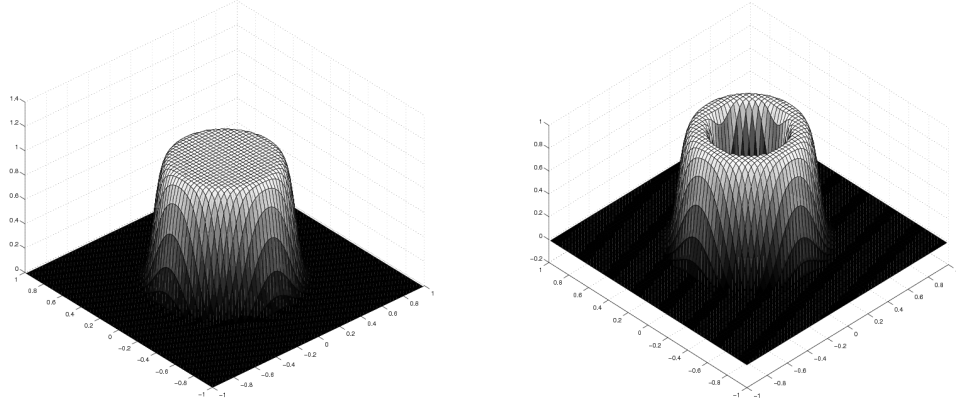


Figure 3.1: Fourier transforms of a typical isotropic refinable function (left) and wavelet (right).

Now we need to establish that $s_{j,k} = 0$ for all $j \neq k$.

$$\begin{aligned} s_{j,k} &= \sum_{i=1}^{|\det(A)|} e_{\mathbf{q}_{i-1}}(\boldsymbol{\xi} + A^{*-1}\mathbf{q}_j) \overline{e_{\mathbf{q}_{i-1}}(\boldsymbol{\xi} + A^{*-1}\mathbf{q}_k)} \\ &= \sum_{i=1}^{|\det(A)|} e_{\mathbf{q}_{i-1}}(A^{*-1}\mathbf{q}_j - A^{*-1}\mathbf{q}_k) = \sum_{i=0}^{|\det(A)|-1} e^{2\pi i \langle \mathbf{q}_i, A^{*-1}(\mathbf{q}_j - \mathbf{q}_k) \rangle}. \end{aligned}$$

Since $j \neq k$, we have $\mathbf{q}_j - \mathbf{q}_k \neq 0$ and $A^{*-1}(\mathbf{q}_j - \mathbf{q}_k) \notin \mathbb{Z}^d$. Therefore, $e_{A^{*-1}(\mathbf{q}_j - \mathbf{q}_k)}$ is not the identity character on the quotient group $\mathbb{Z}^d / (A^*\mathbb{Z}^d)$ and by Lemma 3.1.6, $s_{j,k} = 0$. This completes the proof of the claim $\mathbf{H}\mathbf{H}^* = \mathbf{I}$.

Figure 3.1 shows the graphs of the Fourier transform of the 2- D version of a typical isotropic scaling function and isotropic wavelet, obtained in this example while Figure 3.2 shows their space domain graphs.

One concrete realization of the construction described in Example 3.2.1 is obtained by using the so-called ‘Root Raised Cosine’ filter as a low pass filter. Here, we use the dyadic

3.2. EXAMPLES OF ISOTROPIC WAVELET FRAMES

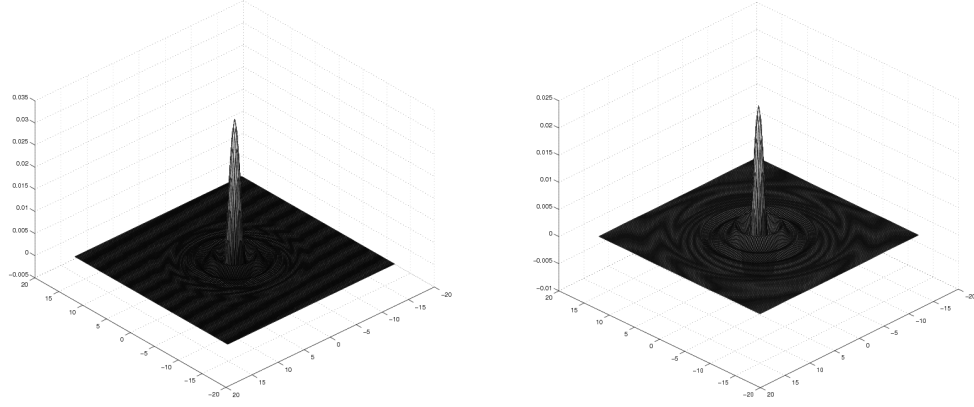


Figure 3.2: Isotropic refinable function (left) and wavelet (right) in the space domain.

dilation matrix to define the dilation operator. The low pass filter is defined by

$$H_0(\boldsymbol{\xi}) = \begin{cases} 1 & \text{for } |\boldsymbol{\xi}| < 3/20 \\ \sqrt{\frac{1+\cos(10\pi|\boldsymbol{\xi}|-\frac{3\pi}{2})}{2}} & \text{for } 3/20 < |\boldsymbol{\xi}| < 1/4 \\ 0 & \text{for } |\boldsymbol{\xi}| > 1/4 \end{cases} .$$

Hence, the Fourier transform of the refinable function ϕ is given by

$$\widehat{\phi}(\boldsymbol{\xi}) = \begin{cases} 1 & \text{for } |\boldsymbol{\xi}| < 3/10 \\ \sqrt{\frac{1+\cos(5\pi|\boldsymbol{\xi}|-\frac{3\pi}{2})}{2}} & \text{for } 3/10 < |\boldsymbol{\xi}| < 1/2 \\ 0 & \text{for } |\boldsymbol{\xi}| > 1/2 \end{cases} .$$

The high pass filters are given by

$$H_i(\boldsymbol{\xi}) = \frac{e_{\mathbf{a}_{i-1}}}{2^{d/2}} \begin{cases} 0 & \text{for } |\boldsymbol{\xi}| < 3/20 \\ \sqrt{\frac{1-\cos(10\pi|\boldsymbol{\xi}|-\frac{3\pi}{2})}{2}} & \text{for } 3/20 < |\boldsymbol{\xi}| < 1/4 \\ 1 & \text{for } |\boldsymbol{\xi}| > 1/4 \end{cases} .$$

and, finally, the wavelets are defined in the frequency domain as follows:

$$\widehat{\psi}_i(2\xi) = \frac{e_{\mathbf{q}_{i-1}}}{2^{d/2}} \begin{cases} 0 & \text{for } |\xi| < 3/20 \\ \sqrt{\frac{1 - \cos(10\pi|\xi| - \frac{3\pi}{2})}{2}} & \text{for } 3/20 < |\xi| < 1/4 \\ 1 & \text{for } 1/4 < |\xi| < 3/10 \\ \sqrt{\frac{1 + \cos(5\pi|\xi| - \frac{3\pi}{2})}{2}} & \text{for } 3/10 < |\xi| < 1/2 \\ 0 & \text{for } |\xi| > 1/2 \end{cases} .$$

Example 3.2.2 In this example we produce dual frame pairs using the Mixed Extension Principle (Theorem 3.1.4) and Theorem 3.1.10. As in the previous example, all the wavelets are isotropic and the refinable function is radial. Let $\frac{1}{2a^2} < b_2 < b_1 < b_0 < \frac{1}{2a}$ (See Figure 3.3). Pick the analysis low-pass filter, a smooth, \mathbb{Z}^d -periodic function H_0^a satisfying

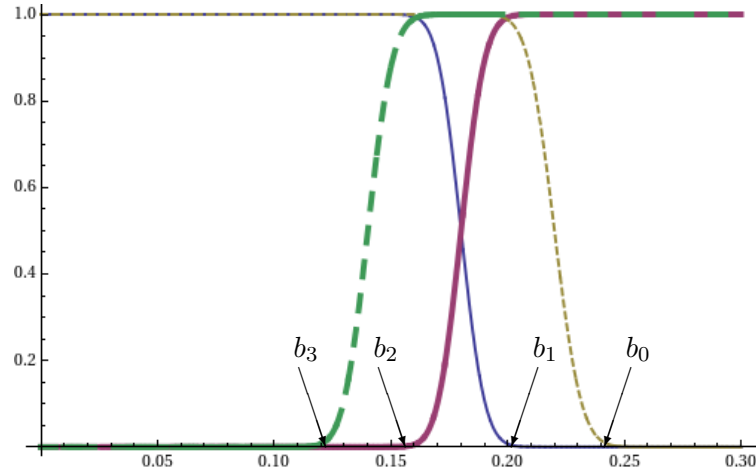


Figure 3.3: Radial profiles of the transfer functions of various filters used in Example 3.2.2. Notice that all filters lie between 0 and 1. The actual high pass filters are a constant multiple of the filters shown here (see Equation (3.29)). Since the constant differs with the dimension of the space and the dilation factor, we have not shown it here. The dashed graphs represent the synthesis filters while the solid ones represent the analysis filters.

the following three properties:

- $H_0^a = 1$ inside the ball of radius b_2 ,

- $H_0^a = 0$ on $\mathbb{T}^d \setminus B(0, b_1)$,
- $H_0^a|_{B(0, b_1)}$ is radial.

Similarly to the previous example, we define ϕ^a by $\widehat{\phi^a} = H_0^a(A^{*-1})\chi_{\mathbb{T}^d}$. Now, let h^a be a \mathbb{Z}^d -periodic function defined by,

$$h^a(\boldsymbol{\xi}) = \frac{1 - H_0^a(\boldsymbol{\xi})}{|\det(A)|^{1/2}}. \quad (3.29)$$

Using h^a we define the analysis high pass filters

$$H_i^a(\boldsymbol{\xi}) := e_{\mathbf{q}_{i-1}}(\boldsymbol{\xi})h^a(\boldsymbol{\xi}), \quad i = 1, \dots, |\det(A)|. \quad (3.30)$$

Next, let the synthesis low pass filter, a smooth, \mathbb{Z}^d -periodic function H_0^s satisfying the following three properties:

- $H_0^s = 1$ inside the ball of radius b_1 ,
- $H_0^s = 0$ on $\mathbb{T}^d \setminus B(0, b_0)$,
- $H_0^s|_{B(0, b_0)}$ is radial.

To define $|\det(A)|$ synthesis high pass filters H_i^s , $i = 1, \dots, |\det(A)|$, we use a smooth, \mathbb{Z}^d -periodic function h^s satisfying the following three properties:

- $h^s = 0$ inside the ball of radius b_3 , for some $b_3 > 0$,
- $h^s = \frac{1}{|\det(A)|^{1/2}}$ on $\mathbb{T}^d \setminus B(0, b_2)$,
- $h^s|_{\mathbb{T}^d}$ is radial,

and take $H_i^s = e_{\mathbf{q}_{i-1}}h^s$. Notice, for each $i = 0, \dots, |\det(A)|$, the pairing of the analysis and synthesis filters. Let \mathbf{H}_a and \mathbf{H}_s denote the modulation matrices corresponding to the

filters H_i^a and H_i^s respectively. (Recall that a modulation matrix is defined by (3.1.2)).

We claim that $\mathbf{H}_s \mathbf{H}_a^* = \mathbf{I}$. To prove the claim we begin by observing

$$(\mathbf{H}_s \mathbf{H}_a^*)_{1,1}(\boldsymbol{\xi}) = \sum_{i=0}^{|\det(A)|} H_i^s(\boldsymbol{\xi}) \overline{H_i^a(\boldsymbol{\xi})} = H_0^a(\boldsymbol{\xi}) + |\det(A)| \frac{1 - H_0^a(\boldsymbol{\xi})}{|\det(A)|} = 1 \quad \text{for all } \boldsymbol{\xi} \in \mathbb{T}^d.$$

Now,

$$(\mathbf{H}_s \mathbf{H}_a^*)_{i+1,i+1}(\boldsymbol{\xi}) = (\mathbf{H}_s \mathbf{H}_a^*)_{1,1}(\boldsymbol{\xi} + A^{*-1} \mathbf{q}_{i-1}) = 1 \quad \text{for all } \boldsymbol{\xi} \in \mathbb{T}^d, i = 1, \dots, |\det(A)|.$$

To establish that the off-diagonal entries are zero, observe that the supports of $H_0^s(\cdot + A^{*-1} \mathbf{q}_{i-1})$ and $\overline{H_0^a(\cdot + A^{*-1} \mathbf{q}_{j-1})}$ are disjoint, which implies

$$H_0^s(\boldsymbol{\xi} + A^{*-1} \mathbf{q}_{i-1}) \overline{H_0^a(\boldsymbol{\xi} + A^{*-1} \mathbf{q}_{j-1})} = 0 \quad \text{for all } \boldsymbol{\xi} \in \mathbb{T}^d, i \neq j.$$

Hence,

$$\begin{aligned} (\mathbf{H}_s \mathbf{H}_a^*)_{j,k}(\boldsymbol{\xi}) &= \sum_{i=0}^{|\det(A)|} H_i^s(\boldsymbol{\xi} + A^{*-1} \mathbf{q}_{j-1}) \overline{H_i^a(\boldsymbol{\xi} + A^{*-1} \mathbf{q}_{k-1})} \\ &= \sum_{i=1}^{|\det(A)|} H_i^s(\boldsymbol{\xi} + A^{*-1} \mathbf{q}_{j-1}) \overline{H_i^a(\boldsymbol{\xi} + A^{*-1} \mathbf{q}_{k-1})} \\ &= \overline{h^a(\boldsymbol{\xi} + A^{*-1} \mathbf{q}_{k-1})} \underbrace{\left(\sum_{i=1}^{|\det(A)|} e_{\mathbf{q}_{i-1}}(\boldsymbol{\xi} + A^{*-1} \mathbf{q}_{j-1}) \overline{e_{\mathbf{q}_{i-1}}(\boldsymbol{\xi} + A^{*-1} \mathbf{q}_{k-1})} \right)}_{=: s_{j-1,k-1}}. \end{aligned}$$

Recall, from Example 3.2.1 that $s_{j,k} = 0$ for all $j \neq k$. Now, the proof of the claim $\mathbf{H}_s \mathbf{H}_a^* = \mathbf{I}$ is complete.

Our next objective is to show that $\left\{ D_A^j T_k \psi_i^a : j \in \mathbb{Z}, k \in \mathbb{Z}^d, i = 1, \dots, |\det(A)| \right\}$ is a Bessel sequence. For a fixed i and a fixed j , we have,

$$\sum_{k \in \mathbb{Z}^d} \left| \left\langle f, D_A^j T_k \psi_i^a \right\rangle \right|^2 = \sum_{k \in \mathbb{Z}^d} \frac{1}{|\det(A)|^j} \left| \int_{\mathbb{R}^d} \widehat{f}(\boldsymbol{\xi}) \overline{e_k(A^{*-j} \boldsymbol{\xi})} \widehat{\psi_i^a(A^{*-j} \boldsymbol{\xi})} d\boldsymbol{\xi} \right|^2$$

$$= \sum_{k \in \mathbb{Z}^d} \frac{1}{|\det(A)|^j} \left| \sum_{\boldsymbol{l} \in \mathbb{Z}^d} \int_{A^{*j}\mathbb{T}^d} \widehat{f}(\boldsymbol{\xi} + A^{*j}\boldsymbol{l}) \overline{e_k(A^{*-j}\boldsymbol{\xi}) \widehat{\psi}_i^a(A^{*-j}\boldsymbol{\xi} + \boldsymbol{l})} d\boldsymbol{\xi} \right|^2.$$

The sum over $\boldsymbol{l} \in \mathbb{Z}^d$ in the last equality reduces to a sum over $\boldsymbol{l} \in F$, where F is a finite subset of \mathbb{Z}^d which remains *fixed for all j* , because $\widehat{\psi}_i^a$ has compact support. Now, by applying Plancherel's theorem to the $A^j\mathbb{Z}^d$ -periodic function $\sum_{\boldsymbol{l} \in \mathbb{Z}^d} \widehat{f}(\cdot + \boldsymbol{l}) \widehat{\psi}_i^a(A^{*-j}\cdot + \boldsymbol{l})$, we have

$$\begin{aligned} \sum_{i=1}^{|\det(A)|} \sum_{j=-\infty}^{\infty} \sum_{k \in \mathbb{Z}^d} \left| \langle f, D_A^j T_k \psi_i^a \rangle \right|^2 &= \sum_{i=1}^{|\det(A)|} \sum_{j=-\infty}^{\infty} \int_{A^{*j}\mathbb{T}^d} \left| \sum_{\boldsymbol{l} \in F} \widehat{f}(\boldsymbol{\xi} + A^{*j}\boldsymbol{l}) \widehat{\psi}_i^a(A^{*-j}\boldsymbol{\xi} + \boldsymbol{l}) \right|^2 d\boldsymbol{\xi} \\ &\leq \sum_{i=1}^{|\det(A)|} \sum_{j=-\infty}^{\infty} \int_{A^{*j}\mathbb{T}^d} \left[\sum_{\boldsymbol{l} \in F} \left| \widehat{f}(\boldsymbol{\xi} + A^{*j}\boldsymbol{l}) \right|^2 \right] \left[\sum_{\boldsymbol{l}' \in F} \left| \widehat{\psi}_i^a(A^{*-j}\boldsymbol{\xi} + \boldsymbol{l}') \right|^2 \right] d\boldsymbol{\xi} \\ &= \sum_{i=1}^{|\det(A)|} \sum_{j=-\infty}^{\infty} \sum_{\boldsymbol{l} \in F} \int_{A^{*j}(\mathbb{T}^d + \boldsymbol{l})} \left| \widehat{f}(\boldsymbol{\eta}) \right|^2 \left[\sum_{\boldsymbol{l}' \in F} \left| \widehat{\psi}_i^a(A^{*-j}\boldsymbol{\eta} - \boldsymbol{l} + \boldsymbol{l}') \right|^2 \right] d\boldsymbol{\eta} \\ &\leq \sum_{i=1}^{|\det(A)|} \sum_{j=-\infty}^{\infty} \sum_{\boldsymbol{l} \in F} \int_{A^{*j}(\mathbb{T}^d + \boldsymbol{l})} \left| \widehat{f}(\boldsymbol{\eta}) \right|^2 \left[\sum_{\boldsymbol{q} \in F-F} \left| \widehat{\psi}_i^a(A^{*-j}\boldsymbol{\eta} + \boldsymbol{q}) \right|^2 \right] d\boldsymbol{\eta} \\ &\leq \int_{\mathbb{R}^d} \left| \widehat{f}(\boldsymbol{\eta}) \right|^2 \sum_{i=1}^{|\det(A)|} \sum_{j=-\infty}^{\infty} \left[\sum_{\boldsymbol{q} \in F-F} \left| \widehat{\psi}_i^a(A^{*-j}\boldsymbol{\eta} + \boldsymbol{q}) \right|^2 \right] d\boldsymbol{\eta}. \end{aligned}$$

Using the definition of the ψ_i^a 's one can easily establish

$$\sum_{j=-\infty}^{\infty} \left| \widehat{\psi}_i^a(A^{*-j}\boldsymbol{\eta} + \boldsymbol{q}) \right|^2 \leq \frac{2}{|\det(A)|},$$

for every \boldsymbol{q} which implies that $\left\{ D_A^j T_k \psi_i^a : j \in \mathbb{Z}, k \in \mathbb{Z}^d, i = 1, \dots, |\det(A)| \right\}$ is a Bessel sequence.

Similarly, we can show that $\left\{ D_A^j T_k \psi_i^s : j \in \mathbb{Z}, k \in \mathbb{Z}^d, i = 1, \dots, |\det(A)| \right\}$ is a Bessel sequence too. Now, Theorem 3.1.4 implies that the families,

$$\left\{ D_A^j T_k \psi_i^a : j \in \mathbb{Z}, \boldsymbol{k} \in \mathbb{Z}^d, i = 1, \dots, |\det(A)| \right\} \quad \text{and}$$

$$\left\{ D_A^j T_k \psi_i^s : j \in \mathbb{Z}, \boldsymbol{k} \in \mathbb{Z}^d, i = 1, \dots, |\det(A)| \right\},$$

3.2. EXAMPLES OF ISOTROPIC WAVELET FRAMES

are a pair of dual frames for $L^2(\mathbb{R}^d)$. Also, by Theorem 3.1.10, the families $X_{\phi\psi}^a$ and $X_{\phi\psi}^s$ are a pair of dual frames for $L^2(\mathbb{R}^d)$.

It can be easily verified that if the synthesis high pass filters in Example 3.2.2 are replaced by $H_i^s = e_{\mathbf{q}i-1}\chi_{\mathbb{T}^d}$, the identity, $\mathbf{H}_s\mathbf{H}_a^* = \mathbf{I}$, still holds, but the families, $\left\{D_A^j T_{\mathbf{k}}\psi_i^s : j \in \mathbb{Z}, \mathbf{k} \in \mathbb{Z}^d, i = 1, \dots, |\det(A)|\right\}$ and $X_{\phi\psi}^s$ are not Bessel sequences. This shows we need the hypotheses that both affine families generated from the wavelets ψ^a and ψ^s in Theorem 3.1.4 and similarly the families $X_{\phi\psi}^a$ and $X_{\phi\psi}^s$ in Theorem 3.1.10 are Bessel sequences.

One concrete realization of the construction described in Example 3.2.2 is again obtained by using the so-called ‘Raised Cosine’ filter as a low pass filter. Once again, we use the dyadic dilation matrix to define the dilation operator. The analysis and synthesis low pass filters are defined by

$$H_0^a(\boldsymbol{\xi}) = \begin{cases} 1 & \text{for } |\boldsymbol{\xi}| < 1/8 \\ \frac{1+\cos\left(\frac{12\pi}{2}|\boldsymbol{\xi}|-\frac{3\pi}{2}\right)}{2} & \text{for } 1/8 < |\boldsymbol{\xi}| < 5/24 \\ 0 & \text{for } |\boldsymbol{\xi}| > 5/24 \end{cases} ,$$

$$H_0^s(\boldsymbol{\xi}) = \begin{cases} 1 & \text{for } |\boldsymbol{\xi}| < 5/24 \\ \frac{1+\cos\left(\frac{240\pi}{11}|\boldsymbol{\xi}|-\frac{50\pi}{11}\right)}{2} & \text{for } 5/24 < |\boldsymbol{\xi}| < 1/4 \\ 0 & \text{for } |\boldsymbol{\xi}| > 1/4 \end{cases} .$$

Hence, the Fourier transform of the scaling functions are given by the formulae,

$$\widehat{\phi^a}(\boldsymbol{\xi}) = \begin{cases} 1 & \text{for } |\boldsymbol{\xi}| < 1/4 \\ \frac{1+\cos\left(6\pi|\boldsymbol{\xi}|-\frac{3\pi}{2}\right)}{2} & \text{for } 1/4 < |\boldsymbol{\xi}| < 5/12 \\ 0 & \text{for } |\boldsymbol{\xi}| > 5/12 \end{cases} ,$$

$$\widehat{\phi}^s(\boldsymbol{\xi}) = \begin{cases} 1 & \text{for } |\boldsymbol{\xi}| < 5/12 \\ \frac{1 + \cos(\frac{120\pi}{11}|\boldsymbol{\xi}| - \frac{50\pi}{11})}{2} & \text{for } 5/12 < |\boldsymbol{\xi}| < 1/2 \\ 0 & \text{for } |\boldsymbol{\xi}| > 1/2 \end{cases} .$$

Define the analysis and synthesis high pass filters by

$$H_i^a(\boldsymbol{\xi}) = \frac{e_{\mathbf{q}_{i-1}}}{2^{d/2}} \begin{cases} 0 & \text{for } |\boldsymbol{\xi}| < 1/8 \\ \frac{1 - \cos(12\pi|\boldsymbol{\xi}| - \frac{3\pi}{2})}{2} & \text{for } 1/8 < |\boldsymbol{\xi}| < 5/24 \\ 1 & \text{for } |\boldsymbol{\xi}| > 5/24 \end{cases} ,$$

$$H_i^s(\boldsymbol{\xi}) = \frac{e_{\mathbf{q}_{i-1}}}{2^{d/2}} \cdot \begin{cases} 0 & \text{for } |\boldsymbol{\xi}| < 1/16 \\ \frac{1 - \cos(16\pi|\boldsymbol{\xi}| - \pi)}{2} & \text{for } 1/16 < |\boldsymbol{\xi}| < 1/8 \\ 1 & \text{for } |\boldsymbol{\xi}| > 1/8 \end{cases} .$$

Finally, the wavelets are defined in the frequency domain as follows,

$$\widehat{\psi}_i^a(2\boldsymbol{\xi}) = \frac{e_{\mathbf{q}_{i-1}}}{2^{d/2}} \begin{cases} 0 & \text{for } |\boldsymbol{\xi}| < 1/8 \\ \frac{1 - \cos(12\pi|\boldsymbol{\xi}| - \frac{3\pi}{2})}{2} & \text{for } 1/8 < |\boldsymbol{\xi}| < 5/24 \\ 1 & \text{for } 5/24 < |\boldsymbol{\xi}| < 1/4 \\ \frac{1 + \cos(6\pi|\boldsymbol{\xi}| - \frac{3\pi}{2})}{2} & \text{for } 1/4 < |\boldsymbol{\xi}| < 5/12 \\ 0 & \text{for } |\boldsymbol{\xi}| > 5/12 \end{cases} ,$$

$$\widehat{\psi}_i^s(2\boldsymbol{\xi}) = \frac{e_{\mathbf{q}_{i-1}}}{2^{d/2}} \begin{cases} 0 & \text{for } |\boldsymbol{\xi}| < 1/16 \\ \frac{1 - \cos(16\pi|\boldsymbol{\xi}| - \pi)}{2} & \text{for } 1/16 < |\boldsymbol{\xi}| < 1/8 \\ 1 & \text{for } 1/8 < |\boldsymbol{\xi}| < 5/12 \\ \frac{1 + \cos(\frac{120\pi}{11}|\boldsymbol{\xi}| - \frac{50\pi}{11})}{2} & \text{for } 5/12 < |\boldsymbol{\xi}| < 1/2 \\ 0 & \text{for } |\boldsymbol{\xi}| > 1/2 \end{cases} .$$

The two previous examples presented typical IMRA-wavelets and refinable functions, but there are other possible cases. Particularly, some of the wavelets constructed by means of Theorem 3.1 in [2] or in [86] can be derived from singly generated IMRAs and thus

shown to be implementable with IMRA-fast wavelet algorithms. The radial wavelets of Epperson and Frazier [42, 43] cannot be derived from singly generated IMRAs although they are very similar to the radial wavelets constructed in the previous two examples. The decompositions of $L^2(\mathbb{R}^d)$ for which these wavelets are used are not at all similar to those induced by $X_{\phi\psi}$ and their associated dual families.

3.3 Fast Isotropic Wavelet Transform

In this section we describe the fast isotropic wavelet transforms associated with the frames produced in Example 3.2.2. We use the abbreviation FIWT for Fast Isotropic Wavelet Transform. This discrete wavelet decomposition and reconstruction algorithm was first presented in [14], for dyadic dilations, in the context of exact reconstruction isotropic filter banks.

As in the classical fast wavelet algorithm (See Section 1.3.3), the goal of the decomposition branch of FIWT is to obtain the approximation (low pass component) and detail (high pass component) at level $j - 1$ given the approximation at level j . The reconstruction branch retrieves the approximation at level j using these high and low pass components at level $j - 1$.

We begin by observing that for the filters defined in Example 3.2.2, the set $\{e_{\mathbf{k}}h^a : \mathbf{k} \in \mathbb{Z}^d\}$ is equal to $\cup_{i=1}^{|\det(A)|} \{e_{2\mathbf{k}}H_i^a : \mathbf{k} \in \mathbb{Z}^d\}$. The latter union would yield $|\det(A)|$ high pass channels with decimation. In our implementation, all these channels are combined into a single undecimated channel using the filter h^a , which is the \mathbb{Z}^d -periodic function defined in (3.29). Accordingly, in our implementation the low pass filtering is followed by decimation determined by A while the high pass filtered signal stays undecimated.

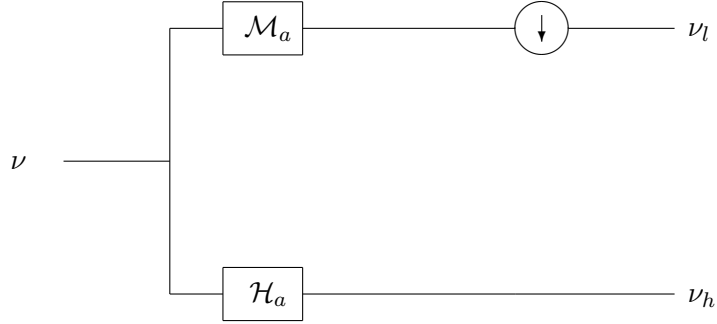


Figure 3.4: Flow diagram for one level of decomposition in FIWT

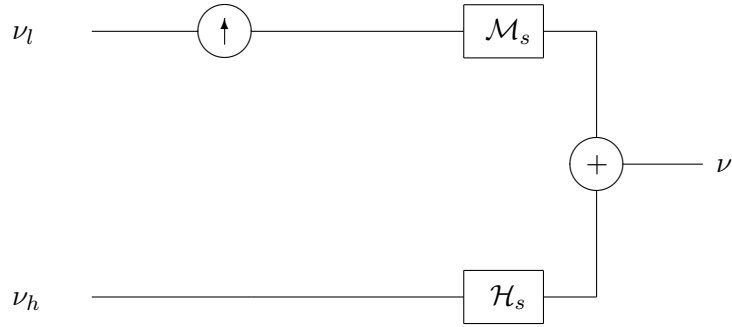


Figure 3.5: Flow diagram for one level of reconstruction in FIWT

The analysis filters produce analysis operators \mathcal{M}_a and \mathcal{H}_a defined via

$$(\mathcal{M}_a \nu)^\wedge = |\det(A)|^{1/2} \widehat{\mathcal{D}}(H_0^a \widehat{\nu}) \quad \text{and} \quad (\mathcal{H}_a \nu)^\wedge = |\det(A)|^{1/2} h^a \widehat{\nu}, \quad \nu \in \ell^2(\mathbb{Z}^d), \quad (3.31)$$

where \mathcal{D} denotes the downsampling operator given by,

$$(\mathcal{D}\nu)^\wedge(\boldsymbol{\xi}) = \frac{1}{|\det(A)|} \sum_{l=1}^{|\det(A)|} \widehat{\nu}(A^{*-1}\boldsymbol{\xi} + \boldsymbol{\gamma}_l),$$

and $\{\boldsymbol{\gamma}_l : l = 1, \dots, |\det(A)|\}$ are the representatives of the quotient group $(A^{*-1}\mathbb{Z}^d)/\mathbb{Z}^d$.

As in the case of analysis high pass filters, the $|\det(A)|$ high pass channels are combined into a single high pass channel with filter h^s . We define the high pass synthesis operator

via $(\mathcal{H}_s\nu)^\wedge = |\det(A)|^{1/2}h_s\widehat{\nu}$ and the low pass synthesis operator, \mathcal{M}_s , is defined via $(\mathcal{M}_s\nu)^\wedge := |\det(A)|^{1/2}H_0^s(\mathcal{U}\nu)^\wedge$, where $\nu \in \ell^2(\mathbb{Z}^d)$ and \mathcal{U} is the upsampling operator defined via,

$$(\mathcal{U}\nu)^\wedge(\boldsymbol{\xi}) = \widehat{\nu}(A^*\boldsymbol{\xi}).$$

These analysis and synthesis operators satisfy an exact reconstruction formula similar to the one obtained for classical fast wavelet algorithms at the end of Section 1.3.3. This formula enables the implementation of FIWT analogous to the classical fast wavelet algorithm.

Proposition 3.3.1 [14][Exact reconstruction formula] *Let \mathcal{M}_s , \mathcal{M}_a , \mathcal{H}_s and \mathcal{H}_a be operators on $\ell^2(\mathbb{Z}^d)$ as defined above, then the following identity holds*

$$I_{\ell^2(\mathbb{Z}^d)} = \mathcal{M}_s\mathcal{M}_a + \mathcal{H}_s\mathcal{H}_a$$

Proof: Let $\nu \in \ell^2(\mathbb{Z}^d)$ then $(\mathcal{H}_s\mathcal{H}_a\nu)^\wedge = |\det(A)|h_s h_a \widehat{\nu} = |\det(A)|^{1/2}h_a\widehat{\nu}$. From the definition of \mathcal{D} and \mathcal{U} , we infer $(\mathcal{U}\mathcal{M}_a\nu)^\wedge$ is a $A^{-1}\mathbb{Z}^d$ -periodic function. Since m_s and m_a vanish outside the d -torus $A^{*-1}\mathbb{T}^d$ and the ball $A^{*-1}\mathbb{B}_1$ respectively, we obtain $(\mathcal{M}_s\mathcal{M}_a\nu)^\wedge = m_s m_a \widehat{\nu} = m_a \widehat{\nu}$.

Now, observe that $m_a + |\det(A)|^{1/2}h_a = 1$, which verifies the exactness of the reconstruction. \square

Remark 3.3.2 The exact reconstruction formula holds even if we use $\frac{1}{|\det(A)|^{1/2}}I_{\ell^2(\mathbb{Z}^d)}$ instead of \mathcal{H}_s . Hence, for the implementation, we do not apply the synthesis high pass filter. Instead, we just multiply by the output of the analysis high pass operator by the factor $\frac{1}{|\det(A)|^{1/2}}$. We mention this fact here because if we use $\frac{1}{|\det(A)|^{1/2}}I_{\ell^2(\mathbb{Z}^d)}$ instead of \mathcal{H}_s as the high pass synthesis operator then the family, $X_{\phi\psi}^s$, is not Bessel. The latter is

required for theoretical consistency as it enables Theorem 3.1.10, which gives that $X_{\phi\psi}^a$ and $X_{\phi\psi}^s$ are dual frames for $L^2(\mathbb{R}^d)$.

Remark 3.3.3 In contrast to the usual tensor-product constructions both filters (low pass and high pass) are isotropic. The analysis and synthesis scaling functions are C^∞ -smooth in the wavenumber domain by definition. This, in turn, implies that the wavelets are also C^∞ -smooth in the wavenumber domain. Thus, the radial scaling functions and their associated wavelets have rapid decay in the spatial domain.

The exact reconstruction formula holds for any filter bank satisfying Equation (3.9), for digital signals ν such that $\widehat{\nu}$ is supported on $\sigma(V_0^a) \cap \sigma(V_0^s)$. We conclude this chapter by proving this version of the exact reconstruction formula.

Recall that for a filter bank $\{H_i, i = 0, 1, \dots, m\}$ the modulation matrix \mathbf{H} is defined by

$$\mathbf{H} = \begin{pmatrix} H_0 & H_1 & \dots & H_m \\ T_{\mathbf{q}_1} H_0 & T_{\mathbf{q}_1} H_1 & \dots & T_{\mathbf{q}_1} H_m \\ \vdots & \vdots & \ddots & \vdots \\ T_{\mathbf{q}_{n-1}} H_0 & T_{\mathbf{q}_{n-1}} H_1 & \dots & T_{\mathbf{q}_{n-1}} H_m \end{pmatrix},$$

where $n = |\det(A^*)|$ and $\mathbf{q}_l : l = 0, 1, 2, \dots, n-1$ are the representatives of the quotient group $(A^{*-1}\mathbb{Z}^d)/\mathbb{Z}^d$. If \mathbf{H}_a is the modulation matrix corresponding to the analysis filters, and \mathbf{H}_s is the modulation matrix corresponding to the synthesis filters, then Equation (3.9)

says that

$$\mathbf{H}_s \mathbf{H}_a^* = \begin{pmatrix} \chi_{\sigma(V_0^a) \cap \sigma(V_0^s)} & 0 & \cdots & 0 \\ 0 & T_{\mathbf{q}_1} \chi_{\sigma(V_0^a) \cap \sigma(V_0^s)} & \cdots & 0 \\ \vdots & \vdots & \ddots & \vdots \\ 0 & 0 & \cdots & T_{\mathbf{q}_{n-1}} \chi_{\sigma(V_0^a) \cap \sigma(V_0^s)} \end{pmatrix}.$$

For a given digital signal $\nu \in \ell^2(\mathbb{Z}^d)$ let $\boldsymbol{\omega}$ denote the following vector:

$$\boldsymbol{\omega} = (\widehat{\nu}, T_{\mathbf{q}_1} \widehat{\nu}, \dots, T_{\mathbf{q}_{n-1}} \widehat{\nu})^T.$$

Observe that,

$$\mathbf{H}_a^* \boldsymbol{\omega} = \begin{pmatrix} \sum_{l=0}^{n-1} T_{\mathbf{q}_l} (\overline{H_0^a} \widehat{\nu}) \\ \sum_{l=0}^{n-1} T_{\mathbf{q}_l} (\overline{H_1^a} \widehat{\nu}) \\ \vdots \\ \sum_{l=0}^{n-1} T_{\mathbf{q}_l} (\overline{H_m^a} \widehat{\nu}) \end{pmatrix} = |\det(A)| \begin{pmatrix} \widehat{\mathcal{U}} \widehat{\mathcal{D}} (\overline{H_0^a} \widehat{\nu}) \\ \widehat{\mathcal{U}} \widehat{\mathcal{D}} (\overline{H_1^a} \widehat{\nu}) \\ \vdots \\ \widehat{\mathcal{U}} \widehat{\mathcal{D}} (\overline{H_m^a} \widehat{\nu}) \end{pmatrix}.$$

Now, assuming that $\mathbf{H}_s \mathbf{H}_a^* = \mathbf{I}$, we get

$$\sum_{i=0}^m \mathcal{H}_i^s \mathcal{H}_i^a = I_{\ell^2(\mathbb{Z}^d)}, \quad (3.32)$$

where, for each i , the analysis operator, \mathcal{H}_i^a , is defined via $\widehat{\mathcal{H}}_i^a = |\det(A)|^{1/2} \widehat{\mathcal{D}}(\overline{H_i^a} \widehat{\nu})$, and the synthesis operator, \mathcal{H}_i^s , is defined via $\widehat{\mathcal{H}}_i^s = |\det(A)|^{1/2} H_i^s (\mathcal{U}\nu)^\wedge$. Equation (3.32) gives an exact reconstruction formula for filters satisfying $\mathbf{H}_s \mathbf{H}_a^* = \mathbf{I}$. This condition is slightly stronger than the condition in Equation (3.9). If the filters satisfy the weaker condition (3.9) then we get

$$\sum_{i=0}^m (\mathcal{H}_i^s \mathcal{H}_i^a \nu)^\wedge = \chi_{\sigma(V_0^a) \cap \sigma(V_0^s)} \widehat{\nu}. \quad (3.33)$$

Therefore, in this case, we get exact reconstruction for a digital signal, only if, its Fourier transform is supported on $\sigma(V_0^a) \cap \sigma(V_0^s)$.

3.3. FAST ISOTROPIC WAVELET TRANSFORM

Since the definition of filters on the complement of $\sigma(V_0^a) \cap \sigma(V_0^s)$ has no effect on Theorem 3.1.10, we can design the filters to satisfy the stronger condition above and thus have exact reconstruction at every step of the pyramid algorithm. This is the case with the filters designed in Examples 3.2.2 and 3.2.1.

Chapter 4

Explicit Schemes in Seismic Migration and Isotropic Multiscale Representations

Migration is a seismic imaging technique used by the oil industry to image the interior of the Earth for the purpose of oil prospecting. A detailed description of seismic migration is beyond the scope of this thesis. In Section 4.1, we give a very brief overview of what is called wave equation migration and we arrive at the so-called Phase-shift propagator operator which is used to obtain the image of the interior by downward propagating acoustic waves recorded on the surface. Our focus in this chapter is the efficient discretization of this operator in terms of pairs of dual frames arising from a Isotropic Multiresolution Analysis (IMRA) described in Section 3.2. Seismic migration is a delicate inverse problem. To solve it we work on a 3 or 4 dimensional time-frequency space, $\mathbb{R} \times \mathbb{R}^2$ or $\mathbb{R} \times \mathbb{R}^3$ respectively. The underlying spaces are $L^2(\mathbb{R}) \otimes L^2(\mathbb{R}^d)$ with $d = 2, 3$. One of the main tools is the Fourier transform. We actually use two such transforms; the Fourier transform on $L^2(\mathbb{R})$ and the Fourier transform on $L^2(\mathbb{R}^d)$. We refer to \mathbb{R} as the time-domain and to \mathbb{R}^d as the spatial

domain. We refer to the dual group of \mathbb{R}^2 or \mathbb{R}^3 as the wavenumber domain to distinguish it from the dual group of \mathbb{R} , which we refer to as the frequency domain. Wavenumbers, i.e. elements of the dual group of \mathbb{R}^d , are denoted by ξ 's versus elements of the dual group of \mathbb{R} , the time domain, denoted by ω 's.

The phase shift operator is a multiplicative operator in the wavenumber domain. It is therefore, a convolution in the space domain. If the velocity of sound waves is not assumed to be constant beneath the surface then this becomes a spatially varying convolution operator. The recursive application of this convolution operator is referred to as an explicit scheme. Explicit schemes for wave equation migration are attractive because they handle lateral variations in velocity better than implicit schemes such as Fourier finite differences [95]. However, the computational cost of explicit schemes is always a matter of concern due to the enormity of the data sets. In Section 4.2 we show that the IMRA-based wave equation migration (henceforth referred to as migration) reduces to a standard explicit scheme when applied to a signal at the zero resolution level. The multiscale structure of IMRA, offers the possibility of reducing the computational cost. This can be compared to the work of Margrave and his collaborators [81], who describe a sub-sampling scheme using the frequency domain.

4.1 Explicit Schemes for Wave Equation Migration

In this section we give a brief overview of explicit wave equation migration. In a typical prospecting experiment, sound waves generated by small explosions travel from a source on the surface into the ground and are reflected back by the complex structures beneath the surface which we refer to as reflectors. These reflectors represent the surfaces where the stratigraphy changes. The reflected waves are recorded on receivers called geophones

(or hydrophones in the case of offshore exploration). If we assume that the source and the receiver are located at the same point then the data (recorded pressure wave on the receivers) is said to have zero offset. For zero-offset data the incident and reflected waves travel along the same path. A simplifying assumption is to disregard the incident wave and assume that the reflectors beneath the surface explode at time $t = 0$, to produce the waves that travel to the surface at half of the actual velocity and are recorded on the receivers. With this assumption the propagation distance (reflector to surface) is half the actual propagation distance (surface to reflector and back to the surface). Since both the velocity and propagation distance are half of their actual values, the pressure wave created by the exploding reflectors arrives at the same time as the original reflected wave.

Migration refers to the process of obtaining the image of the reflectors using the pressure wave recorded on the surface. The pressure wave at x, y horizontal coordinates, depth z and time t is denoted by $f(x, y, z, t)$. We begin by taking the Fourier transform of f with respect to the time variable. This new function with variables x, y, z and ω is called the ‘wavefield’ for frequency, ω . If the velocity varies only with depth z , we solve the following differential equation proposed by Claerbout (Section 1.5 in [31]), who derives it by applying principles of classical optics;

$$\frac{\partial \hat{f}}{\partial z}(k_x, k_y, z, \omega) = \left(2\pi i \sqrt{\frac{\omega^2}{c(z)^2} - k_x^2 - k_y^2} \right) \hat{f}(k_x, k_y, z, \omega), \quad (4.1)$$

where $c(z)$ denotes the velocity, \hat{f} denotes the wavefield in the wavenumber domain (with respect to x and y variables), and k_x and k_y denote the wavenumbers. We refer to (4.1) as the one-way wave equation because it represents the upward going waves when the reflectors ‘explode’ in the subsurface. The solution to (4.1) is given by:

$$\hat{f}(z; k_x, k_y, \omega) = \exp \left(\int_{z_0}^z 2\pi i \sqrt{\frac{\omega^2}{c(z)^2} - k_x^2 - k_y^2} dz \right) \hat{f}(z_0; k_x, k_y, \omega). \quad (4.2)$$

For a small depth step Δz , c is practically constant. Hence, for practical purposes we allow

$$\widehat{f}(z + \Delta z; k_x, k_y, \omega) = e^{2\pi i \Delta z \sqrt{\frac{\omega^2}{c(z)^2} - k_x^2 - k_y^2}} \widehat{f}(z, k_x, k_y; \omega). \quad (4.3)$$

In conclusion, the wavefield at $z + \Delta z$ is calculated from the wavefield at z via a multiplication in the wavenumber domain. The multiplication by $e^{2\pi i \Delta z \sqrt{\frac{\omega^2}{c(z)^2} - k_x^2 - k_y^2}}$ in the previous equation defines a multiplicative operator referred to as the Phase-shift propagator operator. This is a convolution operator in the spatial domain which we denote by \mathcal{P} . We recursively obtain the wavefield for all z using \mathcal{P} . Integrating numerically over all frequencies ω , we obtain the pressure wave $f(x, y, z, 0)$ for all z at time $t = 0$ which depicts the ‘exploding’ reflectors. This procedure is termed as *post stack migration*, because, in order to apply the ‘exploding reflectors’ concept, the data has to be stacked into zero offset sections. The interested reader can find the details of the stacking process and the derivation of the one-way wave equation in [31]. If the velocity varies laterally, the operator \mathcal{P} is replaced by a ‘spatially varying convolution’ operator. We clarify this kind of convolution below. But before doing this we want to mention that in the geophysical literature, the migration process described above, is discretized by sampling the wave-field on a regular grid and by approximating $e^{\pm 2\pi i \Delta z \sqrt{\frac{\omega^2}{c^2} - k_x^2 - k_y^2}}$ (the symbol of the operator, \mathcal{P} in the wavenumber domain) with a trigonometric polynomial. This approximation of \mathcal{P} is carried out for every point of the grid on which the data are collected. The collection of all these approximations of \mathcal{P} is referred to as a propagator matrix. Propagator matrices are applied recursively on the data to calculate the propagating wavefield for all z .

Our approach is formal compared to various ad-hoc discretizations of the phase-shift operator. It also leads to a sparser propagator matrix in certain cases.

Let us now return to \mathcal{P} . For a fixed ω , we denote the wavefield at (\mathbf{x}, z, ω) by $f_z(\mathbf{x})$,

where $\mathbf{x} = (x, y)$. The operator \mathcal{P} acts via a multiplication in the wavenumber domain,

$$\widehat{f}_{z+\Delta z}(\boldsymbol{\xi}) = \widehat{(\mathcal{P}f_z)}(\boldsymbol{\xi}) = e^{2\pi i\Delta z\sqrt{\frac{\omega^2}{c^2}-|\boldsymbol{\xi}|^2}}\widehat{f}_z(\boldsymbol{\xi}),$$

where $\boldsymbol{\xi} = (k_x, k_y)$. Thus,

$$\mathcal{P}f_z(\mathbf{x}) = \int_{\mathbb{R}^2} e^{2\pi i\langle \mathbf{x}, \boldsymbol{\xi} \rangle} e^{2\pi i\Delta z\sqrt{\frac{\omega^2}{c^2}-|\boldsymbol{\xi}|^2}}\widehat{f}_z(\boldsymbol{\xi})d\boldsymbol{\xi}. \quad (4.4)$$

To make \mathcal{P} bounded, we need to assume that f_z is appropriately band-limited and is in $L^2(\mathbb{R}^2)$. All this analysis works under the assumption that c is laterally constant in the depth slice $[z, z + \Delta z]$. If c varies with $\mathbf{x} \in \mathbb{R}^2$ then (4.4) is no longer valid. What is still valid is to assume that \mathcal{P} is linear and bounded. With these assumptions and for a ϕ that is a continuous function with compact support or rapidly decaying at infinity, we can approximate $\langle \mathcal{P}f_z, \phi \rangle$ by

$$\int_{\mathbb{R}^2} \int_{\mathbb{R}^2} e^{2\pi i\langle \mathbf{x}, \boldsymbol{\xi} \rangle} e^{2\pi i\Delta z\sqrt{\frac{\omega^2}{c^2}-|\boldsymbol{\xi}|^2}}\widehat{f}_z(\boldsymbol{\xi})\overline{\phi(\mathbf{x})}d\boldsymbol{\xi}d\mathbf{x}, \quad (4.5)$$

where c is the mean velocity in the support of ϕ . The previous equation allows us to consider situations that are realistic in seismic imaging, where the velocity has lateral variation. Since ϕ is well localized, we can assume that c is practically constant. This discussion implies that a discretization of \mathcal{P} , discussed in Section 4.2.1, must be implemented with a spatially varying convolution.

4.2 The IMRA-based Numerical Solution of the One-way Acoustic Wave Equation

To carry out the discretization of \mathcal{P} we employ the dual pair of frames, $X_{\phi\psi}^a$ and $X_{\phi\psi}^s$, obtained in Example 3.2.2. Recall that the families $X_{\phi\psi}^a := X_{\phi^a\psi^a}$ and $X_{\phi\psi}^s := X_{\phi^a\psi^a}$ are

defined via

$$X_{\phi\psi} := \left\{ D_A^j T_{\mathbf{k}} \psi_i : j \in \mathbb{N} \cup \{0\}, \mathbf{k} \in \mathbb{Z}^d, i = 1, \dots, m \right\} \cup \left\{ T_{\mathbf{k}} \phi : \mathbf{k} \in \mathbb{Z}^d \right\}.$$

In the rest of this chapter we drop the subscript A from the notation for the dilation operator but we keep in mind that it is defined with respect to a radially expansive matrix of the form $A = aR$, where $a > 1$ and $R \in SO(2)$.

For a fixed depth, z , and a frequency, ω , the samples of the wavefield, f on \mathbb{Z}^2 , are assumed to be equal to the coefficients $\langle f, T_{\mathbf{k}} \phi^a \rangle$ where ϕ^a is the two-dimensional IMRA analysis scaling function which is radial and bandlimited to $B(0, ab_1) \subset \mathbb{T}^2$. This is based on the assumption that the wavefield is band-limited in the ball, $\mathbb{B}_2 := B(0, ab_2)$, where $\widehat{\phi^a}$ is equal to 1. Indeed, for all such f , we have:

$$\begin{aligned} f(\mathbf{k}) &= \int_{\mathbb{R}^2} \widehat{f}(\boldsymbol{\xi}) e^{2\pi i \langle \mathbf{k}, \boldsymbol{\xi} \rangle} d\boldsymbol{\xi} = \int_{\mathbb{R}^2} \widehat{f}(\boldsymbol{\xi}) \widehat{\phi^a}(\boldsymbol{\xi}) e^{2\pi i \langle \mathbf{k}, \boldsymbol{\xi} \rangle} d\boldsymbol{\xi} \\ &= \left\langle \widehat{f}, \widehat{\phi^a} e_{\mathbf{k}} \right\rangle = \langle f, T_{\mathbf{k}} \phi^a \rangle \quad \text{for all } \mathbf{k} \in \mathbb{Z}^2. \end{aligned} \quad (4.6)$$

The second equality is true because $\widehat{\phi^a}$ is equal to 1 on the support of \widehat{f} and the last equality follows from Plancherel's theorem. Now, if the signal (function) has a higher band limit, then we sample the signal on a finer grid and the samples are then the coefficients $\langle f, D^j T_{\mathbf{k}} \phi^a \rangle$ for an appropriate scale $j > 0$.

Recall that the families $X_{\phi\psi}^a$ and $X_{\phi\psi}^s$ form a pair of dual frames for $L^2(\mathbb{R}^2)$. This implies that $D^{j_0} X_{\phi\psi}^a$ and $D^{j_0} X_{\phi\psi}^s$ form a pair of dual frames for $L^2(\mathbb{R}^2)$ because D^{j_0} is a unitary operator for all $j_0 \in \mathbb{Z}$. Hence, every $f \in L^2(\mathbb{R}^2)$ can be written as:

$$f = \sum_{\mathbf{k} \in \mathbb{Z}^2} \langle f, D^{j_0} T_{\mathbf{k}} \phi^a \rangle D^{j_0} T_{\mathbf{k}} \phi^s + \sum_{j=j_0}^{\infty} \sum_{i=1}^{|\det(A)|} \sum_{\mathbf{k} \in \mathbb{Z}^2} \langle f, D^j T_{\mathbf{k}} \psi_i^a \rangle D^j T_{\mathbf{k}} \psi_i^s. \quad (4.7)$$

In the special case that f is band limited to the disk of radius $a^{j_0+1}b_2$ then $\langle f, D^j T_{\mathbf{k}} \psi_i^a \rangle = 0$ for all $j \geq j_0, i = 1, \dots, |\det(A)|, \mathbf{k} \in \mathbb{Z}^2$, and $\langle f, D^{j_0} T_{\mathbf{k}} \phi^a \rangle = f(A^{-j_0} \mathbf{k})$ for all $\mathbf{k} \in \mathbb{Z}^2$.

Hence, the representation of f in (4.7) reduces to

$$f = \sum_{\mathbf{k} \in \mathbb{Z}^2} f(A^{-j_0} \mathbf{k}) D^{j_0} T_{\mathbf{k}} \phi^s. \quad (4.8)$$

We refer to this expression as the representation at the j_0 resolution level. In practice, the resolution level is not quantified. All data sets are delivered on a sampling grid. Typically, this grid delivers the data sampled at the proper rate or at a somewhat higher one. Thus, we always adopt the convention that the wavefield, f , lies in the zero-resolution space, i.e. f can be expressed by means of (4.8) with $j_0 = 0$.

4.2.1 Discretization of the Propagator

Recall that \mathcal{P} denotes the propagator operator and k_0 the ratio $\frac{\omega^2}{c_0^2}$, where c_0 is the velocity which is assumed to be constant for the moment. The discretization of \mathcal{P} turns out to be a Toeplitz matrix in this case. In the wavenumber domain, \mathcal{P} acts via multiplication with the symbol of the operator,

$$\widehat{\mathcal{P}(f)}(\boldsymbol{\xi}) = e^{2\pi i \Delta z \sqrt{k_0^2 - |\boldsymbol{\xi}|^2}} \widehat{f}(\boldsymbol{\xi}) \quad \boldsymbol{\xi} \in \mathbb{R}^2.$$

Applying \mathcal{P} to both sides of the frame decomposition (4.7) we obtain a discretization of \mathcal{P} . First,

$$\mathcal{P}(f) = \sum_{\mathbf{l} \in \mathbb{Z}^2} \langle \mathcal{P}(f), T_{\mathbf{l}} \phi^a \rangle T_{\mathbf{l}} \phi^s + \sum_{j=0}^{\infty} \sum_{i=1}^{|\det(A)|} \sum_{\mathbf{l} \in \mathbb{Z}^2} \langle \mathcal{P}(f), D^j T_{\mathbf{l}} \psi_i^a \rangle D^j T_{\mathbf{l}} \psi_i^s. \quad (4.9)$$

Before we proceed, note that the support of a function in the wavenumber domain is invariant under the action of the propagator, \mathcal{P} because \mathcal{P} is multiplicative in this domain. Hence, for a function, f bandlimited to \mathbb{B}_2 , $\mathcal{P}(f)$ is also bandlimited to \mathbb{B}_2 . Now, from (4.6) and (4.8), such a function, f , can be expressed in terms of the integer translates of

ϕ^s :

$$f = \sum_{\mathbf{k} \in \mathbb{Z}^2} f(\mathbf{k}) T_{\mathbf{k}} \phi^s. \quad (4.10)$$

Since, the same is also true for $\mathcal{P}(f)$, we have

$$\mathcal{P}(f) = \sum_{\mathbf{l} \in \mathbb{Z}^2} \mathcal{P}(f)(\mathbf{l}) T_{\mathbf{l}} \phi^s,$$

where,

$$\mathcal{P}(f)(\mathbf{l}) = \langle \mathcal{P}(f), T_{\mathbf{l}} \phi^a \rangle = \left\langle \mathcal{P} \left(\sum_{\mathbf{k} \in \mathbb{Z}^2} f(\mathbf{k}) T_{\mathbf{k}} \phi^s \right), T_{\mathbf{l}} \phi^a \right\rangle = \sum_{\mathbf{k} \in \mathbb{Z}^2} f(\mathbf{k}) \langle \mathcal{P}(T_{\mathbf{k}} \phi^s), T_{\mathbf{l}} \phi^a \rangle.$$

Thus, the vector of samples of the wavefield at $z + \Delta z$ is given by multiplying the vector of samples of the wavefield at z with a matrix which we denote by $\mathcal{P}^{(0)}$. We refer to this matrix as the propagator matrix for V_0 , given by

$$\mathcal{P}_{\mathbf{l}, \mathbf{k}}^{(0)} = \langle \mathcal{P} T_{\mathbf{k}} \phi^s, T_{\mathbf{l}} \phi^a \rangle = \left\langle \widehat{\mathcal{P}} e_{\mathbf{k}} \widehat{\phi}^s, e_{\mathbf{l}} \widehat{\phi}^a \right\rangle = \int_{\mathbb{R}^2} \widehat{\phi}^a(\boldsymbol{\xi}) e^{i\Delta z \sqrt{k_0^2 - |\boldsymbol{\xi}|^2}} e^{-2\pi i \langle \mathbf{k} - \mathbf{l}, \boldsymbol{\xi} \rangle} d\boldsymbol{\xi}.$$

The last equality follows from the fact $\widehat{\phi}^s = 1$ on the support of $\widehat{\phi}^a$. Now, since $\widehat{\phi}^a$ is supported in $\mathbb{B}_1 \subset \mathbb{T}^2$, the \mathbf{l}, \mathbf{k} -entry of $\mathcal{P}^{(0)}$ is the $(\mathbf{k} - \mathbf{l})$ -th Fourier coefficient of $\widehat{\phi}^a e^{i\Delta z \sqrt{k_0^2 - |\boldsymbol{\xi}|^2}}$. Observe that $\mathcal{P}^{(0)}$ is a Toeplitz matrix. Hence, the operator is applied on the discretized signal by convolution with the first row of this matrix.

For a fixed value of the ratio $k_0 = \frac{\omega}{c_0}$, we refer to these Fourier coefficients as the **propagator filter** corresponding to k_0 . Note that for the constant velocity model, we required only one propagator filter for each ω . Now, if the velocity varies laterally, for each ω , we need more than one propagator filter to construct the propagator matrix $\mathcal{P}^{(0)}$. In that case, we construct a ‘table’ driven migration scheme, meaning that we calculate the propagator filters for a pre-determined set of values of the ratio $k_0 = \frac{\omega}{c_0}$ and store them in a ‘table’. The values of k_0 range from 0 to $\frac{\omega_{max}}{c_{min}}$, where ω_{max} is the maximum temporal frequency of the data and c_{min} is the minimum velocity for the given velocity model.

Recall, for the variable velocity model, we approximate \mathcal{P} via (4.5):

$$\langle \mathcal{P} f_z, \phi \rangle = \int_{\mathbb{R}^2} \int_{\mathbb{R}^2} e^{2\pi i \langle \mathbf{x}, \boldsymbol{\xi} \rangle} e^{2\pi i \Delta z \sqrt{\frac{\omega^2}{c(\mathbf{x})^2} - |\boldsymbol{\xi}|^2}} \widehat{f}_z(\boldsymbol{\xi}) \overline{\phi(\mathbf{x})} d\boldsymbol{\xi} d\mathbf{x},$$

where ϕ is compactly supported or rapidly decaying in the spatial domain and continuous.

The equation is still valid if $\int_{\mathbb{R}^2} |\phi(\mathbf{x})|^2 (1 + |\mathbf{x}|)^{2+\delta} dx < +\infty$ for $\delta > 0$. Hence,

$$\mathcal{P}_{\mathbf{l}, \mathbf{k}}^{(0)} = \langle \mathcal{P}(T_{\mathbf{k}} \phi^s), T_{\mathbf{l}} \phi^a \rangle = \int_{\mathbb{R}^2} \int_{\mathbb{R}^2} e^{2\pi i \langle \mathbf{x}, \boldsymbol{\xi} \rangle} e^{2\pi i \Delta z \sqrt{\frac{\omega^2}{c(\mathbf{x})^2} - |\boldsymbol{\xi}|^2}} e_{\mathbf{k}}(\boldsymbol{\xi}) \widehat{\phi^s}(\boldsymbol{\xi}) \overline{T_{\mathbf{l}} \phi^a(\mathbf{x})} d\boldsymbol{\xi} d\mathbf{x}.$$

Applying the Fubini-Tonelli Theorem, we can change the order of integration. Now, replace $c(\mathbf{x})$ by $c_{\mathbf{l}}$, the \mathbf{l} -th sample of the velocity model because $T_{\mathbf{l}} \phi^a$ is well localized in the space domain since $\widehat{\phi^a}$ is C^∞ -smooth (see Remark 3.3.3). This yields

$$\mathcal{P}_{\mathbf{l}, \mathbf{k}}^{(0)} = \int_{\mathbb{R}^2} e^{2\pi i \Delta z \sqrt{\frac{\omega^2}{c_{\mathbf{l}}^2} - |\boldsymbol{\xi}|^2}} e_{\mathbf{k}}(\boldsymbol{\xi}) \widehat{\phi^s}(\boldsymbol{\xi}) \overline{e_{\mathbf{l}}(\boldsymbol{\xi}) \widehat{\phi^a}(\boldsymbol{\xi})} d\boldsymbol{\xi}. \quad (4.11)$$

Hence, at a given depth step, the \mathbf{l} -th row of the matrix $\mathcal{P}_{\mathbf{l}, \mathbf{k}}^{(0)}$ is the propagator filter corresponding to the ratio $\frac{\omega}{c_{\mathbf{l}}}$. Hence, the \mathbf{l} -th row of the matrix can be obtained from the pre-calculated table by picking up the propagator filter corresponding to k_0 which is closest to the ratio $\frac{\omega}{c_{\mathbf{l}}}$.

Notice that $\widehat{\phi^a}$ acts like a smoothing function to obtain a trigonometric polynomial approximation of the phase shift operator. The matrix, $\mathcal{P}^{(0)}$, is practically a spatially varying convolution. This is because for the constant velocity case, we saw it was a Toeplitz matrix (i.e. each row is obtained by right shifting the previous row) and hence, a convolution. Now that the filter changes with every point on the grid (i.e. \mathbf{l} -th row depends on $c_{\mathbf{l}}$), this induces what is referred to as a spatially varying convolution. As pointed out in the introduction, the discretization of \mathcal{P} we obtained here, at the zero resolution level, is what geophysicists call a standard explicit scheme. In the geophysics literature, this kind of analysis is not carried out. Instead, the entries of the propagator matrix are calculated via (4.11), where instead of $\widehat{\phi^a} \widehat{\phi^s} = \widehat{\phi^a}$, an arbitrary smoothing filter is used.

However, the multilevel structure of the IMRA can be utilized to reduce the computational cost as we argue in the following subsections.

4.2.2 Decomposing the Signal and the Propagator Matrix using the Fast Isotropic Wavelet Algorithm

We can decompose a wavefield belonging to V_0 into a low pass component and a high pass component using the two dimensional version of the fast wavelet algorithm described in Section 3.3. Now, the representation of the function becomes

$$f = \underbrace{\sum_{\mathbf{k} \in \mathbb{Z}^2} \langle f, D^{-1}T_{\mathbf{k}}\phi^a \rangle D^{-1}T_{\mathbf{k}}\phi^s}_{\text{low pass component}} + \underbrace{\sum_{i=1}^{|\det(A)|} \sum_{\mathbf{k} \in \mathbb{Z}^2} \langle f, D^{-1}T_{\mathbf{k}}\psi_i^a \rangle D^{-1}T_{\mathbf{k}}\psi_i^s}_{\text{high pass component}}.$$

Now, from the definition of ψ_i^a and ψ_i^s we infer, $D^{-1}T_{\mathbf{k}'}\psi_i^a = T_{\mathbf{k}}\psi_1^a$ and $D^{-1}T_{\mathbf{k}'}\psi_i^s = T_{\mathbf{k}}\psi_1^s$ where $\mathbf{k} = A\mathbf{k}' + \mathbf{p}_i$ and \mathbf{p}_i are the representatives of the quotient group $\mathbb{Z}^2/(A\mathbb{Z}^2)$. For instance, if A is the dyadic dilation matrix, $2I_{\mathbb{R}^2}$, then $\mathbf{p}_1 = (0, 0)$, $\mathbf{p}_2 = (1, 0)$, $\mathbf{p}_3 = (0, 1)$ and, $\mathbf{p}_4 = (1, 1)$. We therefore have the following representation of the function f :

$$f = \underbrace{\sum_{\mathbf{k} \in \mathbb{Z}^2} \langle f, T_{A\mathbf{k}}D^{-1}\phi^a \rangle T_{A\mathbf{k}}D^{-1}\phi^s}_{\text{low pass component}} + \underbrace{\sum_{\mathbf{k} \in \mathbb{Z}^2} \langle f, T_{\mathbf{k}}D^{-1}\psi_1^a \rangle T_{\mathbf{k}}D^{-1}\psi_1^s}_{\text{high pass component}}.$$

For this representation, the propagator matrix $\mathcal{P}^{(0)}$ is decomposed into the following:

$$\begin{pmatrix} \mathcal{P}^{(-1)} & \mathfrak{F}^{(-1)} \\ \mathfrak{T}^{(-1)} & \mathcal{Q}^{(-1)} \end{pmatrix}, \quad (4.12)$$

where

$$\begin{aligned}\mathcal{P}_{\mathbf{l},\mathbf{k}}^{(-1)} &= \langle \mathcal{P}T_{A\mathbf{k}}D^{-1}\phi^s, T_{A\mathbf{l}}D^{-1}\phi^a \rangle, \\ \mathfrak{F}_{\mathbf{l},\mathbf{k}}^{(-1)} &= \langle \mathcal{P}T_{A\mathbf{k}}D^{-1}\phi^s, T_{\mathbf{l}}D^{-1}\psi_1^a \rangle, \\ \mathfrak{Z}_{\mathbf{l},\mathbf{k}}^{(-1)} &= \langle \mathcal{P}T_{\mathbf{k}}D^{-1}\psi_1^s, T_{A\mathbf{l}}D^{-1}\phi^a \rangle, \\ \mathcal{Q}_{\mathbf{l},\mathbf{k}}^{(-1)} &= \langle \mathcal{P}T_{\mathbf{k}}D^{-1}\psi_1^s, T_{\mathbf{l}}D^{-1}\psi_1^a \rangle.\end{aligned}$$

We argue that we can ignore $\mathfrak{F}^{(-1)}$ and $\mathfrak{Z}^{(-1)}$ to obtain the following block diagonal propagator matrix,

$$\begin{pmatrix} \mathcal{P}^{(-1)} & 0 \\ 0 & \mathcal{Q}^{(-1)} \end{pmatrix}. \quad (4.13)$$

We now describe the process of obtaining each of the components, $\mathcal{P}^{(-1)}$, $\mathfrak{F}^{(-1)}$, $\mathfrak{Z}^{(-1)}$ and $\mathcal{Q}^{(-1)}$, for the constant velocity case. The generalization to the variable velocity model is exactly the same as for $\mathcal{P}^{(0)}$. To obtain the propagators for V_{-1} and W_{-1} , recall the two scale relations:

$$\widehat{\phi^a}(A^*.) = H_0^a \widehat{\phi^a}, \quad (4.14)$$

$$\widehat{\phi^s}(A^*.) = H_0^s \widehat{\phi^s}. \quad (4.15)$$

Applying the inverse Fourier transform followed by a translation, $T_{A\mathbf{k}}$, to (4.14) and (4.15) yields,

$$D^{-1}T_{\mathbf{k}}\phi^a = \sum_{\mathbf{m} \in \mathbb{Z}^2} \alpha_{\mathbf{m}}^a T_{A\mathbf{k}-\mathbf{m}}\phi^a,$$

$$D^{-1}T_{\mathbf{k}}\phi^s = \sum_{\mathbf{m} \in \mathbb{Z}^2} \alpha_{\mathbf{m}}^s T_{A\mathbf{k}-\mathbf{m}}\phi^s,$$

where, $\{\alpha_{\mathbf{m}}^a\}_{\mathbf{m} \in \mathbb{Z}^2}$ and $\{\alpha_{\mathbf{m}}^s\}_{\mathbf{m} \in \mathbb{Z}^2}$ are the coefficients of the Fourier series of $|\det(A)|^{1/2}m_0^a$ and $|\det(A)|^{1/2}m_0^s$ respectively. Using this, the matrix $\mathcal{P}^{(-1)}$ is obtained by the convolution

4.2. IMRA-BASED SOLUTION OF THE ONE-WAY ACOUSTIC WAVE EQUATION

of $\mathcal{P}^{(0)}$ with the tensor product matrix $S = (\overline{\alpha^a} \alpha_m^s)_{i, \mathbf{m}}$ followed by downsampling as follows:

$$\begin{aligned}
 \mathcal{P}_{\mathbf{l}, \mathbf{k}}^{(j-1)} &= \langle \mathcal{P}(D^{j-1} T_{\mathbf{k}} \phi^s), D^{j-1} T_{\mathbf{l}} \phi^a \rangle \\
 &= \left\langle \mathcal{P} \left(\sum_{\mathbf{m} \in \mathbb{Z}^2} \alpha_{\mathbf{m}}^s D^j T_{A\mathbf{k}-\mathbf{m}} \phi^s \right), \sum_{\mathbf{i} \in \mathbb{Z}^2} \alpha_{\mathbf{i}}^a D^j T_{A\mathbf{l}-\mathbf{i}} \phi^a \right\rangle \\
 &= \sum_{i, \mathbf{m}} \overline{\alpha^a} \alpha_{\mathbf{m}}^s \langle \mathcal{P} D^j T_{A\mathbf{k}-\mathbf{m}} \phi^s, D^j T_{A\mathbf{l}-\mathbf{i}} \phi^a \rangle \\
 &= \sum_{i, \mathbf{m}} \overline{\alpha^a} \alpha_{\mathbf{m}}^s \mathcal{P}_{A\mathbf{l}-\mathbf{i}, A\mathbf{k}-\mathbf{m}}^{(j)}.
 \end{aligned}$$

Similar expressions can be derived for $\mathfrak{F}^{(-1)}$, $\mathfrak{T}^{(-1)}$ and $\mathcal{Q}^{(-1)}$, using (3.16), (3.17), (4.14), and (4.15). Thus, having discretized \mathcal{P} at V_0 , we can in principle, obtain its discretizations for V_{-1} and W_{-1} using the Isotropic Fast wavelet algorithm. But, since the Isotropic Fast wavelet algorithm in this case must be implemented with four dimensional convolutions, which are computationally very expensive, we, instead, calculate the propagator matrices for the resolution and detail level -1 directly. This is done according to the following equations:

$$\begin{aligned}
 \mathcal{P}_{\mathbf{l}, \mathbf{k}}^{(-1)} &= \langle \mathcal{P} D^{-1} T_{\mathbf{k}} \phi^s, D^{-1} T_{\mathbf{l}} \phi^s \rangle = |\det(A)| \left\langle \widehat{\mathcal{P}} e_{A\mathbf{k}} \widehat{\phi}^s(A^*), e_{A\mathbf{l}} \widehat{\phi}^a(A^*) \right\rangle \\
 &= |\det(A)| \int_{\mathbb{R}^2} \widehat{\phi}^a(A^* \boldsymbol{\xi}) e^{i\Delta z \sqrt{k_0^2 - |\boldsymbol{\xi}|^2}} e^{-2\pi i \langle A(\mathbf{k}-\mathbf{l}), \boldsymbol{\xi} \rangle} d\boldsymbol{\xi}.
 \end{aligned}$$

Similarly, we obtain the following expressions:

$$\begin{aligned}
 \mathcal{Q}_{\mathbf{l}, \mathbf{k}}^{(-1)} &= \int_{\mathbb{R}^2} \widehat{\psi}_1^a(A^* \boldsymbol{\xi}) e^{i\Delta z \sqrt{k_0^2 - |\boldsymbol{\xi}|^2}} e^{-2\pi i \langle \mathbf{k}-\mathbf{l}, \boldsymbol{\xi} \rangle} d\boldsymbol{\xi}, \\
 \mathfrak{F}_{\mathbf{l}, \mathbf{k}}^{(-1)} &= |\det(A)|^{1/2} \int_{\mathbb{R}^2} \widehat{\phi}^s(A^* \boldsymbol{\xi}) \widehat{\psi}_1^a(A^* \boldsymbol{\xi}) e^{i\Delta z \sqrt{k_0^2 - |\boldsymbol{\xi}|^2}} e^{-2\pi i \langle A\mathbf{k}-\mathbf{l}, \boldsymbol{\xi} \rangle} d\boldsymbol{\xi}, \\
 \mathfrak{T}_{\mathbf{l}, \mathbf{k}}^{(-1)} &= |\det(A)|^{1/2} \int_{\mathbb{R}^2} \widehat{\phi}^a(A^* \boldsymbol{\xi}) \widehat{\psi}_1^s(A^* \boldsymbol{\xi}) e^{i\Delta z \sqrt{k_0^2 - |\boldsymbol{\xi}|^2}} e^{-2\pi i \langle \mathbf{k}-A\mathbf{l}, \boldsymbol{\xi} \rangle} d\boldsymbol{\xi}.
 \end{aligned}$$

Now, observe that $\widehat{\phi}^a(A^*)$ and $\widehat{\psi}_1^a(A^*)$ overlap only in a small annulus with inner radius b_2 and outer radius b_1 . We denote this annulus by \mathbb{S} . Hence, we can ignore the contribution of

the off diagonal components. We give a justification for this claim by looking more closely at $\mathfrak{F}^{(-1)}$.

The component $\mathfrak{F}^{(-1)}$ acts on the sequence $\{\langle f, T_{A\mathbf{k}}D^{-1}\phi^a \rangle\}_{\mathbf{k} \in \mathbb{Z}^2}$. Let \mathcal{A} be the analysis operator for $\{T_{A\mathbf{k}}D^{-1}\phi^a\}_{\mathbf{k} \in \mathbb{Z}^2}$, i.e. $\mathcal{A}(f) = \{\langle f, T_{A\mathbf{k}}D^{-1}\phi^a \rangle\}_{\mathbf{k} \in \mathbb{Z}^2}$. We claim that $\|\mathfrak{F}^{(-1)}\mathcal{A}(f)\|$ tends to zero, as the area of the annulus, \mathbb{S} , goes to zero, for all f such that \widehat{f} is essentially bounded. This is a reasonable assumption on f because we only have finitely many samples of the wavefield. It is therefore represented by a finite linear combination of the translates of the synthesis scaling function which is bounded in the wavenumber domain.

We write $\mathbf{l} = A\mathbf{l}' + \mathbf{p}_i$, and define $|\det(A)|$ sub-matrices of $\mathfrak{F}^{(-1)}$, denoted by $\mathfrak{F}_i^{(-1)}$, via $(\mathfrak{F}_i^{(-1)})_{\mathbf{l}', \mathbf{k}} = (\mathfrak{F}^{(-1)})_{\mathbf{l}, \mathbf{k}}$. Recall that \mathbf{p}_i are the representatives of the quotient group $\mathbb{Z}^2/(A\mathbb{Z}^2)$. Now, observe that each of $\mathfrak{F}_i^{(-1)}$ is a Toeplitz matrix with each row made up of the Fourier coefficients of the $A^{*-1}\mathbb{Z}^2$ -periodic function $\widehat{\phi}^s(A^* \cdot) \widehat{\psi}_i^a(A^* \cdot) e^{i\Delta z \sqrt{k_0^2 - |\cdot|^2}}$. Therefore, the action $\mathfrak{F}_i^{(-1)}$ on $\mathcal{A}(f)$ is a convolution. Also note that $\widehat{\mathcal{A}(f)} = \widehat{f} \widehat{\phi}^a(A^* \cdot)$, where we identify the bandlimited function, $\widehat{f} \widehat{\phi}^a(A^* \cdot)$ with its $A^{*-1}\mathbb{Z}^2$ -periodic extension. Therefore, applying Plancherel's theorem we conclude,

$$\begin{aligned} \|\mathfrak{F}_i^{(-1)}\mathcal{A}(f)\|^2 &= \int_{A^{*-1}\mathbb{T}^2} \left| \widehat{\phi}^s(A^* \boldsymbol{\xi}) \widehat{\psi}_i^a(A^* \boldsymbol{\xi}) e^{i\Delta z \sqrt{k_0^2 - |\boldsymbol{\xi}|^2}} \widehat{f}(\boldsymbol{\xi}) \widehat{\phi}^a(A^* \boldsymbol{\xi}) \right|^2 d\boldsymbol{\xi} \\ &\leq \|f\|_\infty^2 \int_{A^{*-1}\mathbb{T}^2} \left| \widehat{\psi}_i^a(A^* \boldsymbol{\xi}) \widehat{\phi}^a(A^* \boldsymbol{\xi}) \right|^2 d\boldsymbol{\xi} \\ &\leq \|f\|_\infty^2 \|\widehat{\psi}_i^a(A^* \cdot) \widehat{\phi}^a(A^* \cdot)\|_\infty^2 |\mathbb{S}|, \end{aligned}$$

where $|\mathbb{S}|$ is the area of the annulus \mathbb{S} . This proves our claim that $\|\mathfrak{F}^{(-1)}\mathcal{A}(f)\|$ tends to zero as the area of \mathbb{S} tends to zero. Similar calculations can be carried out for the component, $\mathfrak{T}^{(-1)}$. Hence, by keeping the area of the annulus small, we can neglect the error caused by ignoring the off-diagonal components of the propagator. Our experimental results support this claim (see Figure 4.1).

4.2. IMRA-BASED SOLUTION OF THE ONE-WAY ACOUSTIC WAVE EQUATION

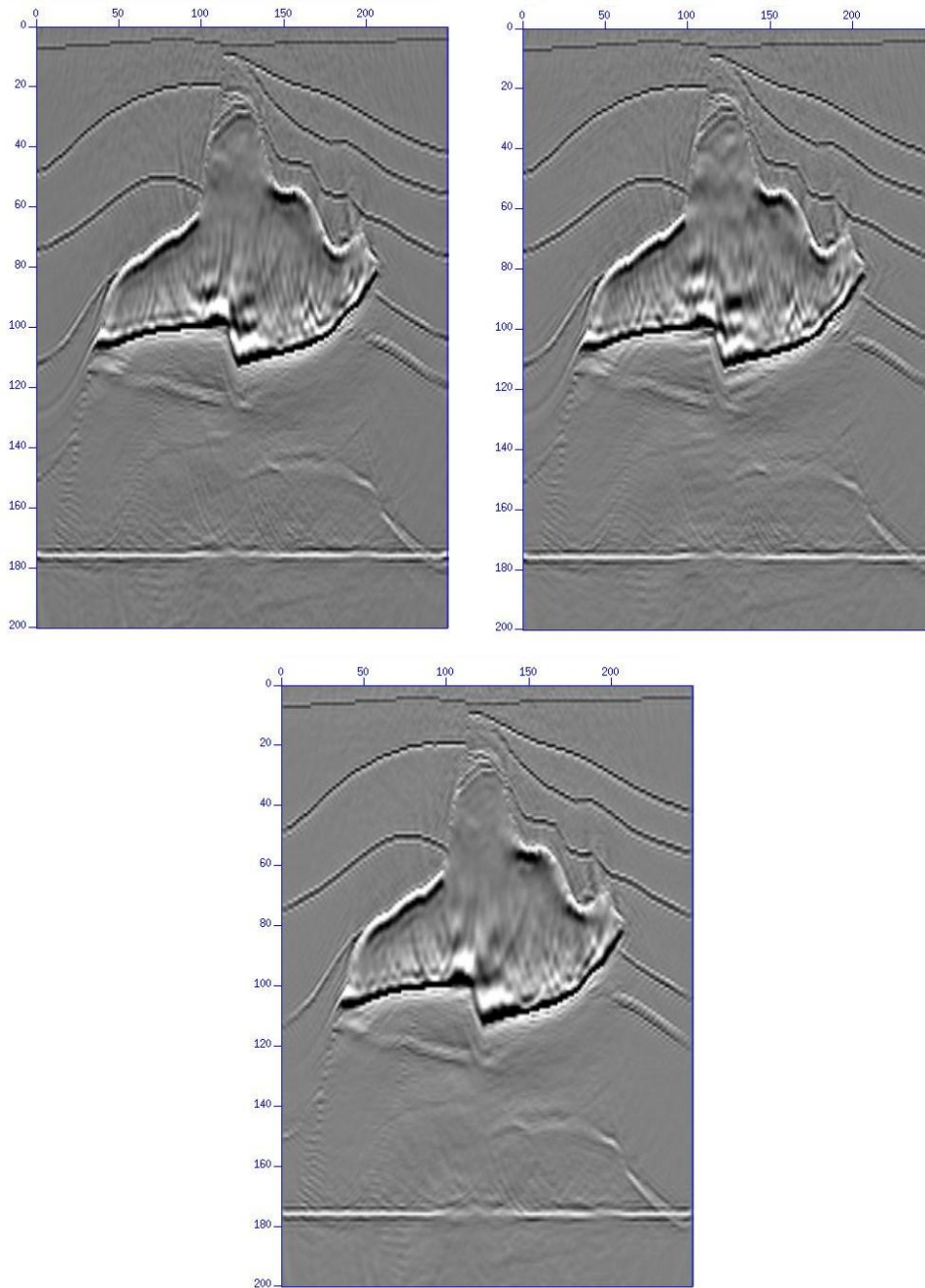


Figure 4.1: Here we show the vertical cross sections of the images obtained for the SEG Salt model using IMRA. The left image on the top was obtained by discretizing the propagator at the zero resolution level. The right image on the top was obtained using one-level of decomposition with the Dyadic dilation matrix. The image on the bottom was obtained using one-level of decomposition using the Quincunx dilation matrix (4.16).

4.2. IMRA-BASED SOLUTION OF THE ONE-WAY ACOUSTIC WAVE EQUATION

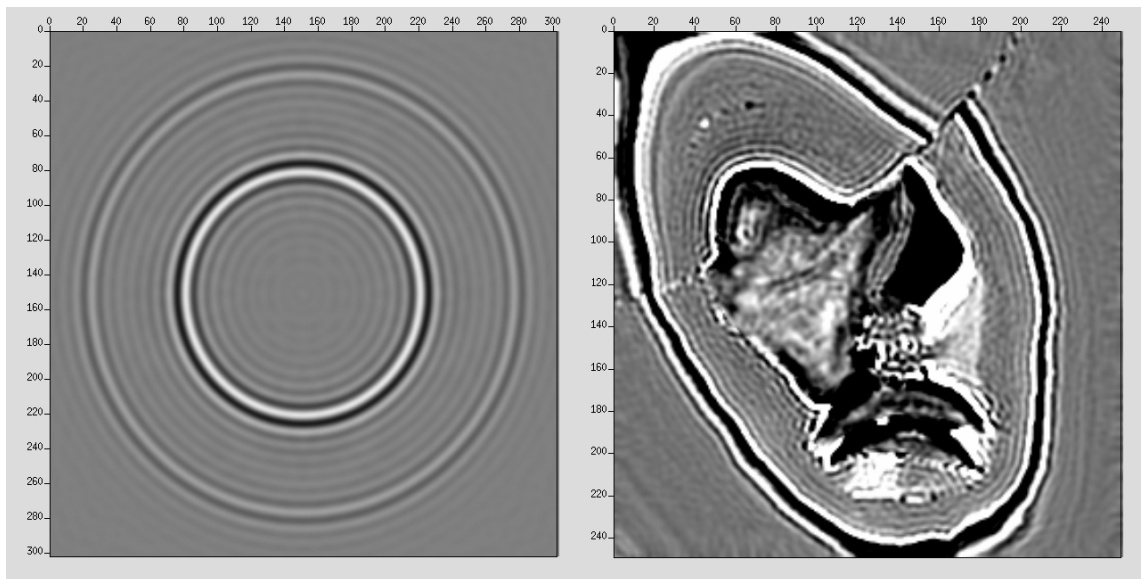


Figure 4.2: Horizontal cross-sections of the results obtained using the IMRA for the Impulse (left) and the Salt (right) models. Due to the radial nature of the filters the faults in all directions are imaged with the same accuracy and have no directional artifacts.

4.2.3 Increasing the Sparsity of the Propagator Matrix

In this subsection, we describe how the decomposition into low and high pass components can be used to increase the sparsity of the propagator matrix and thereby reduce the cost of computation. We use ν to denote the signal in V_0 , i.e. the samples of the wavefield on \mathbb{Z}^2 and refer to this sequence of samples as the original signal and the grid on which it is defined, as the original grid. After decomposing into a low pass component, ν_l and a high pass component, ν_h , using the fast wavelet algorithm, the wavefield is represented by the column vector $(\nu_l, \nu_h)^T$, where T stands for transpose. Recall that the high pass component is undecimated. Hence, ν_h has the same size as ν . Thus, as a result of our decomposition, we increase the amount of data by the size of ν_l . The low pass component, ν_l is a quarter of the size of ν if we use the Dyadic dilation matrix. Applying the propagator (4.13) on $(\nu_l, \nu_h)^T$ yields $(\mathcal{P}^{(-1)}\nu_l, \mathcal{Q}^{(-1)}\nu_h)^T$. The cost of matrix-vector multiplication, $\mathcal{Q}^{(-1)}\nu_h$ is the same as that of the matrix-vector multiplication $\mathcal{P}^{(0)}\nu$.

Nevertheless, the sparsity increases from the fact that we can discard the high pass component for certain values of the ratio, ω/c . Wavenumbers larger than the ratio ω/c correspond to evanescent waves which are considered non-physical [31]. Hence, we only need to propagate the waves corresponding to wavenumbers smaller than ω/c accurately, while the evanescent waves can be damped or set to zero. Now, for ratios $\omega/c < b_2$, we can set the high pass component equal to zero because in this case the high pass component contains only the evanescent waves. By setting the high pass component to zero, we mean that we can set the l -th row of $\mathcal{Q}^{(-1)}$ equal to zero whenever $\omega/c_l < b_2$. In the case of dyadic dilations, $\frac{1}{8} < b_2 < \frac{1}{4}$. This reduces the computational load significantly for regions where the velocity is high and the temporal frequency is low, because in such regions we only propagate the low pass component and with the use of dyadic dilations the low

4.2. IMRA-BASED SOLUTION OF THE ONE-WAY ACOUSTIC WAVE EQUATION

pass component is one-quarter the size of the original grid. This use of the IMRA can be compared to the sub-sampling scheme proposed by Margrave et al [81]. However, unlike Margrave’s sub-sampling, the 1-level IMRA wavelet decomposition is suitable for localized variations of the velocity model. In their implementation, for a fixed frequency, ω , the signal is sub-sampled to reduce the computation time. The IMRA decomposition is more general because we subsample not only for one fixed frequency, but also for various regions of the image where the velocity is high.

A significant gain in speed as compared to standard explicit scheme can be anticipated if we can discard the high pass component for a sufficient number of points in the grid. However, Table 4.1 shows that with dyadic dilation, we have to propagate the high pass component for almost every grid point when the frequency is higher than 9 Hz. When this happens a decomposition ends up being more expensive. Hence, it is useful to decompose the wavefield only for very low frequencies.

Frequency in Hz	Dyadic	Quincunx
1.5 - 8.75	55	0
9 - 16.25	99.5	37.5
16.5 - 23.75	100	93.3
24 - 31.25	100	96.4
31.25 - 37.5	100	100

Table 4.1: Percentage of points in the high pass component that must be propagated for various ranges of temporal frequencies, in the case of Dyadic and Quincunx dilations, for the SEG Salt model.

To rectify this, we want the low pass filter to be supported in a ball that has bigger radius than the one we had with Dyadic dilation, so that the high pass component can be discarded for more values of ω/c . This can be achieved by replacing the Dyadic dilation matrix with the Quincunx matrix:

$$A = \begin{bmatrix} 1 & -1 \\ 1 & 1 \end{bmatrix}. \quad (4.16)$$

This allows the low pass band to be supported in a ball of radius b_0 , where $\frac{1}{4} < b_0 < \frac{\sqrt{2}}{4}$. But, in this case the discretization grid for the low pass component is half the size of the original computation grid. As we can see from Table 4.1, this improves the situation because now, decomposing the wavefield is useful for higher temporal frequencies than in the case of Dyadic dilation. In the actual implementation, the decomposition is only applied for the lower frequencies since it does not save computation time for higher ones.

4.3 Filter Design and Implementation

To implement either the explicit scheme or the IMRA approach, we need a trigonometric polynomial approximation of the discretized phase shift operator. We need short filters (i.e. less terms in the trigonometric polynomial) to keep the computational cost under control. Since the extrapolation is done for small increments Δz , these filters must not amplify the wavefield at every depth step. Hence, we have to optimize the filter under a constraint that guarantees stability and in a way that keeps the computational cost under control. We use a weighted least squares (WLSQ) algorithm due to Thorbecke et al [104], to carry out this task. Recall that wavenumbers larger than the ratio ω/c correspond to evanescent waves which are considered non-physical. The only requirement for the evanescent waves is that they should be damped (i.e. must be less than one in absolute

4.3. FILTER DESIGN AND IMPLEMENTATION

value) so that they do not cause numerical instability. Hence, we use a weight that is equal to one in the propagating region ($|\xi| < \omega/c$) and equal to a very small value (about 10^{-5}) in the evanescent region ($|\xi| > \omega/c$). The filters calculated with this weighted least squares approach have larger errors in the evanescent region but are very accurate for $|\xi| < \omega/c$. Whereas, filters calculated without the weight (i.e. by truncating the Fourier series) have oscillations in the propagating region which results in numerical instability. This is illustrated in Figure 4.3.

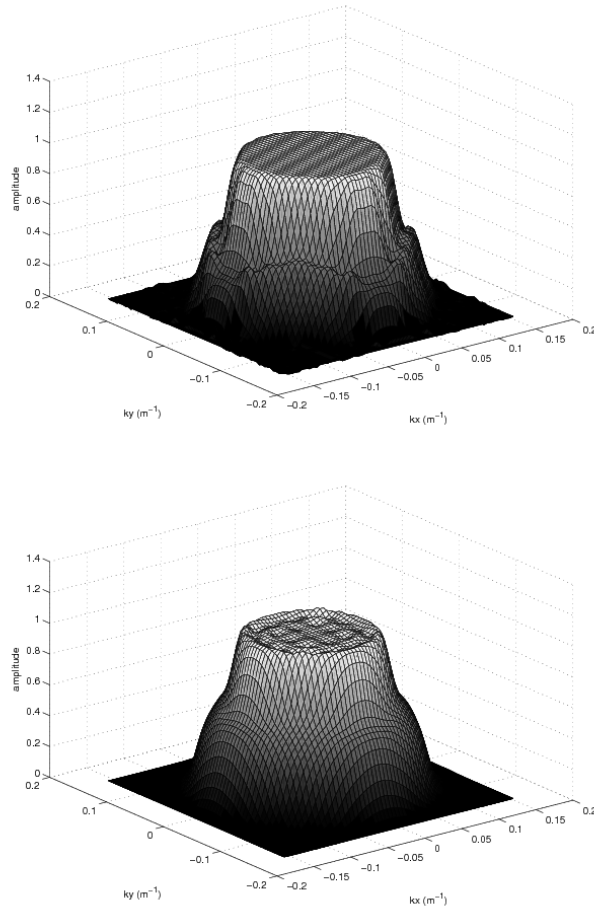


Figure 4.3: Trigonometric polynomial approximations of the propagator filter with a weighted least squares algorithm (top) and with a truncated Fourier series (bottom). Both have 25×25 coefficients.

For 3-D migration, we have to convolve with 2-D filters. Two-dimensional convolutions are expensive and hence, we study ways to make these convolutions computationally efficient without compromising accuracy. We can take advantage of the radial nature of the filters to optimize the 2-D convolution. Since a radial filter is even in both variables, for each point we can first sum up the four quarters of the data and perform the convolution for 1/4 of the original size of the filter i.e. just the first quadrant. Another approach is to design a 1-D filter in the radial variable and use a transformation to map it to a 2-D filter. We consider two such transformations, the McClellan transform [56, 83] and the Soubaras' Laplacian synthesis [101].

4.3.1 McClellan Transform

The McClellan transform was originally described by McClellan in his PhD thesis [83], as a tool to design two dimensional radial filters from their one dimensional profiles in the radial variable.

Let \widehat{P}_0 denote the exact radial filter in the wavenumber domain. Then, \widehat{P}_0 can be approximated by a trigonometric polynomial, say \widehat{P} with respect to the radial variable $k = \sqrt{k_x^2 + k_y^2}$,

$$\widehat{P}(k) = \sum_n a_n \cos(nk).$$

Using T_n to denote the n -th degree Chebychev polynomial,

$$\widehat{P}(k_x, k_y) = \sum_n a_n T_n \left(\cos \left(\sqrt{k_x^2 + k_y^2} \right) \right),$$

where $T_n(\cos(x)) = \cos(nx)$.

Multiplication by $T_n(\cos(k))$ in the wavenumber domain is equivalent to repeated convolutions in the space domain by a filter approximating $\cos \left(\sqrt{k_x^2 + k_y^2} \right)$. This can be

implemented by the so-called Chebychev recursion scheme described in [84].

The filter suggested by McClellan for the approximation of $\cos\left(\sqrt{k_x^2 + k_y^2}\right)$ is the 3×3 filter,

$$\begin{bmatrix} 1/8 & 1/4 & 1/8 \\ 1/4 & -1/2 & 1/4 \\ 1/8 & 1/4 & 1/8 \end{bmatrix}.$$

For seismic imaging, Hale suggested the so called ‘Improved McClellan’ filter, [56], given by:

$$\begin{bmatrix} -c/8 & 0 & c/4 & 0 & -c/8 \\ 0 & 1/8 & 1/4 & 1/8 & 0 \\ c/4 & 1/4 & -(1+c)/2 & 1/4 & c/4 \\ 0 & 1/8 & 1/4 & 1/8 & 0 \\ -c/8 & 0 & c/4 & 0 & -c/8 \end{bmatrix}.$$

Observe from Figure 4.5 that this filter is a good approximation for $\cos\left(\sqrt{k_x^2 + k_y^2}\right)$ if k_x and k_y up to half the bandwidth of the original signal, but for higher wavenumbers, the approximation is good only along the k_x and k_y axes and deviates significantly along the $k_x = k_y$ line. This produces significant dispersion in the 45° azimuth angle of the image. (See Figures 4.7 and 4.9).

4.3.2 Soubaras’ Laplacian Synthesis

Another way of mapping 1-D filter co-efficients to 2-D filters via Chebychev recursion is Soubaras’ Laplacian synthesis [101]. In this approach, $L_0 := k_x^2 + k_y^2$ is approximated by a

4.3. FILTER DESIGN AND IMPLEMENTATION

trigonometric polynomial of the form,

$$L = (d_x(0) + d_y(0))/2 + \sum_{n=1}^{N_x} d_x(n) \cos(nk_x) + \sum_{n=1}^{N_y} d_y(n) \cos(nk_y), \quad (4.17)$$

where $d_x(n)$ are the coefficients of the Fourier Series of the function f defined by $f(k_x) =$

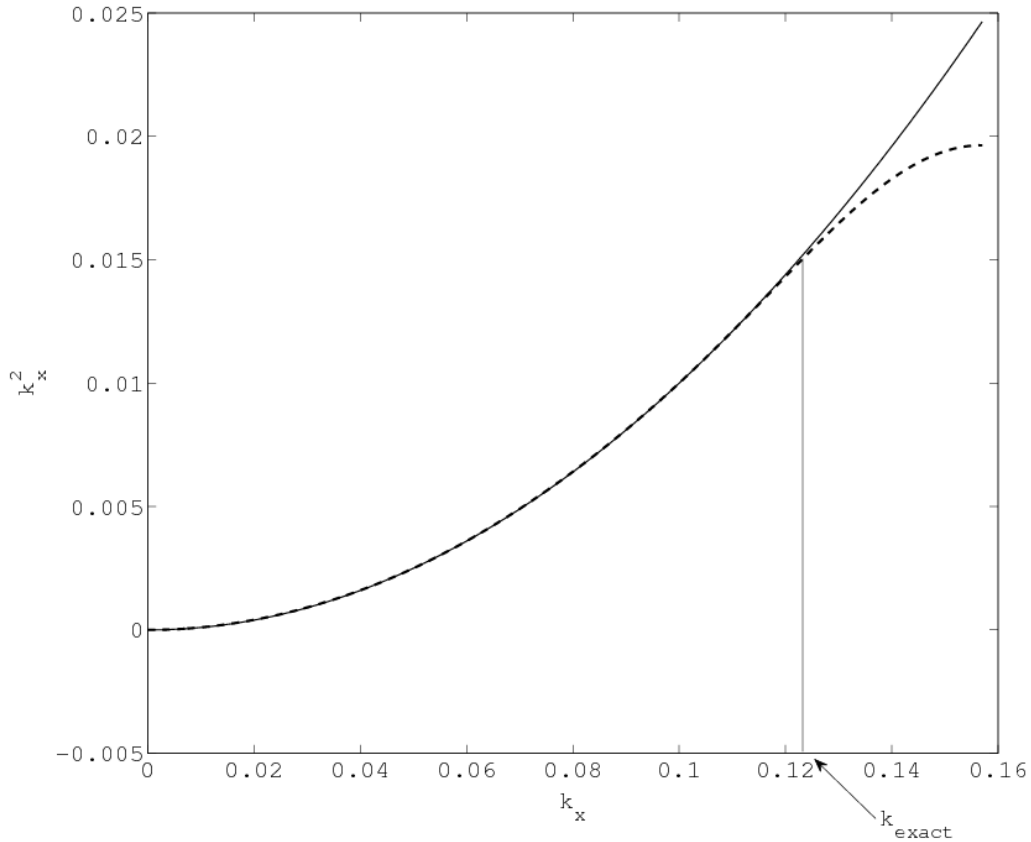


Figure 4.4: The 1-D profiles of the filters, L (dashed) and L_0 (solid), along the k_x -axis. Here L is a trigonometric polynomial in Equation (4.17) with $N_x = N_y = 5$. The approximation is exact up to k_{exact} .

$k_x^2.H(k_x)$ for k_x in $[-\Delta x/\pi, -\Delta x/\pi]$ and extended periodically. Here Δx is the spatial sampling interval and H is a smoothing window. We obtain $d_y(n)$ in the same way. Notice from Figures 4.4 and 4.5 that L is a good approximation for L_0 up to a certain radius say

4.3. FILTER DESIGN AND IMPLEMENTATION

k_{exact} . This imposes a limit on the dip angles that can be imaged correctly, but up to this radius the approximation is accurate in all directions.

Since L and cosine are continuous functions we can recover the entire range of values of L using the following equation

$$L = \gamma(h) = 0.5(L_{min} - L_{max}) \cos(h) + 0.5(L_{min} + L_{max}), \quad 0 \leq h \leq \pi, \quad (4.18)$$

where L_{min} and L_{max} are the minimum and the maximum values of the synthesized Laplacian L . Recall that the exact filter in the wavenumber domain is denoted by \hat{P}_0 . Now, the radial filter $\hat{P}_0(L) = \hat{P}_0(\gamma(h))$ can be approximated by a Cosine Series (in the variable h) via

$$\hat{P}(\gamma(h)) = \sum_n t_n \cos(nh).$$

Solving Equation (4.18) for $\cos(h)$, \hat{P} can be written with respect to L as follows

$$\hat{P}(L) = \sum_n t_n T_n [(2L - L_{min} - L_{max}) / (L_{min} - L_{max})].$$

The operator P is implemented via a Chebychev recursion similar to the one used for the McClellan transform. Here, instead of a filter approximating $\cos(\sqrt{k_x^2 + k_y^2})$ we use the filter $(2L - L_{min} - L_{max}) / (L_{min} - L_{max})$. This filter is implemented via convolution with the matrix

$$\frac{1}{L_{min} - L_{max}} \begin{bmatrix} 0 & 0 & d_y(N_y) & 0 & 0 \\ 0 & 0 & \vdots & 0 & 0 \\ d_x(N_x) & \dots & d_x(0) + d_y(0) - L_{min} - L_{max} & \dots & d_x(N_x) \\ 0 & 0 & \vdots & 0 & 0 \\ 0 & 0 & d_y(N_y) & 0 & 0 \end{bmatrix}.$$

4.3. FILTER DESIGN AND IMPLEMENTATION

Observe that unlike McClellan, the 1-D filter design must be done after the design of the transformation filter L . This is because the function γ depends on L . The weight function in the WLSQ algorithm must correspond to the appropriate cut off given by $h_c = (2L_c - L_{min} - L_{max}) / (L_{min} - L_{max})$ where $L_c = \min \{ \omega^2 / c^2, k_{exact}^2 \}$.

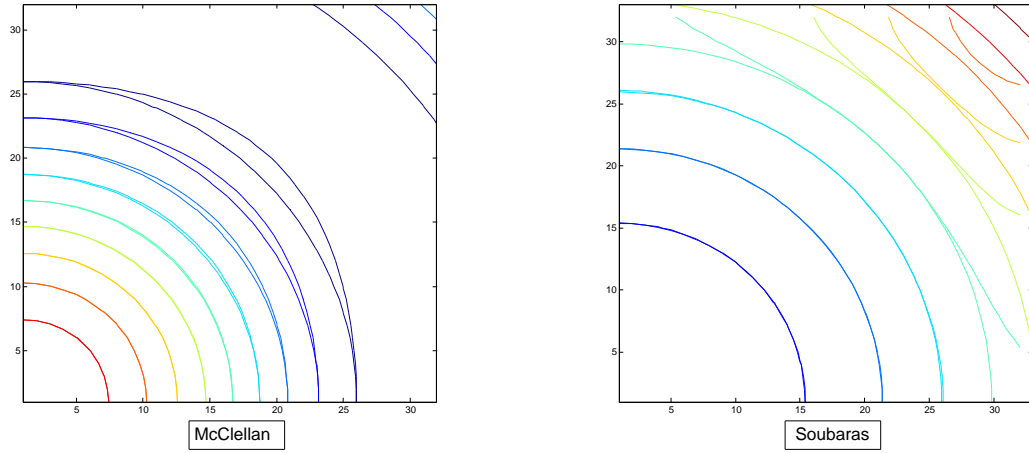


Figure 4.5: The figure on the left has the contours of the ‘Improved McClellan filter’ plotted along with the exact function $\cos\left(\sqrt{k_x^2 + k_y^2}\right)$. The figure on the right is a contour plot of a synthesized Laplacian, L with $N_x = N_y = 5$ along with the contour plot of the exact function $k_x^2 + k_y^2$. Notice that although the McClellan filter gives a very good approximation of the exact function along the axes, it deviates significantly along the $k_x = k_y$ line. The Soubaras’ filter is a good approximation in all directions up to a radius k_{exact} (See Figure 4.4) which is larger than the radius up to which the McClellan filter gives a good approximation. Beyond k_{exact} , the Soubaras’ filter also deviates from the exact function $k_x^2 + k_y^2$ as the contours for the filter are not radial for radii bigger than k_{exact} .

Figure 4.5 shows that the filter L is a good approximation to $k_x^2 + k_y^2$ for a bigger domain than the one in which the ‘Improved McClellan’ filter is accurate. See Figures 4.7 and 4.10.

4.3.3 Computational Cost

A comparison between the number of floating point operations (FLOPS) required for the Chebychev recursion scheme and direct convolution is given in [56]. Although, the number of FLOPS is much higher for direct convolution, it is important to note that the Chebychev recursion scheme is computationally more complex and hence the computational overhead may increase the computation time. An empirical study for the time required by various computers for the implementation of each method is presented in [103]. Surprisingly, for some computers direct convolution turns out to be less expensive.

The computational cost for Soubaras’ method in terms of the number of FLOPS is comparable to that of the McClellan transform but the results obtained from the former method do not have the directional bias in contrast to those obtained by means of the McClellan transform. Therefore, we recommend the use of Soubaras’ method for seismic migration.

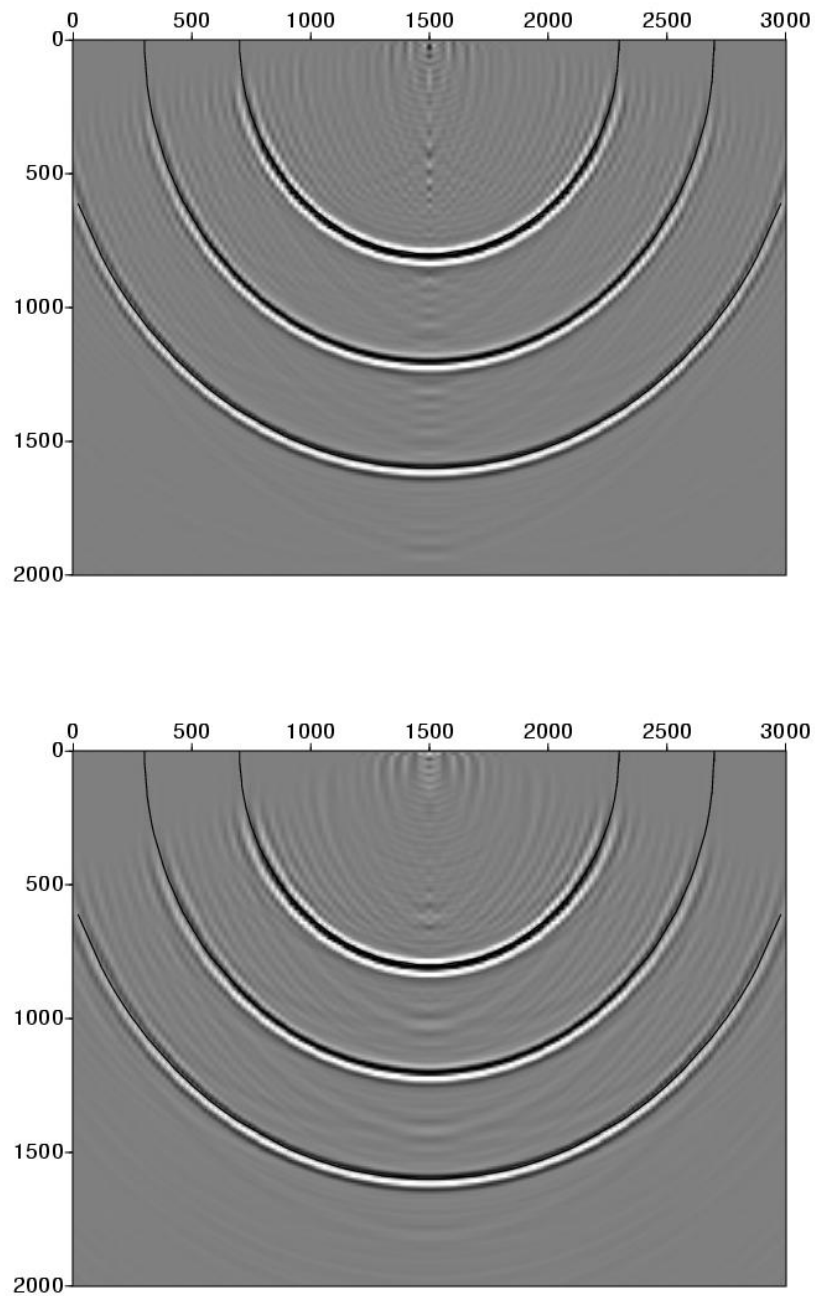


Figure 4.6: Slice $y = 76$ of the constant velocity impulse model using McClellan (top) and Soubaras (bottom).

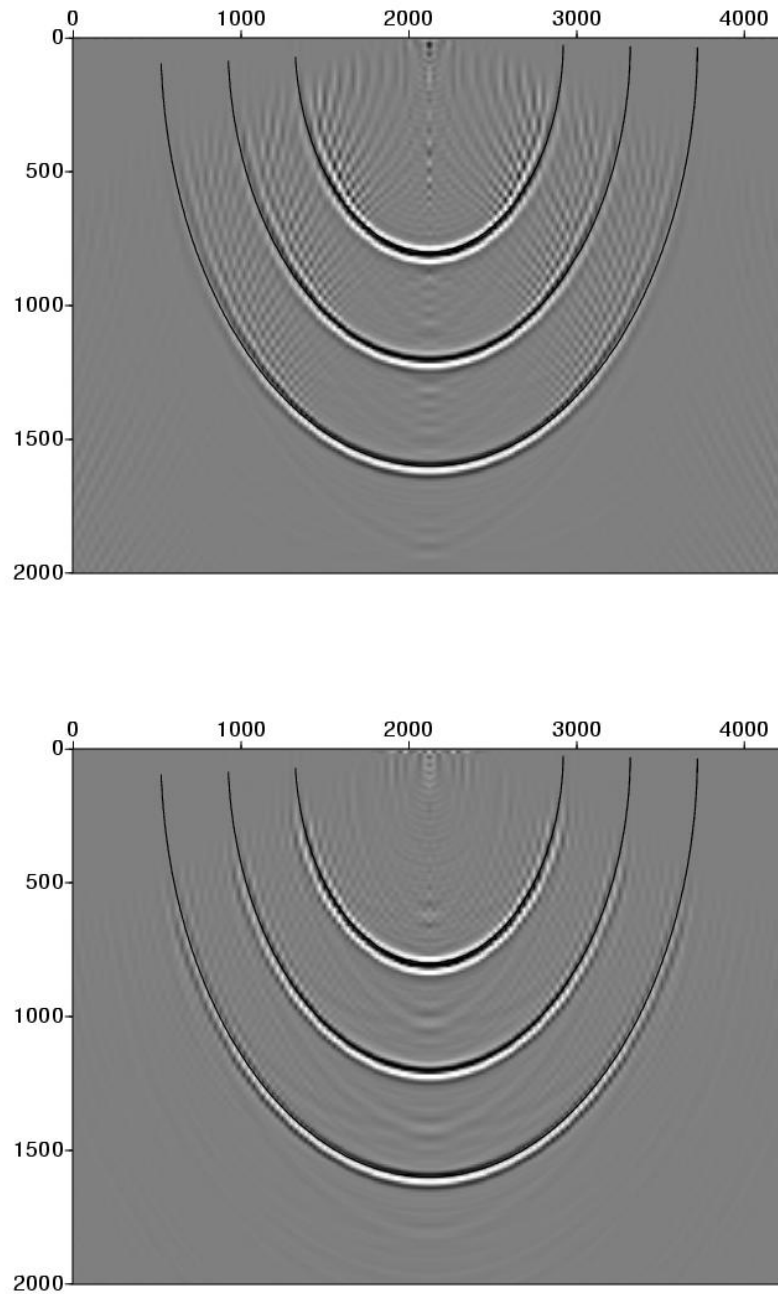


Figure 4.7: Slice $x = y$ of the constant velocity impulse model using McClellan (top) and Soubaras (bottom). The result from McClellan shows a lot of dispersion in the higher angles while the Soubaras gives an accurate result.

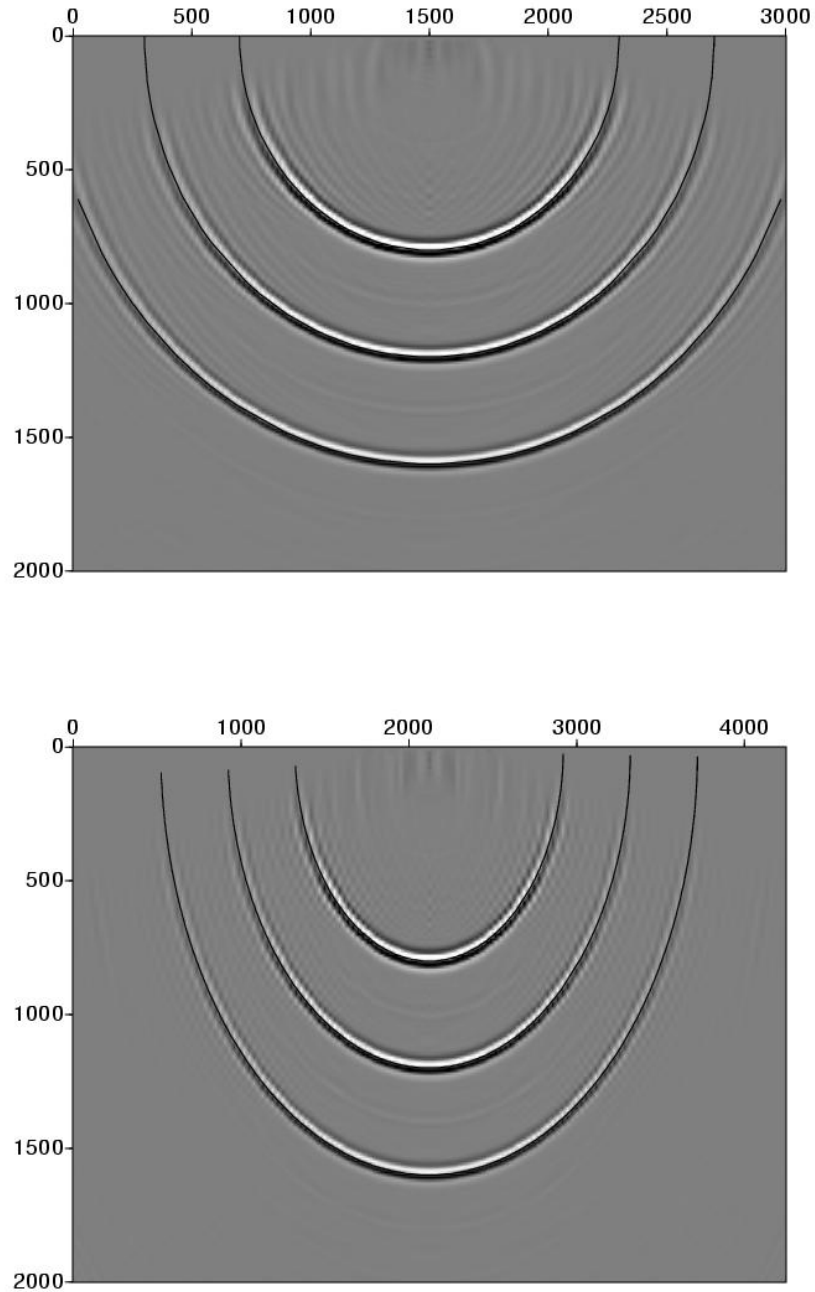


Figure 4.8: Slice $y = 76$ (top) and $x = y$ (bottom) of the constant velocity impulse model using 2D IMRA filters. These results have less ringing than the ones obtained from Soubaras. (Figures 4.6,4.7)

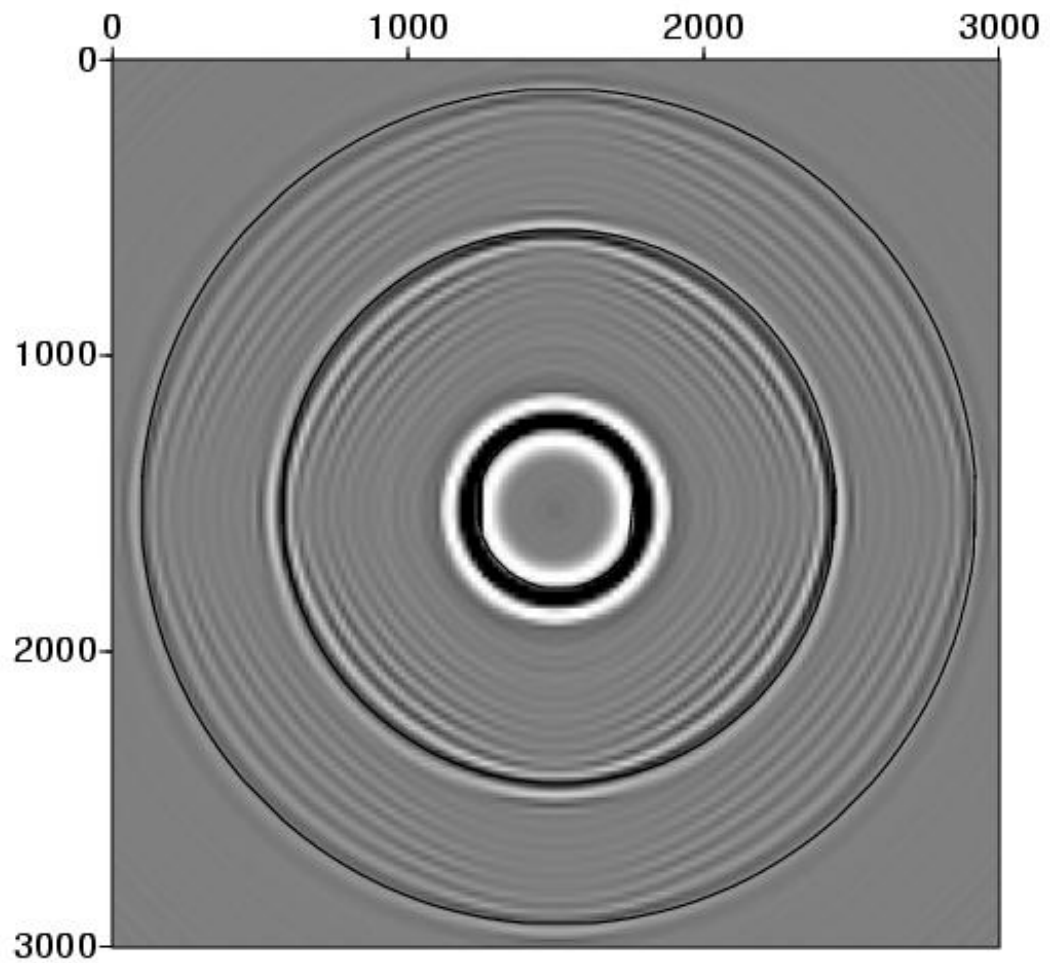


Figure 4.9: Slice $z = 75$ using McClellan. Notice the dispersion in the 45° azimuth angle which is absent in the results obtained from Soubaras (Figure 4.10) and full 2-D IMRA implementation (Figure 4.11).

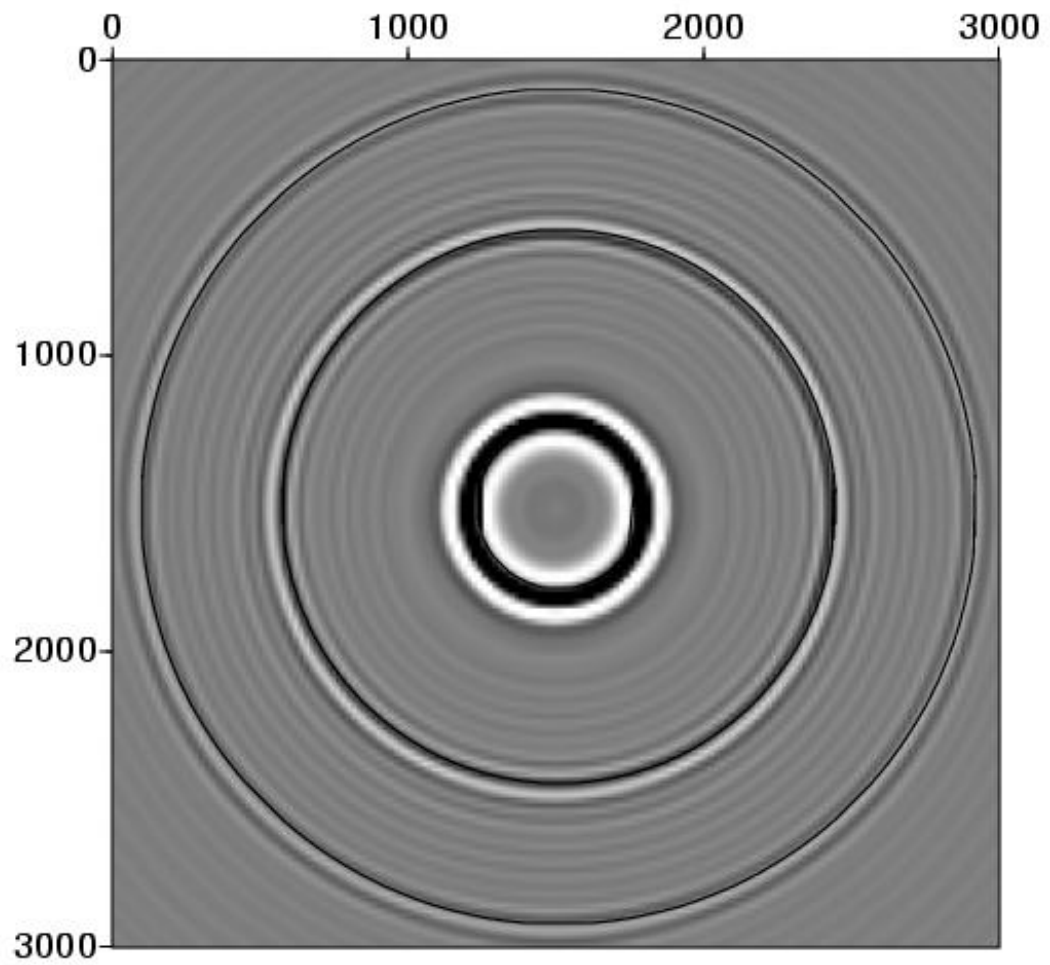


Figure 4.10: Slice $z = 75$ of the constant velocity impulse model using Soubaras. The result is accurate in all directions but has more ringing than the result obtained from a full 2-D convolution (Figure 4.11)

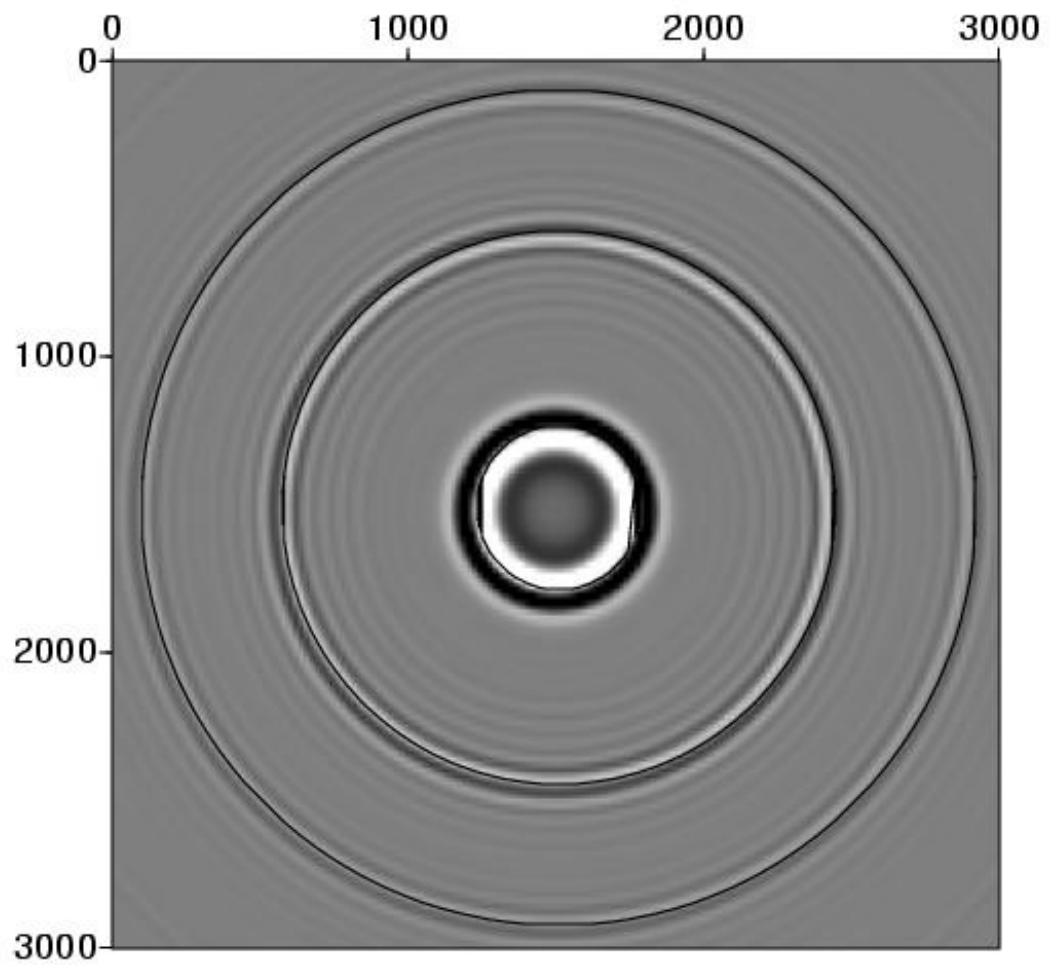


Figure 4.11: Slice $z = 75$ of the constant velocity impulse model using 2D IMRA filters at the zero resolution level (without decomposing into low and high pass components).

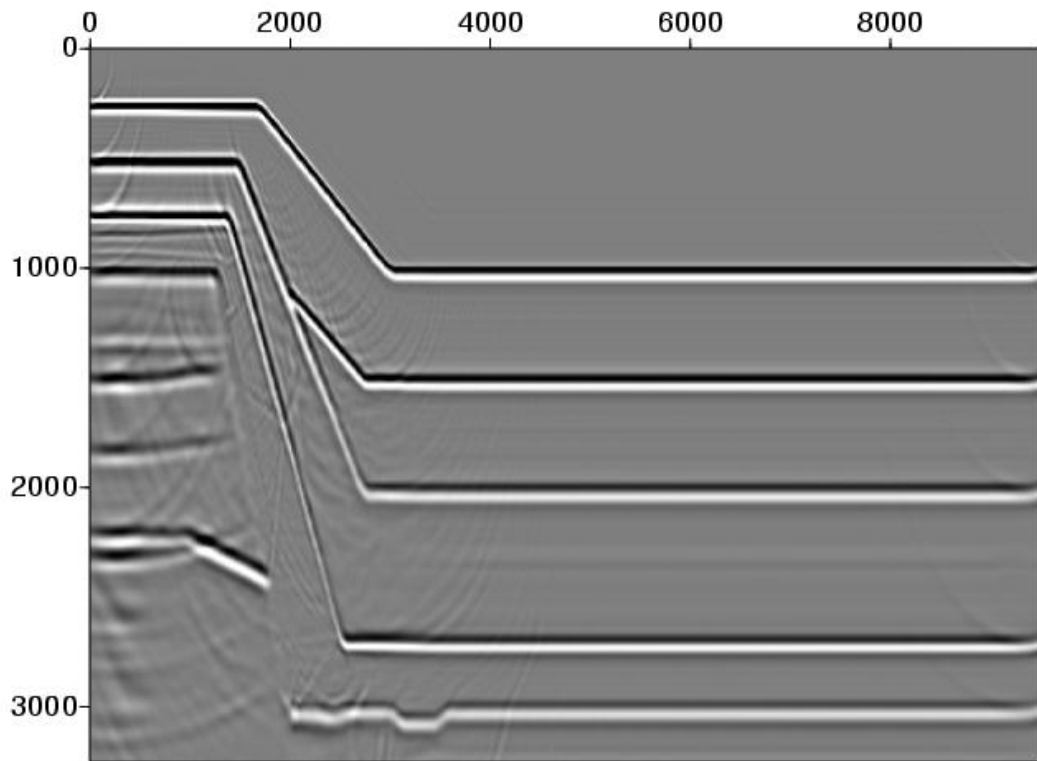


Figure 4.12: Slice $y = 5$ of the steep model using McClellan.

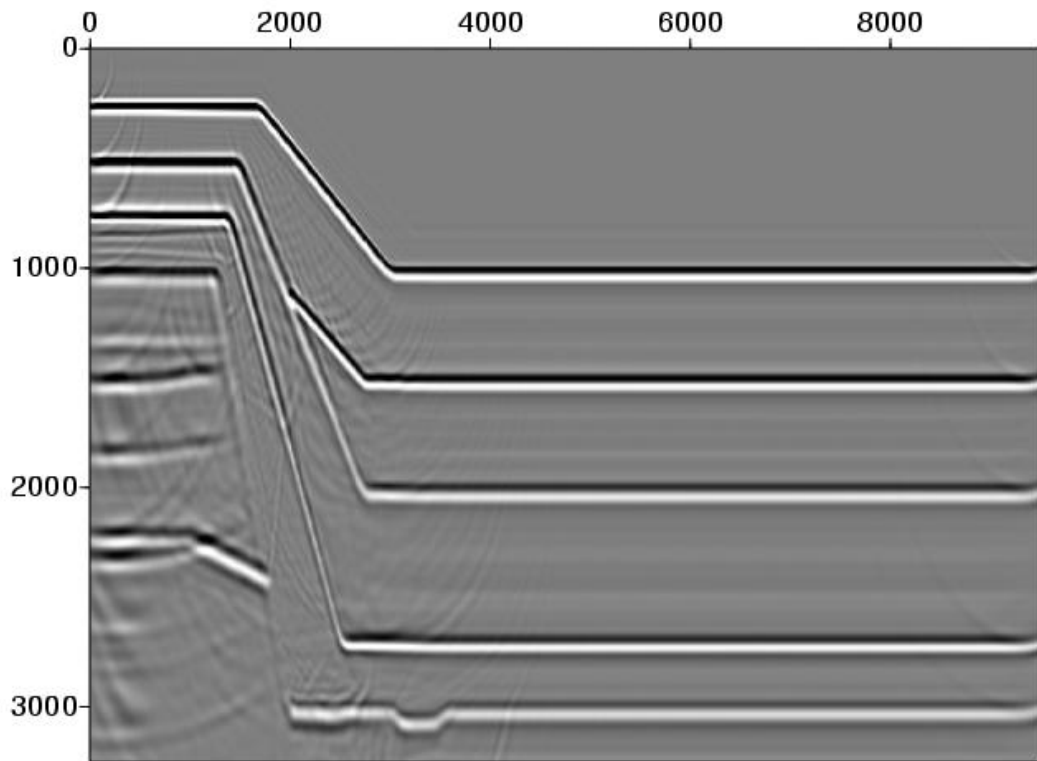


Figure 4.13: Slice $y = 5$ of the steep model using Soubaras.

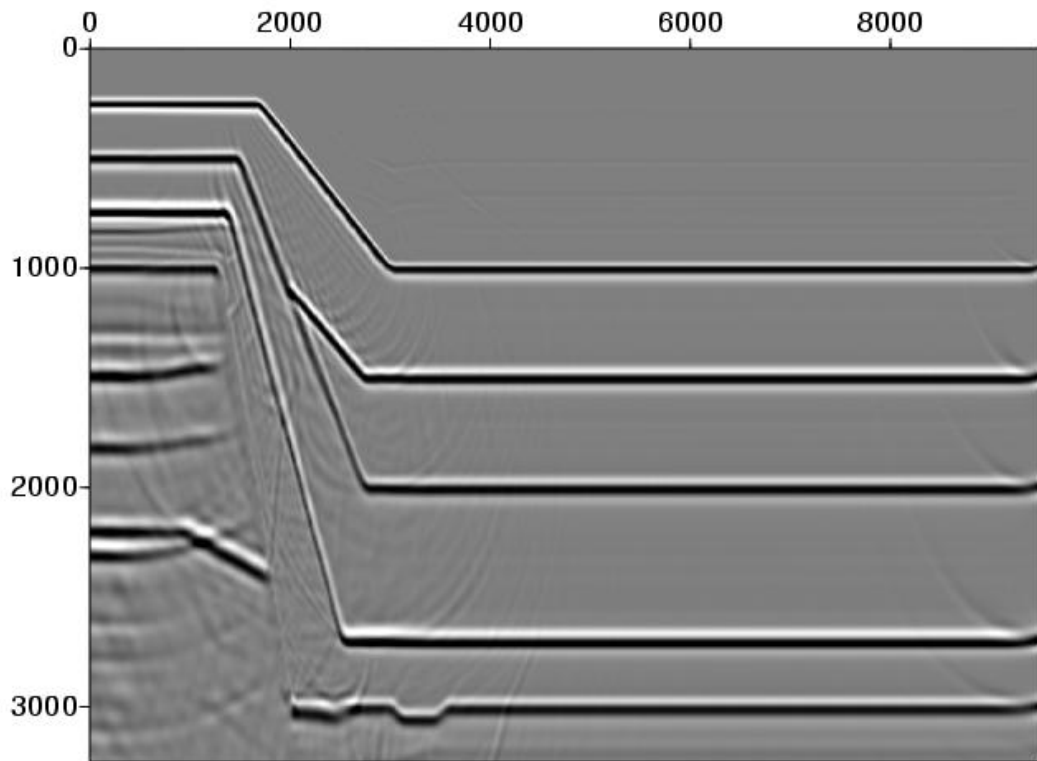


Figure 4.14: Slice $y = 5$ of the steep model using 2D IMRA filters at the zero resolution level (without decomposing into low and high pass components).

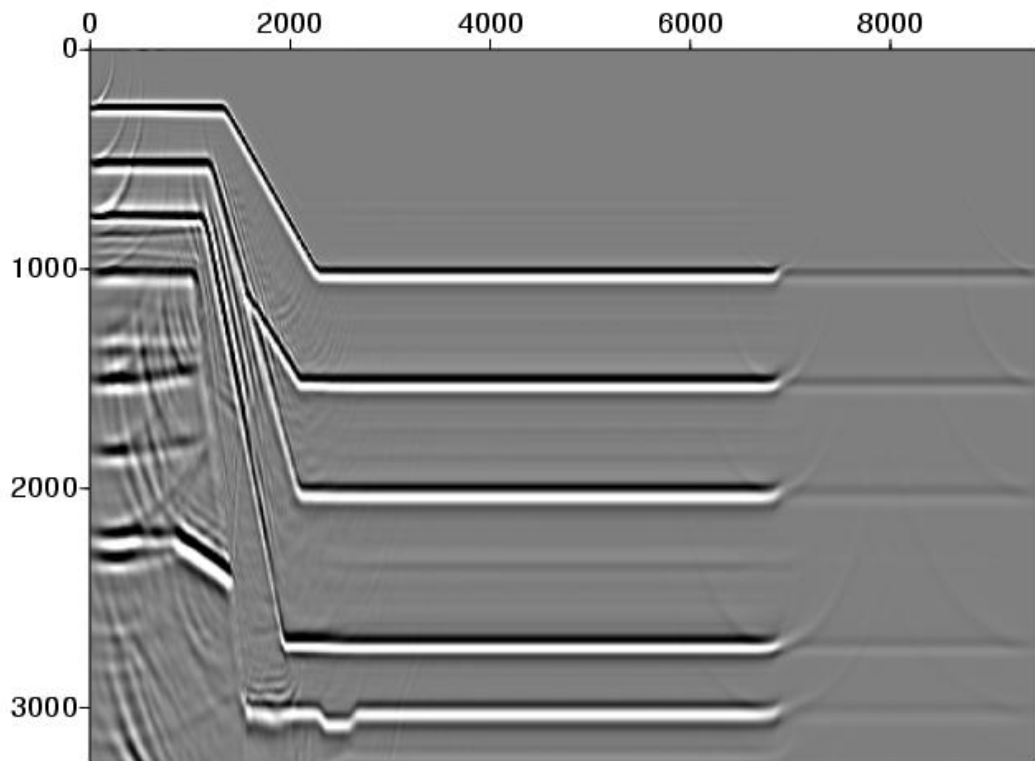


Figure 4.15: Slice $x = y$ of the steep model using McClellan. Notice the dispersion in the higher angles of propagation. The results obtained from Soubaras (Figure 4.16) and 2-D IMRA filters (Figure 4.17) do not have these artifacts.

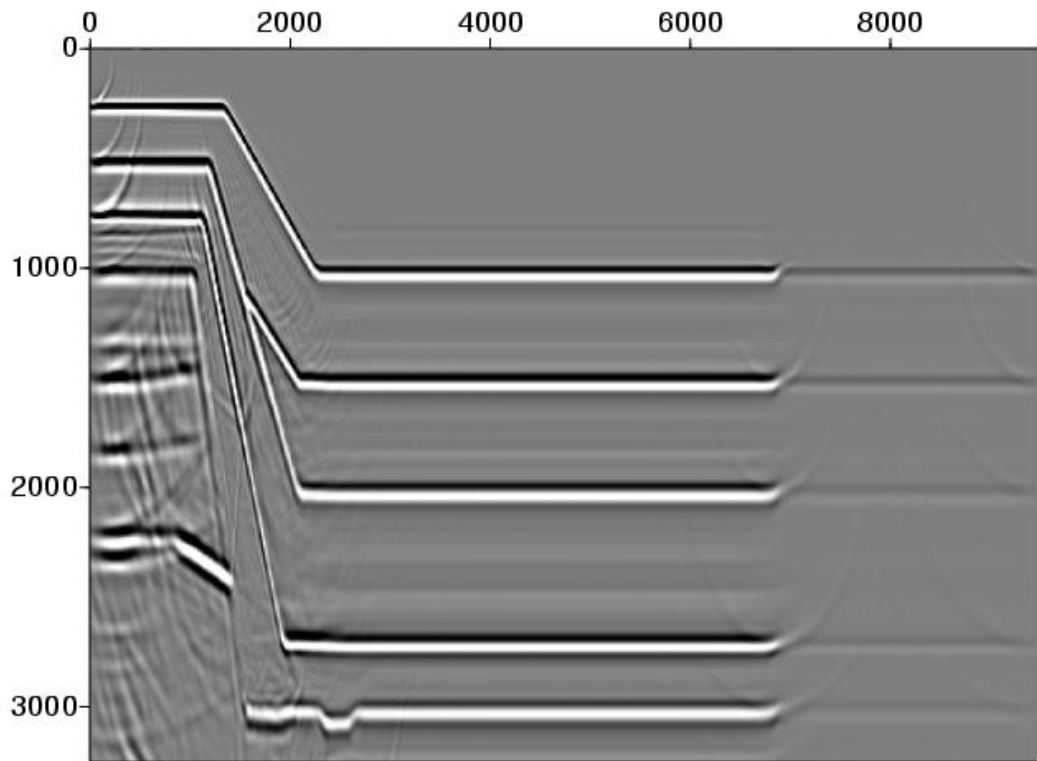


Figure 4.16: Slice $x = y$ of the steep model using Soubaras.

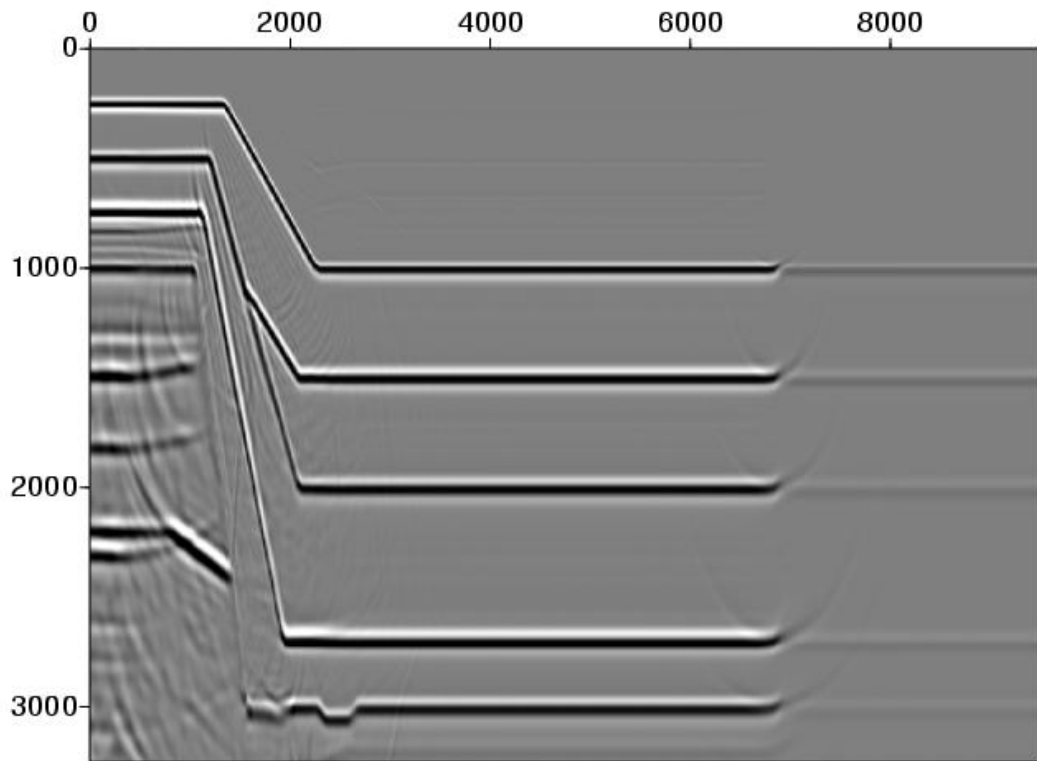


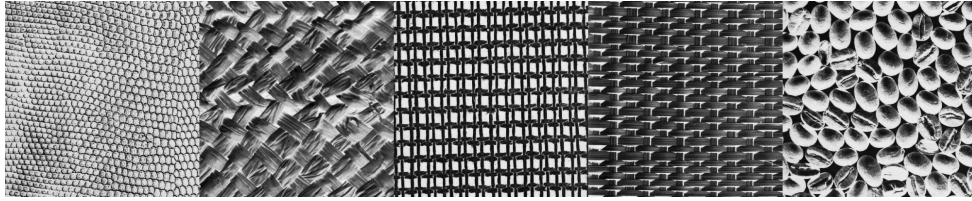
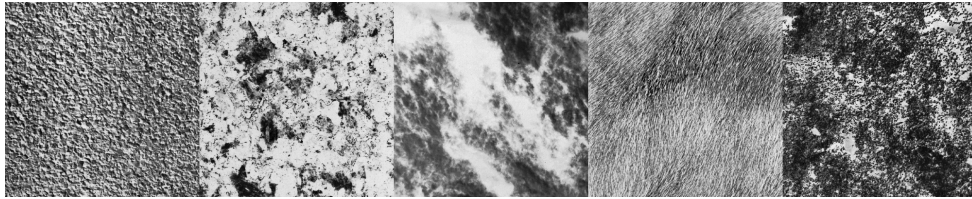
Figure 4.17: Slice $x = y$ of the step model using 2D IMRA filters at the zero resolution level (without decomposing into low and high pass components).

Rotationally Invariant 3-*D* Texture Classification

5.1 Introduction

Textures appear in most natural images, but there is no precise mathematical definition of a texture. However, there are various descriptions of textures available in the literature. These approaches can be broadly classified as structural or deterministic, and stochastic [26, 35, 58, 76, 105]. The structural approach is more suitable for describing textures that can be formed by repeating a unit pattern also known as a primitive. Examples of such textures are shown in Figure 5.1. Textures in which the absence of a faithful repetition of a certain pattern is the norm are better described by statistical models. Some examples of non-deterministic textures are shown in Figure 5.2.

Textures appear naturally in many classes of imaging, among them medical images used for diagnostic and research purposes. In imaging modalities such as X-ray CT and

Figure 5.1: Examples of structural 2- D texturesFigure 5.2: Examples of stochastic 2- D textures

MRI, different tissues give rise to different textures, but these textures are now 3- D . Thus, efficient texture classification and segmentation routines can be used for the automatic or semi-automatic detection of anomalies. Textures arising from tissues can not be treated as those in Figure 5.1, where the precise perpetual repetition of the primitive determines the texture. Natural tissue variation should be taken into account. In addition, various types of noise join forces to enhance the variability in textures of this sort. Thus, stochastic models are better suited for modeling textures that appear in medical imaging. These textures are the focus of this chapter.

The first step in a texture analysis problem is to identify a good set of features or texture signatures. A feature is a certain attribute of the model. To be useful, a feature should be easily computable otherwise it can not be easily utilized. A **texture signature** is a collection of features identifying a texture. Feature vector is an alternative term that can be used instead of texture signature. In fact, the use of the noun ‘vector’ underscores the importance of vector-valued texture signatures versus scalar-valued signatures. The complexity of the nature of a texture becomes feasible with a multidimensional approach.

The dimensionality of a texture signature is very critical in enabling texture discrimination. The feature vectors or texture signatures corresponding to two different textures should be distant enough from each other with respect to a suitable metric. Various kinds of features have been considered in the literature such as those arising from spatial frequency based techniques such as Gabor filters [8, 91, 102] and wavelets [24, 45, 106], or those arising from spatial interaction and autoregressive models such as Markov random fields [25, 64, 80]. The autoregressive and spatial interaction models are particularly attractive because they take into account the local statistical interactions of an image which capture a lot of information about textures. Of these, Gaussian Markov Random Fields (GMRF) have been studied most extensively for 2-*D* texture analysis [25, 35, 65, 91]. More recently, GMRFs have been used for the study of 3-*D* textures in [93]. The literature on 3-*D* texture analysis in general is extremely limited due to the tremendous computational challenges one encounters in this kind of image analysis. A few recent generalizations of the 2-*D* methods to 3-*D* can be found in [69, 70, 77, 94, 108].

We are interested in rotationally invariant classification of 3-*D* textures because, in applications such as medical imaging, a tissue type must be classified regardless of the position or orientation of the subject. Various authors have considered different approaches to obtain a rotationally invariant classification scheme, mostly in 2-*D*. In [66], Kashyap and Khotanazad propose a so-called circular symmetric autoregressive model. They fit two traditional simultaneous autoregressive models, one for the nearest neighbors and one for the diagonal nearest neighbors. By the diagonal nearest neighbors they mean points on the diagonal at a unit distance. These points do not lie on the original lattice so the gray scale values here are obtained via linear interpolation. The parameters for these models are used as rotation invariant features. This kind of circularly symmetric models are also

considered in [91], where higher order neighborhoods beyond first order ones are also employed. In [91], the authors also propose circularly symmetric Gabor filter-based features. The main shortcoming of these models is that they impose an isotropic structure on possibly non-isotropic textures. A mathematically rigorous treatment of isotropic textures can be found in [88]. However, when we are dealing with textures that show directional characteristics, isotropic models limit the flexibility in texture classification. This problem is also recognized in [35], where the authors model the textures using a continuous stationary Gaussian random field. Rotations are defined via a continuous counterpart of the discrete power spectral density associated to a discrete model defined on a finite lattice. This is similar to the approach that we describe for rotation of textures in Section 5.3.2. Using the continuous power spectral density, they derive a likelihood function for the rotation parameter. The classification is then carried out in two steps. First, they obtain a maximum likelihood estimate for the rotation angle and then they compare against each texture in the training set for classification. This approach is shown to work well in 2- D but a 3- D version would be computationally extremely expensive since the likelihood function they obtain constitutes a product over all the lattice nodes. A 3- D rotation invariant approach for texture classification using local binary patterns is considered in [46]. To the best of our knowledge there has been no previous attempt of a 3- D rotation invariant texture classification using GMRF.

Instead of using a rotationally invariant probabilistic model for a texture, we aim at defining a rotationally invariant distance between two texture signatures which might themselves be non-isotropic. Two different non-isotropic textures might not be distinguishable if isotropy of the texture signatures is imposed. Thus, using non-isotropic signatures, and implementing the rotational invariance via a distance function, makes the models more flexible.

We model discrete textures, i.e. textures defined on a discrete lattice, using GMRF following the approach of Rama Chellappa described for 2- D textures in [25], and extended to 3- D volumes in [93]. GMRFs are particularly useful for the following reasons:

- These stochastic models have a very well understood mathematical structure,
- The computability of Kullback-Leibler distance (see Section 5.3.1),
- Relatively low computational cost of parameter estimation and texture synthesis.

The texture signature is obtained by fitting a GMRF model to each of a finite set of rotations of the texture. This finite set of rotations is obtained by a uniform sampling of $SO(3)$. We define a rotationally invariant distance between these texture signatures in Section 5.3. Since the rotation of a discrete texture is not well-defined, we propose a continuous counterpart of the discrete texture that we wish to rotate. We consider a continuous texture to be a realization of a stationary Gaussian process on \mathbb{R}^3 . *Then the concept of rotating a texture takes a natural form and is shown to be (Equation (5.20)) equivalent to rotating the corresponding autocovariance function.* The conversion between discrete and continuous textures is achieved via Isotropic Multiresolution Analysis developed in Chapters 2 and 3. This is discussed in detail in Section 5.3.2.

5.2 Description of the GMRF Model

To describe the GMRF model, we follow the notation in [93]. The image/volume is defined on a 2/3- D lattice denoted by $\mathbf{\Lambda}$. By a lattice, we mean the following:

$$\mathbf{\Lambda}^{2D} = \{\mathbf{k} = (i, j) \mid 1 \leq i \leq M, 1 \leq j \leq N\},$$

$$\mathbf{\Lambda}^{3D} = \{\mathbf{k} = (i, j, k) \mid 1 \leq i \leq M, 1 \leq j \leq N, 1 \leq k \leq P\}.$$

where, i, j, k are integers and M, N, P denote the size of the lattice in each dimension. The total number of sites or nodes on the lattice are denoted by N_T . In the 2- D case, $N_T = MN$ and for 3- D , $N_T = MNP$. In the rest of this chapter, we assume that we work with a 3- D lattice though most of the discussion in this section applies verbatim to 2- D .

A **neighborhood** $\eta_{\mathbf{k}}$ of node \mathbf{k} is a subset of the lattice, $\eta_{\mathbf{k}} \subset \mathbf{\Lambda}$ such that,

- $\mathbf{k} \notin \eta_{\mathbf{k}}$,
- $l \in \eta_{\mathbf{k}} \Rightarrow \mathbf{k} \in \eta_l$.

A **neighborhood system** η , is the collection of neighborhoods at all nodes, $\eta = \{\eta_{\mathbf{k}}, \mathbf{k} \in \mathbf{\Lambda}\}$.

A **clique** C defined with respect to η , is a subset of $\mathbf{\Lambda}$ such that C either contains a single node, or all nodes in C are neighbors. The set of all cliques in a neighborhood is denoted by \mathcal{C} and \mathcal{C}_n , for $n \in \mathbb{N}^+$, denotes the set of cliques with n nodes.

Let \mathbf{X} be a family of random variables defined on the lattice $\mathbf{\Lambda}$ via $\mathbf{X} := \{X_1, \dots, X_{N_T}\}$. We refer to \mathbf{X} as a **random field** and use the notation $\mathbf{X} = \mathbf{x}$ for the joint event $\{X_i = x_i, i = 1, \dots, N_T\}$, where $\mathbf{x} = \{x_1, \dots, x_{N_T}\}$ is called a **configuration** of \mathbf{X} . An image/volume is a configuration or realization of \mathbf{X} . Each x_i belongs to a (usually finite) set \mathcal{A} , referred to as the **alphabet** (or gray-levels in image processing terminology).

5.2.1 Gibbs and Markov Random Fields

In this subsection, we assume that the alphabet \mathcal{A} is discrete to keep the discussion simple. The technical details required to describe random fields are not needed for our discussion on GMRF in Section 5.2.2, even though the alphabet in that case is \mathbb{R} . For the general

theory of Gibbs and Markov fields with a continuous alphabet, the reader is referred to Chapter 2 in [55]. A random field \mathbf{X} is referred to as a **Gibbs Random Field (GRF)** if it satisfies the following probability distribution:

$$\mathbb{P}(\mathbf{X} = \mathbf{x}) = \frac{1}{Z} \exp\left(\frac{U(\mathbf{x})}{\mathcal{T}}\right).$$

where Z is a positive normalizing constant known as the **partition function**, \mathcal{T} is the temperature and U is referred to as the **Gibbs energy**.

For a finite lattice Λ with a symmetric neighborhood structure η , an example of Gibbs energy function is defined as:

$$U(\mathbf{x}) = \sum_{\mathbf{k} \in \Lambda, C \in \mathcal{C}_1} V_C(x_{\mathbf{k}}) + \sum_{\mathbf{k} \in \Lambda} \sum_{\mathbf{l} \in \eta_{\mathbf{k}}, C \in \mathcal{C}_2} V_C(x_{\mathbf{k}}, x_{\mathbf{l}}), \quad (5.1)$$

where V_C are known as the **clique potentials**.

A random field \mathbf{X} is called a **Markov Random Field (MRF)** on the lattice Λ with respect to a neighborhood system η if it satisfies the following conditions:

- $\mathbb{P}(\mathbf{X} = \mathbf{x}) > 0$, for all $\mathbf{x} \in \mathcal{A}^{N_T}$, and
- $\mathbb{P}(X_{\mathbf{k}} = x_{\mathbf{k}} \mid X_{\mathbf{l}} = x_{\mathbf{l}}, \forall \mathbf{l} \in \Lambda \setminus \mathbf{k}) = \mathbb{P}(X_{\mathbf{k}} = x_{\mathbf{k}} \mid X_{\mathbf{l}} = x_{\mathbf{l}}, \forall \mathbf{l} \in \eta_{\mathbf{k}})$.

The **local characteristic** at node \mathbf{k} is the function $\pi^{\mathbf{k}} : \mathcal{A}^{N_T} \rightarrow [0, 1]$ defined by

$$\pi^{\mathbf{k}}(\mathbf{x}) = \mathbb{P}(X_{\mathbf{k}} = x_{\mathbf{k}} \mid X_{\mathbf{l}} = x_{\mathbf{l}} \forall \mathbf{l} \in \eta_{\mathbf{k}}).$$

The family $\{\pi^{\mathbf{k}}\}_{\mathbf{k} \in \Lambda}$ is called the **local specification** of the MRF.

An MRF is characterized by its local property, (the conditional probability density at a node given its neighbors) while a GRF is characterized by its global property (the Gibbs distribution). The **Hammersley-Clifford theorem** (see e.g. [51]) states that a

random field is a GRF if and only if it is an MRF. Thus, it gives us the flexibility of designing an MRF using local or global properties depending on their availability for a specific application.

5.2.2 Gaussian Markov Random Field

A special class of MRF arises from the following clique potentials:

$$V_C(x_{\mathbf{k}}) = \frac{(x_{\mathbf{k}} - \mu_{\mathbf{k}})^2}{2\sigma^2}, \forall C \in \mathcal{C}_1,$$

and

$$V_C(x_{\mathbf{k}}, x_{\mathbf{l}}) = -\theta_{\mathbf{k},\mathbf{l}} \frac{(x_{\mathbf{k}} - \mu_{\mathbf{k}})(x_{\mathbf{l}} - \mu_{\mathbf{l}})}{\sigma^2}, \mathbf{l} \in \eta_{\mathbf{k}}, \forall C \in \mathcal{C}_2,$$

where $\mu_{\mathbf{k}}$ determines the mean at node \mathbf{k} , and as we shall see shortly, $\theta_{\mathbf{k},\mathbf{l}}$ are parameters related to the covariance matrix of the random field. Substituting these clique potentials in (5.1) we obtain,

$$U(\mathbf{x}) = \frac{1}{2\sigma^2} \sum_{\mathbf{k} \in \Lambda} (x_{\mathbf{k}} - \mu_{\mathbf{k}})^2 - \frac{1}{\sigma^2} \sum_{\mathbf{k} \in \Lambda} \sum_{\mathbf{l} \in \eta_{\mathbf{k}}} (x_{\mathbf{k}} - \mu_{\mathbf{k}})\theta_{\mathbf{k},\mathbf{l}}(x_{\mathbf{l}} - \mu_{\mathbf{l}}).$$

We now assume that the alphabet is \mathbb{R} . Thus, the joint probability density of all N_T nodes in Λ is given by:

$$p(\mathbf{x}) = \frac{\sqrt{\det(\mathbf{B})}}{\sqrt{(2\pi\sigma^2)^{N_T}}} \exp \left[-\frac{(\mathbf{x} - \boldsymbol{\mu})^T \mathbf{B} (\mathbf{x} - \boldsymbol{\mu})}{2\sigma^2} \right], \quad (5.2)$$

where $\boldsymbol{\mu}$ is an $N_T \times 1$ vector of means and $\mathbf{B} = [b_{\mathbf{l}\mathbf{k}}]$ is the following $N_T \times N_T$ matrix:

$$b_{\mathbf{l}\mathbf{k}} = \begin{cases} 1, & \text{if } \mathbf{l} = \mathbf{k}, \\ -\theta_{\mathbf{l},\mathbf{k}}, & \text{if } \mathbf{l} \in \eta_{\mathbf{k}}, \\ 0, & \text{else.} \end{cases} \quad (5.3)$$

The function in Equation (5.2) is the joint probability density function of a multivariate Gaussian distribution with covariance matrix $\Sigma = \sigma^2 \mathbf{B}^{-1}$ and mean vector $\boldsymbol{\mu}$. Hence, this random field is referred to as a Gaussian Markov Random Field. The necessary and sufficient condition for p defined in Equation (5.2) to be a density function is that \mathbf{B} is a positive matrix. The Markov property now reads

$$\mathbb{P}(X_{\mathbf{k}} \in A \mid X_{\mathbf{l}}, \forall \mathbf{l} \in \boldsymbol{\Lambda} \setminus \mathbf{k}) = \mathbb{P}(X_{\mathbf{k}} \in A \mid X_{\mathbf{l}}, \forall \mathbf{l} \in \eta_{\mathbf{k}}), \forall A \subset \mathbb{R}.$$

This is true because the conditional probability density $p(x_{\mathbf{k}} \mid x_{\mathbf{l}}, \mathbf{l} \in \boldsymbol{\Lambda} \setminus \mathbf{k})$ is given by [93]:

$$\begin{aligned} p(x_{\mathbf{k}} \mid x_{\mathbf{l}}, \mathbf{l} \in \boldsymbol{\Lambda} \setminus \mathbf{k}) &= p(x_{\mathbf{k}} \mid x_{\mathbf{l}}, \mathbf{l} \in \eta_{\mathbf{k}}) \\ &= \frac{1}{\sqrt{2\pi\sigma^2}} \exp \left[-\frac{1}{2\sigma^2} \left(x_{\mathbf{k}} - \mu_{\mathbf{k}} - \sum_{\mathbf{l} \in \eta_{\mathbf{k}}} \theta_{\mathbf{k},\mathbf{l}}(x_{\mathbf{l}} - \mu_{\mathbf{l}}) \right)^2 \right]. \end{aligned} \quad (5.4)$$

The conditional distribution corresponding to this density is referred to as the local characteristic at node \mathbf{k} for the continuous alphabet case. This conditional distribution is defined in the sense of regular conditional probability (see Theorem V.8.1 in [90]). Now, the gray level at the node \mathbf{k} can be expressed as a linear combination of the gray levels at the neighboring nodes:

$$x_{\mathbf{k}} = \mu_{\mathbf{k}} + \sum_{\mathbf{l} \in \eta_{\mathbf{k}}} \theta_{\mathbf{k},\mathbf{l}}(x_{\mathbf{l}} - \mu_{\mathbf{l}}) + e_{\mathbf{k}}, \quad (5.5)$$

where the correlated Gaussian noise, $\mathbf{e} = (e_1, \dots, e_{N_T})$, has the following structure:

$$\mathbb{E}[e_{\mathbf{k}}e_{\mathbf{l}}] = \begin{cases} \sigma^2, & \mathbf{k} = \mathbf{l}, \\ -\theta_{\mathbf{k},\mathbf{l}}\sigma^2, & \mathbf{l} \in \eta_{\mathbf{k}}, \\ 0, & \text{else.} \end{cases} \quad (5.6)$$

In [25, 65], Equations (5.5) and (5.6) are used to define GMRF. This model is referred to as Conditional Markov (CM) model in [65] where the various parameter estimation schemes for this model are discussed. Also contained in [65] is a discussion on the choice of neighbors.

For models that we use, we assume the following spatial symmetry for the parameters θ :

$$\theta_{\mathbf{k},\mathbf{l}} = \theta_{\mathbf{k},-\mathbf{l}}. \quad (5.7)$$

Hence, the neighborhoods must be defined so that $\mathbf{l} \in \eta_{\mathbf{k}} \Rightarrow -\mathbf{l} \in \eta_{\mathbf{k}}$. We also assume the stationarity of the model. Hence, $\theta_{\mathbf{k},\mathbf{l}}$ only depends on $\mathbf{k} - \mathbf{l}$ and the neighborhood $\eta_{\mathbf{k}}$ has the same structure at each \mathbf{k} . By the same structure we mean that the set $\{\mathbf{k} - \mathbf{l}\}_{\mathbf{l} \in \eta_{\mathbf{k}}}$ is the same for all \mathbf{k} . This set is denoted by η . Similarly, the mean, $\mu_{\mathbf{k}}$ is also constant across all the nodes and hence we drop the subscript \mathbf{k} and denote the mean by μ . Due to the symmetry assumed in Equation (5.7), if $\mathbf{r} \in \eta$ then $-\mathbf{r}$ is also in η . We use η^+ to denote half of the elements of η such that only one of \mathbf{r} or $-\mathbf{r}$ is in η^+ . For instance, in the 2-D case, if $\eta = \{(1, 0), (0, 1), (-1, 0), (0, -1)\}$ then $\eta^+ = \{(1, 0), (0, 1)\}$. Thus, for the stationary case, Equation (5.5) takes the following form

$$x_{\mathbf{k}} = \mu + \sum_{\mathbf{r} \in \eta^+} \theta_{\mathbf{r}}(x_{\mathbf{k}-\mathbf{r}} + x_{\mathbf{k}+\mathbf{r}} - 2\mu) + e_{\mathbf{k}}. \quad (5.8)$$

The vector of parameters $[\theta_{\mathbf{r}}, \mathbf{r} \in \eta^+]$ is denoted by $\boldsymbol{\theta}$.

In the rest of the discussion we assume that $\mu = 0$, unless otherwise mentioned.

5.2.3 Parameter Estimation

Chellappa and Kashyap discuss various parameter estimation schemes in [25, 65]. These, amongst others, include a Maximum likelihood scheme, a coding scheme due to Besag and Least squares (LS). The ML-estimates have good statistical properties but are expensive to compute because they require numerical optimization techniques. We follow the LS estimation scheme given in Section 4.3 of [25]. The statistical properties of this scheme are analyzed in [65]. For a given realization \mathbf{x} , the estimates are given by the following

statistics:

$$\widehat{\boldsymbol{\theta}}(\mathbf{x}) = (\mathbf{Y}^T \mathbf{Y})^{-1} \mathbf{Y}^T \mathbf{x}, \quad (5.9)$$

$$\widehat{\sigma^2}(\mathbf{x}) = \frac{1}{N_T} (\mathbf{x} - \mathbf{Y} \widehat{\boldsymbol{\theta}})^T (\mathbf{x} - \mathbf{Y} \widehat{\boldsymbol{\theta}}), \quad (5.10)$$

where $\mathbf{Y} = [\mathbf{y}_{\mathbf{r}}]$, $\mathbf{r} \in \mathbf{A}$ and $\mathbf{y}_{\mathbf{r}} = [x_{\mathbf{l}} + x_{-\mathbf{l}}, \mathbf{l} \in \eta_{\mathbf{r}}^+]$. Thus, if m is the size of the half-neighborhood $\eta_{\mathbf{r}}^+$ then \mathbf{Y} is a $N_T \times m$ matrix. For a derivation of these equations see Appendix B of [93]. Using the estimate, $\widehat{\boldsymbol{\theta}}$, from (5.9), the expression for estimate of σ^2 reduces to

$$\widehat{\sigma^2}(\mathbf{x}) = \frac{1}{N_T} (\mathbf{x}^T \mathbf{x} - \widehat{\boldsymbol{\theta}}^T \mathbf{Y}^T \mathbf{x}). \quad (5.11)$$

A sufficient condition on $\boldsymbol{\theta}$ for the corresponding $\mathbf{B}(\boldsymbol{\theta})$ (see Equation (5.3)) to be a positive matrix is $|\boldsymbol{\theta}| < 0.5$ [72]. Here, $|\boldsymbol{\theta}|$ denotes the ℓ^1 -norm of the vector $\boldsymbol{\theta}$. As shown in [72], in general, this sufficient condition only represents a subset of the valid parameter space for $\boldsymbol{\theta}$. But, in the case of order one neighborhood, this is also a necessary condition.

In the light of Equation (5.9) and the constraint on $\boldsymbol{\theta}$ for order one neighborhood, we have to solve the following constrained optimization problem to estimate $\boldsymbol{\theta}$:

Find

$$\min_{\boldsymbol{\theta}} \|\mathbf{Y}^T \mathbf{Y} \boldsymbol{\theta} - \mathbf{Y}^T \mathbf{x}\|_2,$$

subject to,

$$\sum_{i=1}^3 |\theta_i| < 0.5.$$

The entries of the matrix $\mathbf{Y}^T \mathbf{Y}$ and the vector $\mathbf{Y}^T \mathbf{x}$ can be calculated from the auto-covariance function of \mathbf{x} . This will facilitate fast calculation of the rotationally invariant distance defined in Section 5.3. For a stationary random process \mathbf{X} on \mathbb{Z}^3 , the auto-covariance function is given by

$$\rho(\mathbf{l}) = \mathbb{E}[\mathbf{X}(\mathbf{l})\mathbf{X}(0)].$$

In particular, for a infinite extent GMRF whose local specifications are given by (5.4), the auto-covariance function ρ decays to zero as $|\mathbf{l}|$ goes to ∞ . This is due to the fact that the power spectral density $\hat{\rho}$ is the inverse of a positive trigonometric polynomial.

Due to the ergodicity (implicit in the model, see Theorem III.4.4 in [7]), the auto-covariance function, ρ , can be approximated by

$$\rho_0(\mathbf{l}) = \frac{1}{N_T} \sum_{\mathbf{r} \in \Lambda} x_{\mathbf{r}} x_{\mathbf{r}+\mathbf{l}}, \quad \text{for all } \mathbf{l} \in \Lambda, \quad (5.12)$$

for a sufficiently large N_T . Using the Discrete Fourier Transform, we obtain

$$\hat{\rho}_0(\mathbf{k}) = \widehat{\mathbf{x}}(\mathbf{k}) \overline{\widehat{\mathbf{x}}(\mathbf{k})} = |\widehat{\mathbf{x}}(\mathbf{k})|^2 \quad \text{for all } \mathbf{k} \in \Lambda', \quad (5.13)$$

where Λ' is a grid of \mathbb{T}^3 , similar to Λ . Note that those values of $\hat{\rho}_0$ give an approximation of the power spectral density $\hat{\rho}$ defined on \mathbb{T}^3 , at the grid points Λ' . Equation (5.13) facilitates efficient calculation of ρ_0 via FFT. Now, the entries of the vector $\mathbf{Y}^T \mathbf{x}$ are expressed in terms of ρ_0 as follows:

$$\begin{aligned} (\mathbf{Y}^T \mathbf{x})_{\mathbf{r}} &= \sum_{\mathbf{l} \in \Lambda} x_{\mathbf{l}} (x_{\mathbf{l}+\mathbf{r}} + x_{\mathbf{l}-\mathbf{r}}) \\ &= N_T (\rho_0(\mathbf{r}) + \rho_0(-\mathbf{r})), \end{aligned}$$

for each $\mathbf{r} \in \eta^+$. Similarly, the entries of the matrix $\mathbf{Y}^T \mathbf{Y}$ are given by

$$\begin{aligned} (\mathbf{Y}^T \mathbf{Y})_{(\mathbf{k}, \mathbf{r})} &= \sum_{\mathbf{l} \in \Lambda} (x_{\mathbf{l}+\mathbf{k}} + x_{\mathbf{l}-\mathbf{k}}) (x_{\mathbf{l}+\mathbf{r}} + x_{\mathbf{l}-\mathbf{r}}) \\ &= N_T (\rho_0(\mathbf{r} - \mathbf{k}) + \rho_0(\mathbf{r} + \mathbf{k}) + \rho_0(-\mathbf{r} - \mathbf{k}) + \rho_0(-\mathbf{r} + \mathbf{k})), \end{aligned}$$

for each $(\mathbf{k}, \mathbf{r}) \in \eta^+ \times \eta^+$. Thus, for any given zero mean discrete texture \mathbf{x} , that is not necessarily a GMRF, we can calculate the ρ_0 using (5.12). Then we can estimate the parameters for a GMRF with neighborhood of order one using the above equations. *We refer to the model with these parameters as the GMRF fitted to the texture \mathbf{x} .*

5.2.4 Synthesizing a GMRF

Next, we briefly discuss the algorithm for sampling a stationary GMRF with toroidal boundaries. For a fixed neighborhood structure $\boldsymbol{\eta}$ and known parameters, $\theta_{\mathbf{k},\mathbf{l}}, \boldsymbol{\mu}, \sigma$, we can write Equation (5.5) as:

$$\mathbf{B}(\mathbf{x} - \boldsymbol{\mu}) = \mathbf{e}.$$

where \mathbf{e} is a zero mean Gaussian noise sequence with the covariance structure defined in (5.6). This noise sequence can be written as

$$\mathbf{e} = \sqrt{\mathbf{B}}\mathbf{e}_0,$$

where \mathbf{e}_0 is a zero mean Gaussian noise sequence with covariance matrix given by σ^2 times the identity. This is easily generated with a standard random number generator in MATLAB. Hence, a realization of \mathbf{X} is obtained via

$$\mathbf{x} = \mathbf{B}^{-1}\sqrt{\mathbf{B}}\mathbf{e}_0 + \boldsymbol{\mu} = \mathbf{B}^{\frac{-1}{2}}\mathbf{e}_0 + \boldsymbol{\mu}.$$

The stationarity assumption implies that $\mu_{\mathbf{k}} = \mu, \forall \mathbf{k} \in \boldsymbol{\Lambda}$ and that $\theta_{\mathbf{k},\mathbf{l}}$ only depends on the difference $\mathbf{k} - \mathbf{l}$. This along with the toroidal boundary condition makes \mathbf{B} a block circulant matrix which can be inverted efficiently using FFT. For details of this algorithm and block circulant matrices, see [93], Chapter 4.

5.3 Rotationally Invariant Distance

Now, to obtain a rotationally invariant texture distance, we begin by defining a texture signature. We use a neighborhood of order one, $\eta^+ = \{(1, 0, 0), (0, 1, 0), (0, 0, 1)\}$. Thus, $\boldsymbol{\theta}$ is a three-dimensional vector. Recall that for a given texture \mathbf{x} , $\widehat{\boldsymbol{\theta}}(\mathbf{x})$ and $\widehat{\sigma^2}(\mathbf{x})$, denote

the parameters of the GMRF fitted to \mathbf{x} . We define the texture signature $\Gamma_{\mathbf{x}}$, via

$$\Gamma_{\mathbf{x}}(\boldsymbol{\alpha}) = \left[\widehat{\boldsymbol{\theta}}(\mathcal{R}_{\boldsymbol{\alpha}}\mathbf{x}), \widehat{\sigma^2}(\mathcal{R}_{\boldsymbol{\alpha}}\mathbf{x}) \right], \quad (5.14)$$

for all $R_{\boldsymbol{\alpha}} \in SO(3)$, where $\boldsymbol{\alpha} = (\alpha, \beta, \gamma)$ is the Euler angle parametrization for the rotation $R_{\boldsymbol{\alpha}}$ (see Equation (5.22) below), and $\mathcal{R}_{\boldsymbol{\alpha}}$ is the rotation operator induced by $R_{\boldsymbol{\alpha}}$ on $L^2(\mathbb{R}^3)$. Notice the abuse of notation when we write $\mathcal{R}_{\boldsymbol{\alpha}}\mathbf{x}$, since \mathbf{x} is not defined on \mathbb{R}^3 but on $\boldsymbol{\Lambda}$, which is a finite sub-lattice of \mathbb{Z}^3 . For now, just think of \mathbf{x} as samples of some continuous infinite extent texture, \mathbf{x}_{cont} , and then $\mathcal{R}_{\boldsymbol{\alpha}}\mathbf{x}$ denotes the samples of $\mathcal{R}_{\boldsymbol{\alpha}}\mathbf{x}_{cont}$ on $\boldsymbol{\Lambda}$. This idea of rotating and resampling the texture will be made more precise in Section 5.3.2.

Now, we define a distance between two textures by the following expression:

$$\min_{\boldsymbol{\alpha}_0 \in SO(3)} \int_{SO(3)} \text{KLdist}(\Gamma_{\mathbf{x}_1}(\boldsymbol{\alpha}), \Gamma_{\mathbf{x}_2}(\boldsymbol{\alpha}\boldsymbol{\alpha}_0)) d\boldsymbol{\alpha}, \quad (5.15)$$

where $\text{KLdist}(\cdot, \cdot)$ is the KL-distance between two Gaussian densities defined in Equation (5.19), and the product $\boldsymbol{\alpha}\boldsymbol{\alpha}_0$ denotes the Euler angles corresponding to the rotation operator $\mathcal{R}_{\boldsymbol{\alpha}}\mathcal{R}_{\boldsymbol{\alpha}_0}$. The integration is carried out with respect to the Haar measure on $SO(3)$. For the Euler angle parametrization of $SO(3)$ with the *ZYZ*-convention (see Equation (5.22) below), the Haar measure is given by (See Chapter 5 of [27]),

$$d\boldsymbol{\alpha} = \sin(\beta)d\alpha d\beta d\gamma, \quad (5.16)$$

where $d\alpha$, $d\beta$ and $d\gamma$ stand for the Lebesgue measure. The Haar measure is usually normalized by $\frac{1}{8\pi^2}$.

5.3.1 KL-distance Between two Gaussian Markov Random Fields

The Kullback-Leibler distance between two N -dimensional probability distributions with joint probability density functions p_1 and p_2 is given by

$$D(p_2||p_1) = \int_{\mathbb{R}^N} p_2(\mathbf{x}) \log_e \left(\frac{p_2(\mathbf{x})}{p_1(\mathbf{x})} \right) d\mathbf{x}. \quad (5.17)$$

The joint probability density function (p.d.f) of a multivariate Gaussian distribution with covariance matrix Σ and mean vector $\boldsymbol{\mu}$ is given by

$$p(\mathbf{x}) = \frac{1}{\sqrt{(2\pi)^N \det(\Sigma)}} \exp \left[-\frac{(\mathbf{x} - \boldsymbol{\mu})^T \Sigma^{-1} (\mathbf{x} - \boldsymbol{\mu})}{2} \right]. \quad (5.18)$$

Now suppose, we have two N -dimensional Gaussian probability density functions, p_1 and p_2 , with means $\boldsymbol{\mu}_1$ and $\boldsymbol{\mu}_2$, and covariance matrices Σ_1 and Σ_2 respectively. Then substituting the formulae for p_1 and p_2 in (5.17) yields the following expression for the KL-distance between two Gaussian distributions:

$$\frac{1}{2} \log_e \left(\frac{\det \Sigma_1}{\det \Sigma_2} \right) + \frac{1}{2} (\boldsymbol{\mu}_2 - \boldsymbol{\mu}_1)^T \Sigma_1^{-1} (\boldsymbol{\mu}_2 - \boldsymbol{\mu}_1) + \frac{1}{2} \text{Trace}(\Sigma_1^{-1} \Sigma_2) - \frac{N}{2}.$$

Note that the distance defined above is not symmetric. Hence, if we exchange Σ_1 and Σ_2 , we get another expression:

$$\frac{1}{2} \log_e \left(\frac{\det \Sigma_2}{\det \Sigma_1} \right) + \frac{1}{2} (\boldsymbol{\mu}_1 - \boldsymbol{\mu}_2)^T \Sigma_2^{-1} (\boldsymbol{\mu}_1 - \boldsymbol{\mu}_2) + \frac{1}{2} \text{Trace}(\Sigma_2^{-1} \Sigma_1) - \frac{N}{2}.$$

Adding these two expressions yields the following expression, which is symmetric:

$$\frac{1}{2} (\boldsymbol{\mu}_1 - \boldsymbol{\mu}_2)^T (\Sigma_2^{-1} + \Sigma_1^{-1}) (\boldsymbol{\mu}_1 - \boldsymbol{\mu}_2) + \frac{1}{2} \text{Trace}(\Sigma_2^{-1} \Sigma_1 + \Sigma_1^{-1} \Sigma_2) - N.$$

Assuming zero means for both the p.d.fs, we conclude that the KL-distance between two Gaussian distributions is:

$$\frac{1}{2} \text{Trace}(\Sigma_2^{-1} \Sigma_1 + \Sigma_1^{-1} \Sigma_2 - 2I_{N \times N}). \quad (5.19)$$

Since in our case, Σ_1 and Σ_2 are block circulant, (5.19) can be calculated efficiently using FFT.

5.3.2 Rotation of Textures

As pointed out in the introduction of this chapter, rotating a discrete texture is not well-defined. Hence, we define a continuous counterpart of the discrete texture we wish to rotate. We model a continuous texture as a realization of a stationary Gaussian random field, \mathbf{X}_{cont} , on \mathbb{R}^3 with a square integrable autocovariance function. We assume that the texture remains invariant under rotation by π about any line passing through the origin. This is consistent with the symmetry assumptions for the discrete texture. We further assume that the autocovariance function of a texture, ρ_{cont} , belongs to the zero resolution space, V_0 , of the IMRA described in Example 3.2.1. Recall that V_0 is the closed linear span of the set $\{T_{\mathbf{k}}\phi\}_{\mathbf{k}\in\mathbb{Z}^3}$. This assumption implies that the power spectral density is compactly supported, inside a radial set. Thus, its support remains invariant under all rotations. Hence, the autocovariance function remains in the same resolution space after rotation and can therefore be sampled at the same sampling rate. This is the advantage of assuming that ρ_{cont} belongs to V_0 .

The sequence of coefficients $\{\langle\rho_{cont}, T_{\mathbf{k}}\phi\rangle\}_{\mathbf{k}\in\mathbb{Z}^3}$ is denoted by ρ . This sequence can be considered as the samples of ρ_{cont} on \mathbb{Z}^3 . In fact, if we assume that the power spectral density $\widehat{\rho_{cont}}$ is supported on the ball $B(0, 2b_1)$ where $\widehat{\phi}$ is equal to one, then $\langle\rho_{cont}, T_{\mathbf{k}}\phi\rangle = \rho_{cont}(\mathbf{k})$ and $\rho_{cont} = \sum_{\mathbf{k}\in\mathbb{Z}^3} \rho_{cont}(\mathbf{k})T_{\mathbf{k}}\phi$.

Next, observe that the autocovariance function of $\mathcal{R}_{\boldsymbol{\alpha}}\mathbf{X}_{cont}$ is given by $\mathcal{R}_{\boldsymbol{\alpha}}\rho_{cont}$:

$$\begin{aligned} \mathbb{E}[\mathcal{R}_{\boldsymbol{\alpha}}\mathbf{X}_{cont}(\mathbf{s})\mathcal{R}_{\boldsymbol{\alpha}}\mathbf{X}_{cont}(0)] &= \mathbb{E}[\mathbf{X}_{cont}(R_{\boldsymbol{\alpha}}^T\mathbf{s})\mathbf{X}_{cont}((R_{\boldsymbol{\alpha}}^T)0)] \\ &= \rho_{cont}(R_{\boldsymbol{\alpha}}^T\mathbf{s}) = \mathcal{R}_{\boldsymbol{\alpha}}\rho_{cont}(\mathbf{s}). \end{aligned} \quad (5.20)$$

Now, since we assumed that $\widehat{\rho_{cont}}$ is supported on the ball $B(0, 2b_1)$, $\mathcal{R}_{\boldsymbol{\alpha}}\rho_{cont}$ is also supported on the same ball. With a slight abuse of notation, the sequence of samples,

$\{\langle \mathcal{R}_\alpha \rho_{cont}, T_{\mathbf{k}} \phi \rangle\}_{\mathbf{k} \in \mathbb{Z}^3}$ is denoted by $\mathcal{R}_\alpha \rho$. Also note that

$$\rho_{cont}(\mathbf{k}) = \mathbb{E}[\mathbf{X}_{cont}(\mathbf{k})\mathbf{X}_{cont}(0)] = \mathbb{E}[\mathbf{X}(\mathbf{k})\mathbf{X}(0)],$$

i.e., the autocovariance function of \mathbf{X} , the samples of \mathbf{X}_{cont} on \mathbb{Z}^3 , is ρ .

Given a realization \mathbf{x} of a discrete texture \mathbf{X} on the finite lattice Λ , we can calculate ρ_0 corresponding to \mathbf{x} using (5.12). As pointed out in Section 5.2.3 this is an approximation for ρ on Λ if Λ is sufficiently big. Assuming that the values of ρ are negligible on $\mathbb{Z}^3 \setminus \Lambda$, the parameters of the GMRF model fitted to the ‘rotated texture’ denoted by $\mathcal{R}_\alpha \mathbf{x}$ can be calculated using $\mathcal{R}_\alpha \rho$. This formalizes the idea of a ‘discrete’ rotation that we had alluded to in Section 5.3. This is an excellent example of how MRAs in general and IMRA in particular act as a bridge between the digital or discrete, and the analog or continuous domains. We make sense of a discrete rotation by first converting to the analog domain via the IMRA, rotating in the analog domain, where rotations are well defined, and finally, converting back to the discrete domain via sampling.

In principle, we can calculate the sequence $\{\langle \mathcal{R}_\alpha \rho_{cont}, T_{\mathbf{k}} \phi \rangle\}_{\mathbf{k} \in \mathbb{Z}^3}$ exactly, but that is computationally very expensive. Instead, we resample ρ on a finer grid using the IMRA. This works by performing one or more steps of the reconstruction algorithm described in Section 3.3, assuming that the detail or high-pass component is zero at each reconstruction step. If we use dyadic dilation, for example, then one step of the reconstruction gives the coefficients $\left\{ \left\langle \rho_{cont}, T_{\frac{\mathbf{k}}{2}} D \phi \right\rangle \right\}_{\mathbf{k} \in \mathbb{Z}^3}$. These can be considered as the samples of the covariance function on the denser grid $\frac{\mathbb{Z}^3}{2}$. We then rotate this covariance function defined on a denser grid by using linear interpolation to get the values at grid points that do not lie on the integer lattice after rotation. This is not exact but the error can be made smaller by resampling on a finer grid. In practice we see that just one or two steps of the reconstruction algorithm are enough to give good results. This is demonstrated in

Section 5.4, where we discuss the results from our experimental study.

5.3.3 Practical Implementation of the Distance

For the practical implementation of the distance defined in Equation (5.15), we must discretize the integral over α . To this end, we discretize the ZYZ -Euler angles. First, note that, due the symmetries in the model, it is enough to restrict the Euler angles to the following domains:

$$0 \leq \alpha \leq \pi, \quad 0 \leq \beta \leq \frac{\pi}{2}, \quad 0 \leq \gamma \leq \pi. \quad (5.21)$$

To prove this, recall that our model is invariant under a rotation by π about any line passing through the origin. Using the ZYZ -convention, the rotation R_{α} is defined by:

$$R_{\alpha} = R_Z(\gamma)R_Y(\beta)R_Z(\alpha), \quad (5.22)$$

where $R_Z(\alpha)$ and $R_Y(\alpha)$ denote rotation by α about the Z -axis and Y -axis respectively,

$$R_Z(\alpha) = \begin{bmatrix} \cos(\alpha) & -\sin(\alpha) & 0 \\ \sin(\alpha) & \cos(\alpha) & 0 \\ 0 & 0 & 1 \end{bmatrix}, \quad R_Y(\alpha) = \begin{bmatrix} \cos(\alpha) & 0 & -\sin(\alpha) \\ 0 & 1 & 0 \\ \sin(\alpha) & 0 & \cos(\alpha) \end{bmatrix}.$$

Now, suppose $\alpha = a + \pi$, where $0 < a < \pi$ and $0 \leq \beta \leq \frac{\pi}{2}$, $0 \leq \gamma \leq \pi$, then the corresponding rotation, R_{α} , is given by

$$R_{\alpha} = R_{\alpha_1}R_Z(\pi),$$

where $\alpha_1 = (a, \beta, \gamma)$. Since, our model is invariant under rotation by $R_Z(\pi)$, we infer that it is enough to restrict α to $[0, \pi]$. Similar calculations show that γ can be restricted to $[0, \pi]$ as well. To see that it is enough to restrict β between $[0, \frac{\pi}{2}]$, consider $\alpha = (a, a + \pi/2, \gamma)$, where $0 < a < \frac{\pi}{2}$. Then, we have,

$$R_{\alpha} = R_Z(\gamma)R_Y\left(a + \frac{\pi}{2}\right)R_Z(\alpha).$$

Again, because of the symmetry properties of our texture, $R_Y(a + \frac{\pi}{2})$ can be replaced by $R_Y(a + \frac{3\pi}{2})$, because this corresponds to a rotation by π about the new Y -axis after the texture has been rotated by $R_Z(\alpha)$. It is easy to check that

$$R_Y\left(a + \frac{3\pi}{2}\right) = R_Z(\pi)R_Y\left(\frac{\pi}{2} - a\right)R_Z(\pi).$$

Since, $\frac{\pi}{2} - a$ lies in $[0, \frac{\pi}{2}]$, we conclude that it is enough to restrict β in $[0, \frac{\pi}{2}]$.

Now, we are ready to discretize the integral in (5.15). We take points spaced uniformly with respect to the Haar measure defined in Equation (5.16). This is done by taking equally spaced points on the interval $[0, \pi]$ for both α and γ . Hence, the discrete sets of parameters are given by $\alpha_i = \{\frac{i\pi}{N_\alpha}\}$ for $i = 0, 1, \dots, N_\alpha - 1$, and $\gamma_i = \{\frac{i\pi}{N_\gamma}\}$ for $i = 0, 1, \dots, N_\gamma - 1$. For β , we take the discrete set $\beta_i = \{\arccos(1 - \frac{i+0.5}{N_\beta})\}$, for $i = 0, 1, \dots, N_\beta - 1$. Notice that we take the discrete values of β starting with 0.5, this is done to avoid β_0 from being equal to zero. If $\beta_0 = 0$, we get into a situation referred to as *gimbal lock*. In that case, only $\alpha + \gamma$ is uniquely determined. Hence, we offset by 0.5 to avoid duplicating rotations in our discrete set. For more information, and a nice illustration of why this situation is called gimbal lock, visit the following web-page.

http://en.wikipedia.org/wiki/Euler_angles

Using the above discrete set of rotations, a practically implementable version of the distance defined in Equation (5.15) is given by

$$\min_{\alpha_0 \in SO(3)} \frac{1}{N_\alpha N_\beta N_\gamma} \sum_{i=0}^{N_\alpha-1} \sum_{j=0}^{N_\beta-1} \sum_{k=0}^{N_\gamma-1} \text{KLdist}(\Gamma(\alpha_{(i,j,k)}), \Gamma(\alpha_{(i,j,k)}\alpha_0)), \quad (5.23)$$

where $\alpha_{i,j,k} = (\alpha_i, \beta_j, \gamma_k)$ and as before, the product $\alpha_{i,j,k}\alpha_0$ represents the Euler angles corresponding the rotation operator $\mathcal{R}_{\alpha_{i,j,k}}\mathcal{R}_{\alpha_0}$. For actual experiments, the minimization can be carried out on a subset of $SO(3)$ corresponding to the Euler angles described by (5.21) because of the symmetries present in the model.

5.4 Experimental Results

To test the ideas developed so far, we generate synthetic volumes arising from 3-*D* GMRF models which we synthesize using the algorithm described in Section 5.2.4. We use the MATLAB function `patternsearch` to solve the minimization problem which is required to calculate the distance defined in Equation (5.23). The number of discrete angles are taken to be $N_\alpha = N_\beta = N_\gamma = 5$. This gives a total of 125 rotations sampled uniformly with respect to the Haar measure on $SO(3)$. Thus, each evaluation of the function to be minimized in Equation (5.23) requires the calculation of 125 sets of parameters and the calculation of 125 K-L distances. On a 2.8 GHz machine each evaluation of the function takes about three-quarters of a second. The MATLAB routine mentioned above is particularly useful because it does not calculate derivatives and thus, each iteration of the algorithm requires very few evaluations of the function to be minimized. The details of this routine can be found in the MATLAB documentation on the web-page of Mathworks. We do not intend to study this optimization algorithm here. We just use it as a black-box and it works well for the calculation of the rotationally invariant distance. It takes about one minute to calculate the distance between two texture signatures.

For our first set of experiments, we generate two distinct synthetic textures, denoted by \mathcal{T}_1 and \mathcal{T}_2 , that have the same conditional variance, $\sigma^2 = 1$, and mean, $\mu = 0$. We use the first order neighborhood to generate these textures using the parameters $\boldsymbol{\theta} = (\theta_x, \theta_y, \theta_z)$ shown in Table 5.1. We make this choice to test the real potential of this method. If we generate synthetic textures with neighborhoods larger than those of order one, then we do not have control over the conditional variance of the GMRF of order one fitted to those textures. In fact, as we show in another set of experiments described below, a few textures that we generated with higher order neighborhoods could be discriminated based on the

5.4. EXPERIMENTAL RESULTS

value of σ^2 corresponding to the order one GMRF fitted to these textures. If the estimate for σ^2 itself is enough to discriminate between textures then we do not have to look at $\boldsymbol{\theta}$. Hence, for our first set of experiments we stick with the synthetic textures obtained from order one GMRFs with equal conditional variance. We denote \mathcal{T}_1 by $\mathcal{T}_{1,0}$ while $\mathcal{T}_{1,\frac{\pi}{2}}$

	$\mathcal{T}_{1,0}$	$\mathcal{T}_{1,\frac{\pi}{2}}$	$\mathcal{T}_{2,0}$	$\mathcal{T}_{2,\frac{\pi}{2}}$
θ_x	0.1	0.1	0.05	0.20
θ_y	0.1	0.25	0.15	0.15
θ_z	0.25	0.1	0.20	0.05
σ^2	1.0	1.0	1.0	1.0

Table 5.1: Parameters for synthetic textures used for experimental study.

denotes the texture $\mathcal{T}_{1,0}$ rotated about the X -axis by $\frac{\pi}{2}$. Similarly, $\mathcal{T}_{2,0}$ denotes the texture \mathcal{T}_2 while $\mathcal{T}_{2,\frac{\pi}{2}}$ denotes the texture $\mathcal{T}_{2,0}$ rotated about the Y -axis by $\frac{\pi}{2}$. Thus, we expect the distances between $\mathcal{T}_{1,0}$ and $\mathcal{T}_{1,\frac{\pi}{2}}$, and between $\mathcal{T}_{2,0}$ and $\mathcal{T}_{2,\frac{\pi}{2}}$ to be small, while we want both $\mathcal{T}_{1,0}$ and $\mathcal{T}_{1,\frac{\pi}{2}}$ to have a large distance from both $\mathcal{T}_{2,0}$ and $\mathcal{T}_{2,\frac{\pi}{2}}$.

In Tables 5.2, 5.3 and 5.4, we tabulate the distance of a realization of each of the four textures (two rotations of two distinct textures) given in Table 5.1 from another realization of each of these textures, for different upsampling factors. The diagonal entries in the tables correspond to the distance between two realizations of the same texture while the off-diagonal entries correspond to the distance between realizations of two different textures. We notice that in Tables 5.2 and 5.3, the distance between $\mathcal{T}_{1,0}$ and $\mathcal{T}_{1,\frac{\pi}{2}}$ is of the order of the distance between two realizations of $\mathcal{T}_{1,0}$ or $\mathcal{T}_{1,\frac{\pi}{2}}$. Same is true for $\mathcal{T}_{2,0}$ and

$\mathcal{T}_{2,\frac{\pi}{2}}$. We further observe that *the distance between any realization of \mathcal{T}_1 and any realization \mathcal{T}_2 is an order of magnitude higher than the distance between two realizations of either \mathcal{T}_1 or \mathcal{T}_2 , or their rotated versions.* Thus, we see that the distance is able to discriminate textures up to rotations.

The results in Table 5.2 are obtained by resampling the auto covariance on the grid $\frac{\mathbb{Z}^3}{4}$ while the results in Table 5.3 are obtained using the auto covariance resampled on $\frac{\mathbb{Z}^3}{2}$. The finer grid does not give any significant improvement. Hence, in this case, resampling on $\frac{\mathbb{Z}^3}{2}$ is enough. Table 5.4 shows the results obtained with the autocovariance defined on the original grid \mathbb{Z}^3 . Here $\mathcal{T}_{1,0}$ and $\mathcal{T}_{1,\frac{\pi}{2}}$ are at a much larger distance from each other than two realizations of $\mathcal{T}_{1,0}$ or $\mathcal{T}_{1,\frac{\pi}{2}}$. Same is true for $\mathcal{T}_{2,0}$ and $\mathcal{T}_{2,\frac{\pi}{2}}$ as well. Since we have not resampled the autocovariance function on a finer grid in this case, we end up rotating by a simple linear interpolation. Hence, we conclude that rotation by simple linear interpolation is not enough. The data must be resampled on a grid that is fine enough to keep the error due to linear interpolation under control.

Finally, observe that the Euler angles corresponding to the minimizer for each case are listed below each distance. They have been normalized by π to make it easier to read. Hence, in each case we list the angles $(\alpha^*/\pi, \beta^*/\pi, \gamma^*/\pi)$, where $(\alpha^*, \beta^*, \gamma^*)$ is the minimizer for the optimization problem required to calculate the distance. This minimizer corresponds to the rotation that must be applied on one texture to get the other in case one is a rotated version of the other. As we can observe in Tables 5.2 and 5.3, all these minimizers are close to the expected values modulo the symmetries assumed, i.e. each can be off by $\pm\pi$.

	$\mathcal{T}_{1,0}$	$\mathcal{T}_{1,\frac{\pi}{2}}$	$\mathcal{T}_{2,0}$	$\mathcal{T}_{2,\frac{\pi}{2}}$
$\mathcal{T}_{1,0}$	0.0007 (0.5871,0,0.3333)	0.0005 (0.4925,0.4515,0.5274)	0.0072 (0.1592,0.0348,0)	0.0137 (0.0199,0.4913)
$\mathcal{T}_{1,\frac{\pi}{2}}$	0.0010 (0.6070,0.4913,0.5274)	0.0007 (0,0,0)	0.0101 (0.9103,0.4714,0.5274)	0.0182 (0.5025,0,0)
$\mathcal{T}_{2,0}$	0.0123 (0.7512,0.0050,0)	0.0128 (0.4925,0.4814,0.9947)	0.0006 (0.0050,0.0298,0)	0.0004 (0.9900,0.4963,0)
$\mathcal{T}_{2,\frac{\pi}{2}}$	0.0093 (0.7263,0.4913,0.0398)	0.0101 (0,0.0039,0.5025)	0.0012 (0.0099,0.4963,0)	0.0009 (0.0050,0,0)

Table 5.2: Distances between two rotations of two distinct textures using the rotationally invariant distance defined in Equation (5.23) and autocovariance resampled on $\frac{\mathbb{Z}^3}{4}$. Below each distance we list the angles $(\alpha^*/\pi, \beta^*/\pi, \gamma^*/\pi)$, where $(\alpha^*, \beta^*, \gamma^*)$ is the minimizer.

	$\mathcal{T}_{1,0}$	$\mathcal{T}_{1,\frac{\pi}{2}}$	$\mathcal{T}_{2,0}$	$\mathcal{T}_{2,\frac{\pi}{2}}$
$\mathcal{T}_{1,0}$	0.0006 (0.6716,0,0.3333)	0.0006 (0.4974,0.4814,0.5075)	0.0073 (0.6319,0,0.3333)	0.0136 (0,0.4913,0)
$\mathcal{T}_{1,\frac{\pi}{2}}$	0.0013 (0.4825,0.4913,0.0050)	0.0007 (0,0.0050,0)	0.0100 (0.4975,0.4814,0.0050)	0.0164 (0.8507,0,0.6667)
$\mathcal{T}_{2,0}$	0.0125 (0.8208,0,0.6667)	0.0203 (0.0099,0,0)	0.0010 (0,0,0)	0.0004 (0.0050,0.4963,0)
$\mathcal{T}_{2,\frac{\pi}{2}}$	0.0119 (0,0.4863,0.0249)	0.0082 (0.5024,0,0)	0.0007 (0,0.4814,0.0050)	0.0008 (0,0.0050,0)

Table 5.3: Distances between two rotations of two distinct textures using the rotationally invariant distance defined in Equation (5.23) and autocovariance resampled on $\frac{\mathbb{Z}^3}{2}$. Below each distance we list the angles $(\alpha^*/\pi, \beta^*/\pi, \gamma^*/\pi)$, where $(\alpha^*, \beta^*, \gamma^*)$ is the minimizer.

	$\mathcal{T}_{1,0}$	$\mathcal{T}_{1,\frac{\pi}{2}}$	$\mathcal{T}_{2,0}$	$\mathcal{T}_{2,\frac{\pi}{2}}$
$\mathcal{T}_{1,0}$	0.0026 (0,0,0)	0.0812 (0.0050,0.0050,0)	0.0330 (0.0099,0,0)	0.1750 (0.0050,0,0)
$\mathcal{T}_{1,\frac{\pi}{2}}$	0.1118 (0,0,0)	0.0010 (0,0,0)	0.0852 (0.0099,0,0)	0.0562 (0,0,0)
$\mathcal{T}_{2,0}$	0.0454 (0,0.0050,0)	0.0694 (0.0050,0.0050,0)	0.0016 (0,0,0)	0.0108 (0,0.4963,0)
$\mathcal{T}_{2,\frac{\pi}{2}}$	0.0607 (0,0.4963,0)	0.0473 (0,0,0)	0.0246 (0,0.4963,0)	0.0018 (0,0,0)

Table 5.4: Distances between two rotations of two distinct textures using the rotationally invariant distance defined in Equation (5.23) and autocovariance sampled on the original grid \mathbb{Z}^3 . Below each distance we list the angles $(\alpha^*/\pi, \beta^*/\pi, \gamma^*/\pi)$, where $(\alpha^*, \beta^*, \gamma^*)$ is the minimizer.

5.4. EXPERIMENTAL RESULTS

For the experiments described above we only took two distinct textures to test the rotational invariance of the our distance function. Next, we study five distinct textures, two of which are the ones presented above (\mathcal{T}_1 and \mathcal{T}_2) while the other three, denoted by $\mathcal{T}_3, \mathcal{T}_4$ and \mathcal{T}_5 , are produced using GMRF models with higher order neighborhoods. Now, since we still use order one neighborhood to get the texture signatures, the estimate for σ^2 may not be the same as, or even close to, the σ^2 used to produce these textures. In fact, for the examples we use here, even though we used the same σ^2 (but different θ s) to produce $\mathcal{T}_3, \mathcal{T}_4$ and \mathcal{T}_5 , the value of σ^2 estimated for a order one GMRF fitted to each of these three textures is different. Thus, in this case, the estimate of σ^2 might be enough to discriminate textures. It is interesting to note that this difference in the value of σ^2 is not an impediment for our distance function. This is evident from the results tabulated in Table 5.5. For each of the five textures, we see that the distance between two of its

	\mathcal{T}_1	\mathcal{T}_2	\mathcal{T}_3	\mathcal{T}_4	\mathcal{T}_5
\mathcal{T}_1	0.0006	0.0073	0.4232	2.3180	1.7724
\mathcal{T}_2	0.0125	0.0010	0.4894	2.5227	1.8381
\mathcal{T}_3	0.4466	0.5134	0.0004	0.5208	0.4563
\mathcal{T}_4	2.4314	2.6315	0.5605	0.0021	0.3533
\mathcal{T}_5	1.8200	1.9227	0.4318	0.2540	0.0043

Table 5.5: Distances between five distinct textures using the rotationally invariant distance defined in Equation (5.23) and autocovariance resampled on the grid $\frac{\mathbb{Z}^3}{2}$.

realizations is still relatively much smaller than its distance from other textures. Thus, we see that we can even discriminate textures arising from higher order GMRFs using

our scheme. This shows that this classification scheme is not limited to synthetic textures produced using GMRFs with order one neighborhoods, and may also be applied to a larger class of textures.

5.5 Conclusion and Future Work

In this chapter we have presented a novel approach to rotationally invariant 3-*D* texture classification. We define a rotationally invariant distance on GMRF-based texture signatures. Rotation of a texture is achieved via rotation of the autocovariance function corresponding to the texture. The practical implementation of the rotationally invariant distance is shown to work well on experimental data. Moving forward, we want to test if these GMRF-based texture signatures, along with the rotationally invariant distance, can be used to separate natural 3-*D* textures arising, for example, in medical imaging. We have used a 2-*D* version of this scheme to separate natural textures (taken from the Brodatz library for instance) that are not generated using a GMRF. The positive results in 2-*D* together with the fact that we could discriminate textures obtained from higher order GMRFs in 3-*D*, makes our scheme a promising candidate for rotationally invariant classification of natural textures in 3-*D*.

Bibliography

- [1] E.H. Adelson, E. Simoncelli, and R. Hingoranp. Orthogonal pyramid transforms for image coding. In *Visual Communications and Image Processing II*, volume 845 of *Proceedings SPIE*, pages 50–58, 1987.
- [2] A. Aldroubi, C. Cabrelli, and U. Molter. Wavelets on irregular grids with arbitrary dilation matrices and frame atoms on $L^2(\mathbb{R}^d)$. *Appl. Comput. Harmon. Anal.*, 17(2):119–140, 2004. Special issue: Frames in Harmonic Analysis, Part II.
- [3] M. Antonini, M. Barlaud, and P. Mathieu. Image coding using lattice vector quantization of wavelet coefficients. In *IEEE Internat. Conf. Acoust. Signal Speech Process.*, pages 2273–2276, 1991.
- [4] A. Ayache. Construction de bases d’ondelettes orthonormées de $L^2(\mathbb{R}^2)$ non séparables, à support compact et de régularité arbitrairement grande. *Comptes Rendus Académie des Sciences de Paris*, 325:17–20, 1997.
- [5] A. Ayache. Construction of non separable dyadic compactly supported wavelet bases for $L^2(\mathbb{R}^2)$ of arbitrarily high regularity. *Revista Matemática Iberoamericana* 15, 15(1):37–58, 1999.
- [6] A. Ayache. Some methods for constructing non separable, orthonormal, compactly supported wavelet bases. *Appl. Comput. Harmon. Anal.*, 10:99–111, 2001.
- [7] R. Azencott and D. Dacunha-Castelle. *Series of Irregular Observations*. Springer-Verlag, 1986.
- [8] R. Azencott, J.P. Wang, and L. Younes. Texture classification using Gabor filters. *IEEE Trans. Pattern Anal. Machine Intell.*, 19(2):148–152, 1997.
- [9] L.W. Baggett, P.E.T. Jorgensen, K.D. Merrill, and J.A. Packer. Construction of Parseval wavelets from redundant filter systems. *J. Math. Phys.*, 46:083502–1 to 083502–28, 2005.

- [10] E. Belogay and Y. Wang. Arbitrarily smooth orthogonal nonseparable wavelets in R^2 . *SIAM Journal of Mathematical Analysis*, 30:678–697, 1999.
- [11] J. J. Benedetto and J. R. Romero. The construction of d - dimensional multiresolution analysis frames. *J. Appl. Func. Anal.*, 2(4):403–426, 2007.
- [12] J.J. Benedetto and S. Li. The theory of multiresolution analysis frames and applications to filter banks. *Appl. Comput. Harmon. Anal.*, 5:389–427, 1998.
- [13] J.J. Benedetto and O.M. Treiber. Wavelet frames: Multiresolution analysis and the unitary extension principle. In L. Debnath, editor, *Wavelet Transforms and Time-Frequency Signal Analysis*, pages 3–36. Birkhauser, Boston MA, 2001.
- [14] B.G. Bodmann and M. Papadakis et. al. Frame isotropic multiresolution analysis for micro CT scans of coronary arteries. In M. Papadakis, A. Laine, and M. Unser, editors, *Wavelets XI*, volume 5914, pages 59141O/1–12. SPIE, 2005.
- [15] C. De Boor, R. A. DeVore, and A. Ron. Approximation from shift-invariant subspaces of $L_2(\mathbb{R}^d)$. *Trans. Amer. Math. Soc.*, 341(2):787–806, 1994.
- [16] M. Bownik. The structure of shift invariant subspaces of $L^2(\mathbb{R}^n)$. *J. Funct. Anal.*, 177:282–309, 2000.
- [17] Marcin Bownik. A characterization of affine dual frames in $L^2(\mathbb{R}^n)$. *App. and Comp. Harm. Anal.*, 8:203–221, 2000.
- [18] P.J. Burt and E.H. Adelson. The Laplacian pyramid as a compact image code. *Proc. IEEE Int. Conf. Commun.*, 31(4):532–540, 1983.
- [19] C. Cabrelli, C. Heil, and U. Molter. *Self-Similarity and Multiwavelets in Higher Dimensions*, volume 170 of *Memoirs, Amer. Math. Soc.* AMS, 2004.
- [20] E. J. Candes and L. Demanet. The curvelet representation of wave propagators is optimally sparse. *Comm. Pure and Appl. Math.*, 58(11):1472–1528, 2005.
- [21] E.J. Candes and D.L. Donoho. Ridgelets: a key to higher dimensional intermittency? *Phil. Trans. R. Soc. London*, A:2495–2509, 1999.
- [22] E.J. Candes and D.L. Donoho. New tight frames of curvelets and optimal representations of objects with piecewise c^2 singularities. *Communications on pure and applied mathematics*, 57(2):219–266, 2004.
- [23] J. Canny. A computational approach to edge detection. *IEEE Trans. Pattern Anal. Machine Intell.*, 8(6):679–698, November 1986.
- [24] T. Chang and C. Kuo. Texture analysis and classification with tree-structured wavelet transform. *IEEE Transaction on Image Processing*, 2(4):429–441, 1995.

- [25] R. Chellappa. Two-dimensional discrete Gaussian Markov random field models for image processing. *Progress in Pattern Recognition 2*, pages 79–112, 1985.
- [26] R. Chin and C. Harlow. Automated visual inspection: A survey. *IEEE Trans. Pattern Anal. Machine Intell.*, PAMI-4(6):557–573, 1982.
- [27] G.S. Chirikjian and A. B. Kyatkin. *Engineering Applications of Noncommutative Harmonic Analysis: With Emphasis on Rotation and Motion Groups*. CRC Press, 2000. electronic resource.
- [28] O. Christensen. *An Introduction to Frames and Riesz Bases*. Birkhauser, 2002.
- [29] O. Christensen. *Frames and Riesz Bases*. Birkhäuser, 2005.
- [30] C. K. Chui, W. He, and J. Stockler. Compactly supported tight and sibling frames with maximum vanishing moments. *Appl. Comput. Harmon. Anal.*, 13:224–262, 2002.
- [31] Claerbout. *Imaging the Earth’s Interior*. <http://sep.stanford.edu/oldreports/sep40/>.
- [32] J.M. Coggins and A.K. Jain. A spatial filtering approach to texture analysis. *Pattern Recognition Letters*, 3(3):195–203, 1985.
- [33] A. Cohen and I. Daubechies. Nonseparable bidimensional wavelet bases. *Revista Matematica Iberoamericana*, 9:51–137, 1993.
- [34] A. Cohen, I. Daubechies, and J.-C. Feauveau. Biorthogonal bases of compactly supported wavelets. *Commun. Pure Appl. Math.*, 45:485–560, 1992.
- [35] F.S. Cohen, Z. Fan, and M.A. Patel. Classification of rotated and scaled textured images using Gaussian Markov Random Field models. *IEEE Transactions on Pattern Analysis and Machine Intelligence*, 13(2):192–202, 1991.
- [36] L. Condat, B. Forster-Heinlein, and D. Van Der Ville. A new family of rotation-covariant wavelets on the hexagonal lattice. In D. Van Der Ville, V. Goyal, and M. Papadakis, editors, *Wavelets XII*, volume 6701, pages 67010B–1 to 67010B–9. SPIE, 2007.
- [37] J.B. Conway. *A Course in Operator Theory*, volume 21 of *Graduate Studies in Mathematics*. American Mathematical Society, Providence, RI, 2000.
- [38] I. Daubechies, B. Han, A. Ron, and Z. Shen. Framelets: MRA-based constructions of wavelet frames. *Appl. Comput Harmon. Anal.*, 14(1):1–46, 2003.
- [39] J. Derado. Nonseparable, compactly supported interpolating refinable functions with arbitrary smoothness. *Appl. Comput. Harmon. Anal.*, 10(2):113–138, 2001.
- [40] D.L. Donoho and Xiaoming Huo. Beamlets and multiscale image analysis. In T.J. Barth, T. Chan, and R. Haimes, editors, *Springer Lecture Notes in Computational Science and Engineering*, volume 20, pages 149–196, 2002.

- [41] G. Easley, D. Labate, and W. Lim. Sparse directional image representations using the Discrete Shearlet Transform. *Appl. Comput. Harmon. Anal.*, 25(1):25–46, 2008.
- [42] J. Epperson and M. Frazier. An almost orthogonal radial wavelet expansion for radial distributions. *J. Fourier Anal. Applic.*, 1(3):311–353, 1995.
- [43] J. Epperson and M. Frazier. Polar wavelets and associated Littlewood-Paley theory. *Dissertationes Mathematicae*, 348:1–51, 1996.
- [44] G. Blacquiere et. al. 3D table-driven migration. *Geophys. Prosp.*, 37:925–958, 1989.
- [45] K. Etemad and R. Chellappa. Separability based tree-structured local basis selection for texture classification. In *ICIP 1994*, volume 3, Austin, TX, 1994.
- [46] J. Fehr and H. Burkhardt. 3d rotation invariant local binary patterns. In *ICPR 2008*, Tampa, FL, 2008.
- [47] M. Fickus and D.G. Mixon. Isotropic moments over integer lattices. *Appl. Comp. Harmon. Anal.*, 26(1):77–96, January 2009.
- [48] M. Fickus, G.S. Seetharaman, and M.E. Oxley. Multiscale moment transforms over the integer lattice. In D. Van Der Ville, V. Goyal, and M. Papadakis, editors, *Wavelets XII*, volume 6701, pages 67011N–1 to 67011N–8. SPIE, 2007.
- [49] B. Forster, T. Blu, , D. Van De Ville, and M. Unser. Shift-invariant spaces from rotation-covariant functions. *Applied Comp. Harmon. Anal.*, 25(2):240–265, 2008.
- [50] W.T. Freeman and E.H. Adelson. The design and use of steerable filters. *IEEE Trans. Pattern Anal. Machine Intell.*, 13(9):891–906, 1991.
- [51] S. Geman and D. Geman. Stochastic relaxation, Gibbs distributions, and the bayesian restoration of images. *IEEE Trans. Pattern Anal. Machine Intell.*, 6:721–741, 1984.
- [52] K. Grochenig and W. Madych. Multiresolution analysis, Haar bases and self-similar tilings. *IEEE Trans. Inform. Theory*, 38:556–568, 1992.
- [53] A. Grossman and J. Morlet. Decomposition of Hardy functions into square integrable wavelets of constant shape. *SIAM J. Math. Anal.*, 15(4):723–736, 1984.
- [54] K. Guo, D. Labate, W. Lim, G. Weiss, and E. Wilson. Wavelets with composite dilations and their MRA properties. *Appl. Comput. Harmon. Anal.*, 20(2):202–236, 2006.
- [55] X. Guyon. *Random Fields on a Network*. Probability and its Applications. Springer Verlag, 1995.
- [56] D. Hale. 3-D migration via McClellan transformations. *Geophysics*, 56(11):1778–1785, 1991.

- [57] Bin Han. On dual tight wavelet frames. *Appl. Comput. Harmon. Anal.*, 4(4):380–413, 1997.
- [58] R. Haralick. Statistical and structural approaches to texture. *Proceedings of IEEE*, 67(5):610–621, 1979.
- [59] W. He and M. J. Lai. Examples of bivariate nonseparable compactly supported orthonormal continuous wavelets. In M. Unser A. Aldroubi, A. Laine, editor, *Wavelet Applications in Signal and Image Processing IV*, volume 3169 of *Proceedings SPIE*, pages 303–314, 1997.
- [60] E. Hernández and G. Weiss. *A First Course on Wavelets*. CRC Press, Boca Raton, FL, 1996.
- [61] A.K. Jain and F. Farrokhnia. Unsupervised texture segmentation using Gabor filters. *IEEE Trans. Pattern Anal. Machine Intell.*, 18(2):1167–1186, 1991.
- [62] S. Jain, M. Papadakis, and E. Dussaud. Explicit schemes in seismic migration and isotropic multiscale representations. In E. Grinberg, D.R. Larson, P.E.T. Jorgensen, P. Massopust, G. Olafsson, E.T. Quinto, and B. Rubin, editors, *Radon Transforms, Geometry, and Wavelets*, volume 464 of *Contemp. Mathem.*, pages 177–200. Amer. Math. Soc., 2008.
- [63] A. Karasaridis and E. Simoncelli. A filter design technique for steerable pyramid image transforms. In *Acoustics Speech and Signal Processing*. ICASP, May 7-10 1996. Atlanta, GA.
- [64] R.L. Kashyap. Analysis and synthesis of image patterns by spatial interaction models. *Progress in Pattern Recognition*, pages 149–186, 1981.
- [65] R.L. Kashyap and R. Chellappa. Estimation and choice of neighbors in spatial-interaction models of images. *IEEE Transactions on Information Theory*, 1:60–72, 1983.
- [66] R.L. Kashyap and A. Khotanazad. A model-based method for rotation invariant texture classification. *IEEE Transactions on Pattern Analysis and Machine Intelligence*, 8(4):472–481, 1986.
- [67] N. Kingsbury. Image processing with complex wavelets. *Phil. Trans. R. Soc. London A*, 357:2543–2560, 1999.
- [68] J. Kovačević and M. Vetterli. Nonseparable multidimensional perfect reconstruction filter-banks and wavelet bases in \mathbb{R}^n . *IEEE Trans. Inform. Theory*, 38:533–555, 1992.
- [69] V.A. Kovalev, F. Kruggel, H.J. Gertz, and D.Y. von Cramon. Three-dimensional texture analysis of MRI brain datasets. *IEEE Trans.on Medical Imaging*, 20(5):424–433, 2001.

- [70] A.S. Kurani, D.H. Xu, J.D. Furst, and D.S. Raicu. Co-occurrence matrices for volumetric data. In *7th IASTED International Conference on Computer Graphics and Imaging*, 2004.
- [71] D. Labate, W. Lim, G. Kutyniok, and G. Weiss. Sparse multidimensional representation using shearlets. In M. Papadakis, A. Laine, and M. Unser, editors, *Wavelets XI*, volume 5914 of *SPIE Proceedings*, pages 247–255, jan 2005.
- [72] S. Lakshmanan and H. Derin. Valid parameter space for 2-D Gaussian Markov Random Fields. *IEEE Transactions on Information Theory*, 39(2):703–709, 1993.
- [73] W. Lawton and H.L. Resnikoff. Multidimensional wavelet bases. Technical report, Aware, Inc., Bedford, MA, February 1991.
- [74] P. D. Lax. Translation invariant spaces. *Acta Math.*, 101:163–178, 1959.
- [75] M. Lindemann. *Approximation Properties of Non-Separable Wavelet Bases With Isotropic Scaling Matrices And Their Relation to Besov Spaces*. PhD thesis, Universitaet Bremen, 2005.
- [76] S.Y. Lu and K.S. Fu. A syntactic approach to texture analysis. *Computer Graphics and Image Processing*, 7:303–330, 1978.
- [77] A. Madabhushi, M. Feldman, D. Metaxas, D. Chute, and J. Tomaszewski. A novel stochastic combination of 3d texture features for automated segmentation of prostatic adenocarcinoma from high resolution MRI. *Medical Image Computing and Computer-Assisted Intervention*, 2878:581–591, 2003.
- [78] S. Mallat. Multiresolution approximation and wavelet orthonormal bases of L^2 . *Trans. Amer. Math. Soc.*, 315:69–87, 1989.
- [79] S. Mallat. *A Wavelet Tour of Signal Processing: The Sparse Way*. Academic Press, third edition, 2008.
- [80] J. Mao and A.K. Jain. Texture classification and segmentation using multiresolution simultaneous autoregressive models. *Pattern Recognition*, 25(2):173–188, 1992.
- [81] G.F. Margrave and et al. Improving explicit seismic depth migration with a stabilizing Wiener filter and spatial resampling. *Geophysics*, 71(3):S111–S120, 2006.
- [82] D. Marr and E. Hildreth. The theory of edge detection. *Proc. R. Soc. London B*, 207:187–217, 1980.
- [83] J.H. McClellan. On the design of one-dimensional and two-dimensional FIR digital filters. *PhD Thesis, Rice University*, 1973.
- [84] J.H. McClellan and D.S.K. Chan. A 2-D FIR filter structure derived from the Chebyshev recursion. *IEEE transaction on circuits and systems*, CAS-24(7):372–378, 1977.

- [85] Y. Meyer. *Wavelets and Operators: Advanced Mathematics*. Cambridge University Press, 1992.
- [86] G. Olafsson and D. Speegle. Wavelets, wavelet sets and linear actions on \mathbb{R}^n . In C. Heil, P. Jorgensen, and D. Larson, editors, *Wavelets, Frames and Operator Theory*, volume 345 of *Contemporary Mathematics*, pages 253–281, 2004.
- [87] M. Papadakis. Frames of translates and the generalized frame multiresolution analysis. In K. Kopotun, T. Lyche, and M. Neamtu, editors, *Trends in Approximation Theory*, Innovations in Applied Mathematics, pages 353–362. Vanderbilt University Press, Nashville, TN, 2001.
- [88] M. Papadakis, B.G. Bodmann, S.K. Alexander, D. Vela MD, S. Baid, A.A. Gittens, D.J. Kouri, S.D. Gertz MD, S. Jain, J.R. Romero, X. Li, P. Cherukuri, D.D. Cody, G. W. Gladish MD, I. Aboshady MD, J.L. Conyers, and S.W. Casscells. Texture-based tissue characterization for high-resolution CT-scans of coronary arteries. *Comm. in Numer. Methods in Engineering*, 25:597–613, 2009.
- [89] M. Papadakis, G. Gogoshin, I.A. Kakadiaris, D.J. Kouri, and D.K. Hoffman. Non-separable radial frame multiresolution analysis in multidimensions. *Numer. Function. Anal. Optimization*, 24:907–928, 2003.
- [90] K. R. Parthasarathy. *Probability Measures on Metric Spaces*. Probability and Mathematical Statistics. Academic Press, 1967.
- [91] R. Porter and N. Canagarajah. Robust rotation-invariant texture classification: wavelet, Gabor filter and GMRF based schemes. *IEE Proc.- Vis. Image Signal Process.*, 144(3):180–188, 1997.
- [92] J. Portilla, V. Strela, M.J. Wainwright, and E.P. Simoncelli. Image denoising using Gaussian scale mixtures in the wavelet domain. *IEEE Trans. Image Processing*, 12(11):1338–1351, 2003. Computer Science techn. rep. nr. TR2002-831, Courant Institute of Mathematical Sciences.
- [93] Elena Boykova Rangelova. Segmentation of textured images on three-dimensional lattices. *PhD Thesis, University of Dublin, Trinity College*, 2002.
- [94] C.C. Reyes-Aldasoro and A. Bhalerao. Volumetric feature selection for MRI. *Information Processing in Medical Imaging*, 2732:282–293, 2003.
- [95] Ristow and Ruhl. Fourier finite-difference migration. *Geophysics*, 59(12):1882–1893, 1994.
- [96] J.R. Romero, S. Alexander, S. Baid, S. Jain, and M. Papadakis. The geometry and the analytic properties of Isotropic Multiresolution Analysis. *Advances in Comp. Math.*, 31:283–328, 2009.

- [97] A. Ron and Z. Shen. Affine system in $L_2(\mathbb{R}^d)$: The analysis of the Analysis operator. *Journal Func. Anal.*, pages 408–447, 1997.
- [98] I.W. Selesnick. Smooth wavelet tight frames with zero moments. *Appl. Comput. Harmon. Anal.*, 10(2):163–181, 2001.
- [99] I.W. Selesnick and L. Sendur. Iterated oversampled filter banks and wavelet frames. In M. Unser A. Aldroubi, A. Laine, editor, *Wavelet Applications in Signal and Image Processing VIII*, volume 4119 of *Proceedings of SPIE*, 2000.
- [100] E.P. Simoncelli, W.T. Freeman, E.H. Adelson, and D.J. Heeger. Shiftable multi-scale transforms. *IEEE Trans. Inform. Theory*, 38(2):587–607, 1992.
- [101] R. Soubaras. Explicit 3-D migration using equiripple polynomial expansion and Laplacian synthesis. *Geophysics*, 61(5):1386–1393, 1996.
- [102] A. Teuner, O. Pichler, and B.J. Hosticka. Unsupervised texture segmentation of images using tuned Gabor filters. *IEEE Transaction on Image Processing*, 4(6):863–870, 1995.
- [103] J.W. Thorbecke. Common focus point technology. *PhD Thesis, Delft University of Technology*, page A.2.5, 1997.
- [104] J.W. Thorbecke, K. Wapenaar, and G. Swinnen. Design of one-way wavefield extrapolation operators, using smooth functions in WLSQ optimization. *Geophysics*, 69(4):1037–1045, 2006.
- [105] F. Tomita and S. Tsuji. *Computer Analysis of Visual Textures*. Kluwer Academic Publishers, 1990.
- [106] M. Unser. Texture classification and segmentation using wavelet frames. *IEEE Transaction on Image Processing*, 2(4):429–441, 1995.
- [107] R.L. Wheeden and A. Zygmund. *Measure and Integral. An Introduction to Real Analysis*. Pure and Applied Mathematics. Marcel-Dekker Inc., 1977.
- [108] D.H. Xu, A.S. Kurani, J.D. Furst, and D.S. Raicu. Run-length encoding for volumetric texture. In *4th IASTED International Conference on Visualization, Imaging and Image Processing*, 2004.
- [109] L. Ying, L. Demanet, and E. Candes. 3-D discrete curvelet transform. In M. Papadakis, A. Laine, and M. Unser, editors, *Wavelets XI*, volume 5914 of *SPIE Proceedings*, pages 591413–1 to 591413–11, 2005.

Index

- D_A , 10
- PW_Ω , 9
- PW_r , 9
- $T_{\mathbf{y}}$, 9
- $X_{\phi\psi}$, 36
- $\Psi^{a(s)}$, 39
- \mathbb{S}^{d-1} , 9
- $e_{\mathbf{k}}$, 9

- $\langle \phi \rangle$, 9

- Analysis operator, 23

- Bessel
 - bounds, 22
 - family, 22

- Density point, 12
- Dilation operator, 10
- Downsampling operator, 69

- Euler angles, 128

- gimbal lock, 129
- ZYZ-convention, 128

- Exact reconstruction formula, 21, 70

- Explicit schemes, 75

- Extension Principles, 35
 - Mixed, 39
 - Oblique, 38
 - Unitary, 35, 37

- Fast Wavelet Algorithm, 15
 - Decomposition, 17, 21, 69
 - Reconstruction, 18, 22, 69
 - Isotropic, 68

- Filter
 - High Pass, 15
 - Low Pass, 14, 31

- FIWT, 68

- Fourier Transform, 8

- Frames, 22

- frame operator, 23
- dual, 23
- frame bounds, 22
- Parseval, 22
- Function
 - isotropic, 12
 - radial, 11
- Gaussian Markov Random Field, 118
 - KL-Distance, 125
 - Parameter estimation, 120
 - Synthesis of, 123
- Gibbs Random Field (GRF), 117
- GMRF, *see* Gaussian Markov Random Field
- Hammersley-Clifford theorem, 117
- IMRA, 24
- KL-Distance, 125
- Kullback Leibler Distance, 125
- Local specification, 117
- Markov Random Field (MRF), 117
- Matrix
 - Quincunx, 91
 - Expansive, 10
 - Radially Expansive, 10
- McClellan transform, 93
- MEP, *see* Extension Principles
- Modulation matrix, 37
- MRA, 13
- Multiresolution Analysis
 - Isotropic, 24
 - Classical, 13
- Phase-shift propagator operator, 77
- Propagator
 - filter, 81
 - operator, 77
- Pyramid Algorithm, *see* Fast Wavelet Algorithm
- Radial
 - function, 11
 - set, 10, 11
- Refinable function, 31
- Scaling function, 13
- Shift operator, 9
- Soubaras' Laplacian synthesis, 94
- Synthesis operator, 23
- Texture, 111
 - Rotation of a, 126
 - signature, 112

Two-scale relation, 14

UEP, *see* Extension Principles

Upsampling operator, 70

Wave equation migration, 75

Wavelets

 Isotropic, 58

 Orthonormal, 13